I. Regular and chaotic motions in a wave tank

II. Interactions between a free surface and a shed vortex sheet

by

Wu-ting Tsai

B.S., National Taiwan University (1981)

M.S., National Taiwan University (1983)

SUBMITTED TO THE DEPARTMENT OF OCEAN ENGINEERING
IN PARTIAL FULFILLMENT OF THE REQUIREMENTS
FOR THE DEGREE OF

DOCTOR OF PHILOSOPHY

at the

MASSACHUSETTS INSTITUTE OF TECHNOLOGY

September 1991

Signature of Author _____
Department of Ocean Engineering
September 1991

Certified by _____
Dick K.P. Yue
Associate Professor, Ocean Engineering
Thesis Supervisor

Accepted by _____
A. Douglas Carmichael
Professor, Ocean Engineering
Chairman, Department Committee on Graduate Students

I. Regular and chaotic motions in a wave tank

II. Interactions between a free surface and a shed vortex sheet

by

Wu-ting Tsai

Submitted to the Department of Ocean Engineering
in partial fulfillment of the requirements for
the degree of Doctor of Philosophy

Abstract

Wave and vortex motions generated simultaneously by different excitation mechanisms interact with each other resulting in distinct and intricate features of nonlinear dynamics. In this thesis, we examine two important examples of these interactions: an asymptotic study of resonant interactions between directly and parametrically forced waves thus expounding a route to deterministic chaos; and a numerical study of the interactions between a free surface and a vortex sheet shed in the wake of a body thus quantifying the critical role of the Froude number.

I. Regular and chaotic motions in a wave tank

We consider the resonant excitation of surface waves inside a rectangular wave tank of arbitrary water depth with a flap-type wavemaker on one side. Depending on the length and width of the tank relative to the sinusoidal forcing frequency of the wave paddle, three classes of resonant mechanisms can be identified. The first two are the well-known synchronous, resonantly forced longitudinal standing waves, and the subharmonic, parametrically excited transverse (cross) waves. The third class is new and involves the simultaneous resonance of the longitudinal and cross waves and their internal interactions. In this case, temporal chaotic motions are found for

a broad range of parameter values and initial conditions. These are studied by local bifurcation and stability analyses, direct numerical simulations, estimations of the Lyapunov exponents and power spectra, and examination of Poincaré surfaces. To obtain a *global* criterion for widespread chaos, the method of resonance overlap is adopted and found to be remarkably effective.

II. Interactions between a free surface and a shed vortex sheet

The nonlinear interactions between a free surface and a shed vortex shear layer in the inviscid wake of a surface-piercing plate is studied numerically using a mixed-Eulerian-Lagrangian method. For a plate with submergence d at rest abruptly attaining a constant horizontal velocity U, the problem is governed by a single parameter, the Froude number $F_n = U/\sqrt{gd}$. Depending on F_n, three classes of interaction dynamics (subcritical, transcritical and supercritical) are identified. For subcritical F_n ($<\sim 0.7$), the free surfaces plunge on both forward and lee sides of the plate before significant interactions with the vortex sheet occur. For transcritical and supercritical F_n, interactions between the free surface and the starting vortex result in a stretching of the vortex sheet which eventually rolls up into double-branched spirals as a result of Kelvin-Helmholtz instabilities. In the transcritical range ($F_n \sim 0.7 - 1.0$), the effect of the free surface on the double-branched spirals remains weak, while for supercritical F_n ($>\sim 1.0$), strong interactions lead to entrainment of the double-branched spiral into the free surface resulting in large surface features.

Thesis Supervisor: Dick K.P. Yue

Title: Associate Professor of Ocean Engineering

Acknowledgments

I would like to express my deepest appreciation to Professor Dick K.P. Yue. He has, for the past six years, taught me and influenced my approach to the study of fluid mechanics. The present work could never have been carried to its completion without his tireless support and encouragement.

I thank Professors C.C. Mei, G.S. Triantafyllou of Levich Institute and M.S. Triantafyllou, who served on my thesis committee, for their knowledgeable suggestions and questions. The study in Part I of the thesis was inspired by the excellent courses in wave hydrodynamics offered by Professor C.C. Mei.

Many people have contributed to the progress of this work at various stages. Dr. D.P. Keenan always patiently listened to me present much of the material in this thesis, and also provided me with enthusiastic support and advice when things got tough. He, Mr. J.-M. Clarisse and I started a small study group when the only way to learn chaotic dynamics at MIT was to learn by yourself. Professors J. Wisdom of Department of Earth, Atmospheric and Planetary Sciences at MIT and K.M.K. Yip of Yale University introduced me the method of resonance overlap, and provided invaluable information on the subject of chaotic dynamics. The features of vortex sheet evolution could never have been captured without the help of Mr. K. Tanizawa of Japan Ship Research Institute in developing the rediscretization algorithm. To these people I express my gratitude.

Most of all, I thank my parents for their love, patience and understanding during these many years, and my wife Tenyi for the calm and brightness she has brought to my life. This thesis is dedicated, with love, to my late grandmother.

Financial support for this research was provided by the National Science Foundation and the Office of Naval Research. Some of the computations were performed on the Cray Y/MP at NSF sponsored Pittsburg Supercomputer Center and on the Cray-2S at Cray Research, Inc.

Contents

I. Regular and chaotic motions in a wave tank 7

1. Introduction 8

2. Formulation of the problem 12

3. Synchronous resonantly forced longitudinal standing waves 15

4. Subharmonic parametrically resonant transverse standing waves . 20

5. Interaction between resonant longitudinal and transverse standing waves 25

5.1. Evolution equations 25

5.2. Stationary solutions and bifurcation diagrams 29

5.3. Regular and chaotic behavior 39

6. Resonance overlap criterion for the onset of widespread chaos 50

7. Concluding remarks 59

Appendix A. Treatment of the inhomogeneous wavemaker boundary conditions 61

Appendix B. Faraday problem for stratified two-layer flow 63

Appendix C. Periodic solutions of the evolution equation governing parametric resonance 70

Appendix D. Second-order solutions for the internal interaction system 75

References 77

II. Interactions between a free surface and a shed vortex sheet 80

1. Introduction 81

2. Mathematical formulation 85

2.1. Mixed first- and second-kinds integral equation 85

2.2. Boundary and initial conditions 87

2.3. Unsteady force and energy 88

3. Numerical implementation 89

3.1. Mixed-Eulerian-Lagrangian method 89

3.2. Adaptive Rediscretization algorithm 91

3.3. Amalgamation of single- and double-branched spirals 97

3.4. Accuracy of numerical time integration 100

3.5. Effects of grid spacing on the plate 102

4. Computational results 104

4.1. Critical Froude number for surface/vortex interaction 104

4.1.1. Subcritical Froude number 106

4.1.2. Transcritical Froude number 109

4.1.3. Supercritical Froude number 118

4.2. Time evolution of characteristic properties 123

4.3. Effect of periodic boundaries 129

4.4. Effect of impulsive plate motion 132

5. Conclusion 136

Appendix A. Numerical evaluation of the discretized integral equations 138

Appendix B. Adaptive rediscretization algorithm 140

References 142

I

Regular and chaotic motions in a wave tank

We consider the resonant excitation of surface waves inside a rectangular wave tank of arbitrary water depth with a flap-type wavemaker on one side. Depending on the length and width of the tank relative to the sinusoidal forcing frequency of the wave paddle, three classes of resonant mechanisms can be identified. The first two are the well-known synchronous, resonantly forced longitudinal standing waves, and the subharmonic, parametrically excited transverse (cross) waves. These have been studied by a number of investigators, notably in deep water. We rederive the governing equations and show good comparisons with the experimental data of Lin & Howard (1960). The third class is new and involves the simultaneous resonance of the synchronous longitudinal and subharmonic cross waves and their internal interactions. In this case, temporal chaotic motions are found for a broad range of parameter values and initial conditions. These are studied by local bifurcation and stability analyses, direct numerical simulations, estimations of the Lyapunov exponents and power spectra, and examination of Poincaré surfaces. To obtain a *global* criterion for widespread chaos, the method of resonance overlap (Chirikov 1979) is adopted and found to be remarkably effective.

1. Introduction

Experiments concerning two-dimensional forced-resonant standing waves were first conducted by Taylor (1953) using a pair of flap-type wavemakers operating symmetrically in a short wave tank. These experiments were designed to verify the theoretical prediction of Penny & Price (1952) for two-dimensional free standing waves on deep water, namely that the crest angle of the highest wave is nearly 90°. An unexpected and interesting observation in Taylor's experiments is that lateral instabilities of the free surface which occur in the form of transverse standing waves with crests normal to the wavemaker. Taylor's experiments involved resonantly forced standing waves but were conducted to verify theoretical predictions for free standing waves, so the actual forcing mechanisms were not considered.

Motivated by Taylor's work, the resonantly excited, longitudinal forced waves and transverse cross waves (wave motions respectively perpendicular and parallel to the wavemaker) in a short wave tank with deep water were investigated both analytically and experimentally by Lin & Howard (1960). Using a method similar to Penney & Price (1952), they looked for periodic nonlinear solutions for the resonated longitudinal and transverse standing waves. For the longitudinal forced standing waves, they obtained a relationship for the response amplitude versus excitation frequency up to third order in surface displacement, a result which was largely confirmed by their experimental measurements. For the standing cross waves, however, they were able to carry out the analysis only to second order. The nonlinear dependence of the wave amplitude on frequency did not appear, and they were unable to make quantitative comparisons with the experiments.

Since then, there have been two main studies of standing cross waves in a short wave tank. Garrett (1970) was apparently the first to show that the mechanism for the excitation of transverse cross waves is indeed a parametric resonance. Using an averaging over the longitudinal waves, Garrett obtained a Mathieu equation governing the amplitude of cross waves. This analysis explains the occurrence of

subharmonic resonant cross waves at specific excitation frequencies but cannot predict their amplitudes, since the solution of the Mathieu equation is unbounded in the unstable region. Recently, Miles (1988) used a Lagrangian formulation and obtained a Hamiltonian system governing the slow modulation of the cross wave amplitude. Miles' analysis included the nonlinear interaction between the motions of the wavemaker and the cross wave to second order and the self-interaction of cross waves to third order. The equation is equivalent to that governing the parametrically excited surface waves in a vertically oscillating tank (Miles 1984*a*).

Both Garrett's and Miles' studies are for the case where the longitudinal wave is not resonantly excited by the wavemaker motion. For such a condition, the amplitude of the longitudinal wave is of higher order than that of the resonant cross wave. If the length of the tank is such that the longitudinal waves are also resonated (synchronously), the amplitudes of both the longitudinal and cross waves may be of the same order of magnitude (see, for example, the experimental measurements in figure 7.2 of Lin & Howard 1960). In this case, the internal interactions between the two standing waves also become important, resulting in a complicated and varied dynamical system.

In this work, we re-examine the resonantly excited longitudinal and transverse waves in a three-dimensional rectangular tank with a harmonically driven wavemaker on one side. Depending on the length and width of the tank relative to the forcing frequency and water depth, i.e., on the degree of longitudinal (synchronous) and transverse (subharmonic) turning, the different possible orders of magnitudes of the longitudinal and transverse wave amplitudes relative to that of the paddle are systematically considered. Specifically, the following three sets of ordering are identified:

	wavemaker	longitudinal wave	transverse wave
case I	$O(\varepsilon)$	$O(\varepsilon^{1/3})$	$O(\varepsilon^{2/3})$
case II	$O(\varepsilon)$	$O(\varepsilon)$	$O(\varepsilon^{1/2})$
case III	$O(\varepsilon)$	$O(\varepsilon^{1/2})$	$O(\varepsilon^{1/2})$

where $\varepsilon = a/L \ll O(1)$ is the nondimensional amplitude of the wavemaker motion normalized by the length, L, of the tank. We remark that other order-of-magnitude orderings are in principle possible, for example, the somewhat 'obvious' choice of $O(\varepsilon^{1/3})$ for both the longitudinal and cross waves for case III. With that ordering, however, the requisite coupling occurs only at fifth order and the interactions between forced and parametric resonances are at higher order than the present case.

Case I corresponds to the case where the driving frequency of the wavemaker approximates a natural frequency of the longitudinal standing waves but is not close to twice that of a standing cross wave. The longitudinal standing wave is synchronously forced and resonated while the cross wave is not resonant and is of higher order in amplitude. Case II is the opposite situation where the subharmonic cross waves only are parametrically resonated. The longitudinal waves are not close to resonance, are of higher order, and do not affect the transverse wave motion in this case, as shown by Garrett (1970). The relevant evolution equations governing the amplitudes of the resonant waves for these two cases can be derived using the method of multiple scales. The derivation and results for both cases (§§3 and 4) are similar to a number of existing results for related problems. The results for the more straight-forward case I appear to have been obtained in the present context using multiple scales for the first time. For the cross waves case II, our equation is isomorphic to that of Miles (1988) using the averaged Lagrangian method. In order to make comparisons to experiments, we consider general finite water depth and *no* approximation is used for the shape function of the wavemaker motion, in contrast to the existing analyses of Lin & Howard (1960) and Miles (1988). In both cases I and II, the response amplitudes of the stationary wave motions, obtained readily from the evolution equations, compare well with the measurements of Lin & Howard (1960). We also discuss the particular depths at which the third order asymptotic analyses break down. To obtain uniformly valid descriptions at these particular depths we carry out the perturbation analyses to fifth order and derive the appropriate evolution equations in both cases.

Case III is new and represents the situation when the driving frequency approximates both a natural frequency of the directly forced longitudinal standing wave and twice that of the standing cross wave. The forced resonant longitudinal and parametrically resonant cross waves are of the same order of magnitude and the internal interactions between the two orthogonal waves become significant. For a broad range of physical parameters (water depth, wavemaker amplitude, width-to-length ratio and frequency detuning), these interactions are shown to lead to chaotic wave motions. We derive the evolution equations governing the amplitudes of the longitudinal and transverse waves for such three-dimensional interactions in §5.1. In order to account for the two resonances caused by the wavemaker, which are involved at different orders, two long timescales are employed in the perturbation analysis. The equilibrium states (stationary solutions) of the evolution equations and their local stability are discussed in §5.2. Numerical simulations of the evolutions are performed in §5.3, and sample results showing temporal chaotic motions in a number of resonance conditions are presented. The chaotic nature of the evolutions are further confirmed through estimates of the Lyapunov characteristic exponents and power spectra of the amplitudes.

In view of the number of physical parameters involved, and to obtain a *global* criterion for the likelihood of widespread chaotic behavior, we adopt the resonance overlap approximation of Chirikov (1979) to the present problem in §6. The method attributes the destruction of tori and the onset of widespread chaotic motion to what is known as the overlapping of primary resonances in Hamiltonian systems. An estimate in terms of the physical parameters can be obtained to predict the transition from predominantly regular to predominantly irregular (chaotic) motions in dynamic system. This approach is shown to yield remarkably good predictions of the global evolution behavior of the present system.

2. Formulation of the problem

We consider the fluid motion in a short rectangular wave tank with a wavemaker at rest at $x = 0$, a rigid bottom at $z = -H$, rigid walls at $x = L$ and $y = 0, W$, and a free surface with undisturbed position at $z = 0$. The wavemaker is subject to a harmonic motion given by,

$$x = \chi(z,t) = aF(z)\cos\omega_e t, \tag{2.1}$$

where a and ω_e are respectively the amplitude and frequency of the wavemaker motion, and $F(z)$ its shape function normalized by $F(0) = 1$. For a flap-type wavemaker hinged at $z=-d\geq -H$, $F(z)=1+z/d$ for $0\geq z\geq -d$, and $F(z)=0$ for $-d\geq z\geq -H$; and for a piston wavemaker, $F(z) = 1$.

In what follows, all physical variables are nondimensionalized by the length of the tank L, and the time scale $2/\omega_e$. The fluid is assumed to be ideal and surface tension is ignored. For irrotational motion, the velocity potential $\Phi(x,y,z,t)$ and free surface elevation $\zeta(x,y,t)$ are then governed by the boundary-value problem:

$$\nabla^2\Phi = 0, \qquad (\chi < x < 1, \quad 0 < y < 1/\ell, \quad -h < z < \zeta) \tag{2.2a}$$

$$\frac{\partial\zeta}{\partial t} + \nabla\zeta\cdot\nabla\Phi - \frac{\partial\Phi}{\partial z} = 0 \qquad (z = \zeta), \tag{2.2b}$$

$$\frac{\partial\Phi}{\partial t} + \frac{1}{2}\nabla\Phi\cdot\nabla\Phi + 4N^2\mu\zeta = 0 \qquad (z = \zeta), \tag{2.2c}$$

$$\frac{\partial\Phi}{\partial x} = \frac{\partial\chi}{\partial t} + \frac{\partial\chi}{\partial z}\frac{\partial\Phi}{\partial z} \qquad (x = \chi = \varepsilon F(z)\cos 2t), \tag{2.2d}$$

$$\frac{\partial\Phi}{\partial x} = 0 \qquad (x = 1), \tag{2.2e}$$

$$\frac{\partial\Phi}{\partial y} = 0 \qquad (y = 0,\ 1/\ell), \tag{2.2f}$$

$$\frac{\partial\Phi}{\partial z} = 0 \qquad (z = -h), \tag{2.2g}$$

$$\int_0^{1/\ell}\int_0^1 \zeta(x,y,t)\ \mathrm{d}x\mathrm{d}y = 0, \tag{2.2h}$$

where $\ell = L/W$ is the length-to-width ratio of the tank, and $\varepsilon = a/L \ll O(1)$ measures the amplitude of the wave paddle motion. For convenience, N and μ are defined respectively as $N = \Omega_x/\omega_e \cong 1$ and $\mu = (n\pi \tanh n\pi h)^{-1} \equiv \mu_x$ or the problem of longitudinal standing waves only (case I); and $N = \Omega_y/\omega_e \cong 1/2$ and $\mu = (\ell\pi \tanh \ell\pi h)^{-1} \equiv \mu_y$ for the (first-mode) cross-wave problem (case II). Ω_x and Ω_y are the linear natural frequencies of the longitudinal (x) and transverse (y) standing waves, respectively; and n is the mode number of the longitudinal standing wave.

We introduce perturbation expansions for Φ and ζ:

$$\Phi = \sum_{j=1}^{\infty} \varepsilon^{jv} \Phi_j, \qquad \zeta = \sum_{j=1}^{\infty} \varepsilon^{jv} \zeta_j, \tag{2.3a,b}$$

where the constant $v > 0$ provides the ordering depending on the problem to be solved. For the Laplace equation and all of the linear boundary conditions in (2.2), Φ_j and ζ_j satisfy the same form of the equations as Φ and ζ. Expanding the free surface boundary conditions (2.2*b,c*) in Taylor series about $z = 0$ and substituting the perturbation expansions (2.3) for Φ and ζ, we obtain to the first three orders the following results for the free-surface boundary conditions. For the kinematic boundary condition (2.2*b*):

$$\frac{\partial \zeta_j}{\partial t} - \frac{\partial \Phi_j}{\partial z} = F_j \qquad (z = 0), \qquad j = 1, 2, \ldots, \tag{2.4}$$

where

$$F_1 = 0, \tag{2.4a}$$

$$F_2 = -\nabla\zeta_1 \cdot \nabla\Phi_1 + \zeta_1 \frac{\partial^2 \Phi_1}{\partial z^2}, \tag{2.4b}$$

$$F_3 = -\nabla\zeta_1 \cdot \nabla\Phi_2 - \nabla\zeta_2 \cdot \nabla\Phi_1 + \zeta_1 \frac{\partial^2 \Phi_2}{\partial z^2} + \zeta_2 \frac{\partial^2 \Phi_1}{\partial z^2} - \zeta_1 \cdot \nabla\zeta_1 \cdot \nabla\left(\frac{\partial \Phi_1}{\partial z^3}\right) + \frac{1}{2}\zeta_1^2 \frac{\partial^3 \Phi_1}{\partial z^3}; \tag{2.4c}$$

and for the dynamic boundary condition (2.2*c*):

$$\frac{\partial \Phi_j}{\partial t} + 4N^2 \mu \zeta_j = G_j \qquad (z = 0), \qquad j = 1, 2, \ldots, \tag{2.5}$$

where

$$G_1 = 0, \tag{2.5a}$$

$$G_2 = -\zeta_1 \frac{\partial^2 \Phi_1}{\partial t \partial z} - \frac{1}{2} \nabla \Phi_1 \cdot \nabla \Phi_1, \tag{2.5b}$$

$$G_3 = -\zeta_1 \frac{\partial^2 \Phi_2}{\partial t \partial z} - \zeta_2 \frac{\partial^2 \Phi_1}{\partial t \partial z} - \nabla \Phi_1 \cdot \nabla \Phi_2 + \zeta_1 \cdot \nabla \Phi_1 \cdot \nabla (\frac{\partial \Phi_1}{\partial z}) - \frac{1}{2} \zeta_1^2 \frac{\partial^3 \Phi_1}{\partial t \partial z^2}. \tag{2.5c}$$

The wavemaker boundary conditions for Φ_j are similarly obtained by expanding (2.2d) about $x = 0$ and substituting (2.3a) for Φ. The appearance of forcing due to the wavemaker depends on the specific ordering of the problem. For the resonant longitudinal standing wave only case (case I), the boundary conditions at $x = 0$ at the first two orders are homogeneous:

$$\frac{\partial \Phi_j}{\partial x} = 0 \qquad (x = 0), \qquad j = 1, 2, \tag{2.6a}$$

and an inhomogeneous forcing term appears only at third order, $O(\varepsilon)$, for Φ_3:

$$\frac{\partial \Phi_3}{\partial x} = \frac{\partial \chi}{\partial t} \qquad (x = 0). \tag{2.6b}$$

For the resonant cross-wave only case (case II) and for the three-dimensional motion case (case III), the wavemaker boundary conditions for Φ_1 and Φ_2 are respectively (2.6a) and (2.6b). The boundary condition for Φ_3 for these two cases is given by:

$$\frac{\partial \Phi_3}{\partial x} = -\chi \frac{\partial^2 \Phi_0}{\partial x^2} + \frac{\partial \chi}{\partial z} \frac{\partial \Phi_0}{\partial z} \qquad (x = 0). \tag{2.6c}$$

3. Synchronous resonantly forced longitudinal standing waves

If the excitation frequency of the wavemaker is approximately equal to a natural frequency of longitudinal standing wave in the tank (say, the nth spatial harmonic mode), but the length-to-width ratio ℓ is not close to an integral multiple of 1/4 (for moderately deep water), then only the longitudinal wave is resonantly excited by the motion of the wavemaker. The transverse waves are of higher order in amplitude ($O(\varepsilon^{2/3})$) compared to the longitudinal standing waves ($O(\varepsilon^{1/3})$) and do not interact with the longitudinal wave motion. In this case, the appropriate choice for the long timescale is $\tau = \varepsilon^{2/3}t$. We further define the excitation frequency as $N = \Omega_x/\omega_e = 1 + \varepsilon^{2/3}\lambda_x$, where λ_x is the detuning parameter between the wavemaker frequency and the linear resonance frequency of the longitudinal standing wave.

Processing the boundary-value problem at successive orders, at the leading ($O(\varepsilon^{1/3})$) and second ($O(\varepsilon^{2/3})$) orders, the boundary conditions at the wavemaker are homogeneous and the velocity potential Φ_1 and Φ_2 and the free surface elevation ζ_1 and ζ_2 can be solved readily. The aim is to obtain the equation governing the evolution of the complex amplitude envelope $A(\tau)$ of the first-order motion:

$$\Phi_1 = [A(\tau)e^{-\mathrm{i}2t} + \text{c.c.}]\ \cos n\pi x\ \frac{\cosh n\pi(z+h)}{n\pi \sinh n\pi h}, \tag{3.1}$$

where c.c. stands for complex conjugate of the preceding term. At the third order, $O(\varepsilon)$, an inhomogeneous wavemaker boundary condition appears:

$$\frac{\partial \Phi_3}{\partial x} = \frac{\partial \chi}{\partial t} = -\mathrm{i}(e^{-\mathrm{i}2t} - \text{c.c.})\ F(z) \qquad (x = 0). \tag{3.2}$$

To remove this inhomogeneous condition from the wall boundary, we decompose the total potential Φ_3 into two parts (Havelock 1929; Ursell, Dean & Yu 1959):

$$\Phi_3 = \phi_3 - \mathrm{i}(e^{-\mathrm{i}2t} - \text{c.c.})\ \varphi(x,z), \tag{3.3a}$$

where $\varphi(x,z)$ satisfies the Laplace equation and homogeneous boundary conditions on the stationary walls and the bottom, and $\partial\varphi/\partial x = F(z)$ on the wavemaker $x = 0$.

For a flap-type wavemaker hinged at $z = -h$, such as those in the experiments of Lin & Howard, φ is given by (see Appendix A)

$$\begin{aligned}\varphi(x,z) =& \frac{8h^2}{\pi^3}\sum_{m=0}^{\infty}\left[\frac{\sin\frac{(2m+1)\pi}{2h}z}{(2m+1)^3}\right] \\ &+ \frac{16h^2}{\pi^3}\sum_{n=1}^{\infty}\sum_{m=0}^{\infty}\left[\frac{\sin\frac{(2m+1)\pi}{2h}z}{(2m+1)[(2m+1)^2+4n^2h^2]}\right]\cos n\pi x \\ &+ \frac{4h^2}{\pi^4}\sum_{m=0}^{\infty}\left[\frac{\cos\frac{(2m+1)\pi}{h}(z+h)}{(2m+1)^4}\right] \\ &+ \frac{8h^2}{\pi^4}\sum_{n=1}^{\infty}\sum_{m=0}^{\infty}\left[\frac{\cos\frac{(2m+1)\pi}{h}(z+h)}{(2m+1)^2[(2m+1)^2+n^2h^2]}\right]\cos n\pi x. \qquad (3.3b)\end{aligned}$$

Substituting (3.3) into the third-order free-surface boundary conditions (2.4) and (2.5), and suppressing the secularity for ϕ_3 and ζ_3, we obtain finally the evolution equation for $A(\tau)$:

$$\mu_x\frac{\mathrm{d}A}{\mathrm{d}\tau} + \mathrm{i}2\lambda_x\mu_x A + \frac{1}{4}\delta - \mathrm{i}\Gamma_a A^2A^\star = 0, \qquad (3.4)$$

where

$$\delta = \frac{8}{n^2\pi^2} - \frac{8}{n^3\pi^3 h}\tanh\frac{n\pi h}{2}, \qquad (3.5a)$$

and

$$\Gamma_a = \frac{1}{32\mu_x}(2 + 3n^2\pi^2\mu_x^2 + 12n^4\pi^4\mu_x^4 - 9n^6\pi^6\mu_x^6). \qquad (3.5b)$$

The frequency of the longitudinal standing wave is exactly equal to the frequency of the wavemaker motion and its amplitude is a function of that forcing frequency. This is the so-called *non-isochronicity* property for nonlinear oscillators. The amplitude and stability of the stationary solutions of (3.4) are readily obtained. The amplitudes of stationary responses as a function of detuning λ_x, are thus similar to those of an undamped Duffing equation with a change from a 'softening-spring' ($\Gamma_a > 0$) to a 'hardening-spring' ($\Gamma_a < 0$) system as the depth h decreases through the critical depth, $h = h^\star$ (Tadjbakhsh & Keller 1960; Fultz 1962).

At $h = h^*, \Gamma_a = 0$, and the perturbation analysis above breaks down. For h near h^*, then, we expand Φ and ζ as perturbation series in powers of $\varepsilon^{1/5}$, choose $N = 1 + \varepsilon^{4/5}\lambda_x$, and process the perturbation analysis to fifth order. Instead of the cubic nonlinear equation (3.4) for A, we obtain at the fifth order, an evolution equation with quintic nonlinearity:

$$\mu_x \frac{\mathrm{d}A}{\mathrm{d}\tau} + \mathrm{i}2\lambda_x\mu_x A + \frac{1}{4}\delta - \mathrm{i}\overline{\Gamma}_a A^3 A^{*2} = 0, \tag{3.6a}$$

where

$$\overline{\Gamma}_a = \frac{n^2\pi^2}{128\mu_x}\left[\frac{1151}{6} - \frac{7509}{8}n^2\pi^2\mu_x^2 + \frac{52919}{48}n^4\pi^4\mu_x^4 + \frac{14683}{24}n^6\pi^6\mu_x^6 - \frac{6093}{8}n^8\pi^8\mu_x^8 + 45n^{10}\pi^{10}\mu_x^{10} + \frac{2565}{16}n^{12}\pi^{12}\mu_x^{12}\right]. \tag{3.6b}$$

This quintic nonlinear equation is valid for $|h - h^*| \leq 0(\varepsilon^{2/5})$ for $\lambda_x \leq O(1)$.

When the natural frequency of an mth spatial harmonic wave becomes an integral multiple of that of the fundamental nth harmonic ($m \neq n$) at certain values of λ, the first-order solution above becomes non-unique (Tadjbakhsh & Keller 1960). Physically, at these depths both the nth and mth spatial harmonics are excited at first order, and there is an internal resonance between the two waves. The coupling interaction of such internal resonance is cubic nonlinear, and the equations governing the evolution of these internal resonant waves can be derived in a similar manner.

Finally, we show the comparisons between the present analytic results and Lin & Howard's (1960) experimental measurements. Figures 1 plot the frequency–amplitude relation for the stationary resonantly forced longitudinal standing waves. The circles represent the experimental measurements, and the solid and broken lines are stable and unstable stationary solutions respectively of (3.4). The amplitudes of the excitation are given by the maximum deflection, θ, of the wavemaker according to Lin & Howard. Figure 1(a) is for tank dimension $L = 18$ in., $H = 24$ in. and $2\theta = 0.566°$, and the resonant motion is the first mode (n=1) standing wave. The comparisons between the theoretical and experimental results are remarkably good

for the entire range of detuning frequency. Figure 1(b) is for the case $L = 29.5$ in., $H = 24$ in., $2\theta = 0.935°$, and the resonant standing wave is the second mode (n=2). The comparisons are fairly good except for large detuning values where the total response is small and other modes may have begun to participate. For the present case, Lin & Howard (1960) also obtained theoretical results using a direct perturbation expansion similar to that of Penney & Price (1952). The resulting analysis was fairly involved and they were only able to obtain results for the first-mode ($n = 1$) resonance and for deep water. Because of this, and possibly also due to algebraic errors, their comparison to the $n = 1$ case (figure 1a) was not as satisfactory.

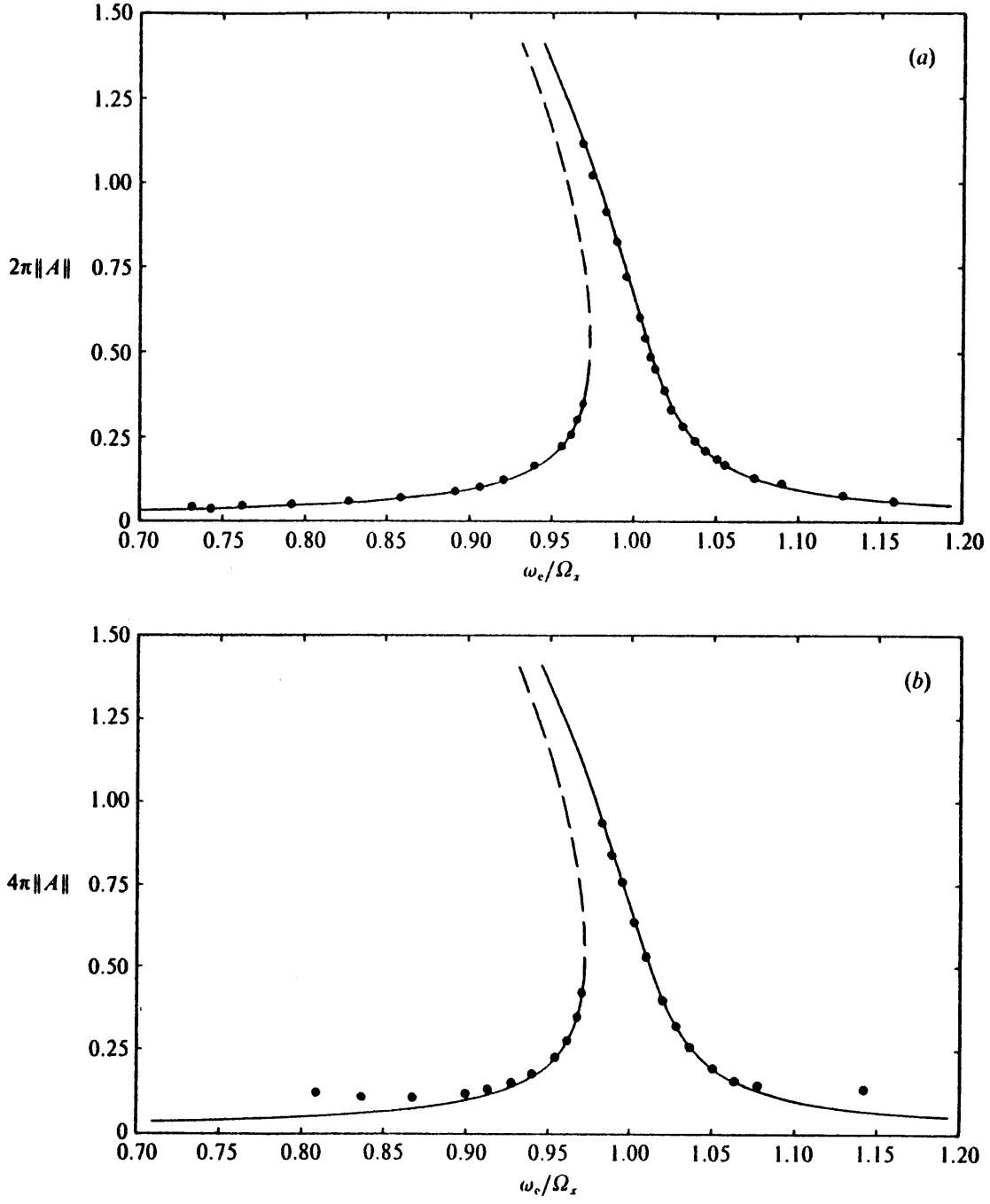

Figure 1. Comparisons of the frequency-response relationship for stationary longitudinal waves between the present analytic results (solid lines for stable and broken lines for unstable responses) and Lin & Howard's (1960) experimental measurements (circles) for (*a*) $n = 1$, $L = 18$ in., $H = 24$ in., $2\theta = 0.566°$; and (*b*) $n = 2$, $L = 29.5$ in., $H = 24$ in., $2\theta = 0.935°$.

4. Subharmonic parametrically resonant transverse standing waves

When the wavemaker excitation is close to twice the frequency of a cross-tank standing wave but the length of the tank is such that the longitudinal standing wave is not resonant, the former is resonantly excited and the latter is of higher order in amplitude. Following the experiments and analysis of Lin & Howard (1960) for the problem, Garrett (1970) showed that the mechanism for cross-wave excitation is indeed one of parametric resonance characterized by forcing terms which appear as coefficients of the differential equation.

For this problem, we consider the 1/2 subharmonic parametric-resonant cross waves, choose the long timescale $\tau = \varepsilon t$ and define the transverse detuning λ_y as $N = \Omega_y/\omega_e = 1/2 + \varepsilon\lambda_y$. The length-to-width ratio ℓ is assumed to be far from integral multiples of 1/4 so that the longitudinal wave is not resonantly excited. Since the longitudinal wave is of higher order, at leading order, $O(\varepsilon^{1/2})$, the velocity potential Φ_1 is independent of x:

$$\Phi_1 = \frac{1}{2}[B(\tau)e^{-it} + \text{c.c.}]\ \cos \ell\pi y\ \frac{\cosh \ell\pi(z+h)}{\ell\pi \sinh \ell\pi h}, \tag{4.1}$$

where $B(\tau)$ is the complex amplitude envelope of the cross wave. At the next order, Φ_2 satisfies the inhomogeneous wavemaker boundary condition (3.2) at $x = 0$. The same procedure as (3.3) is applied and the second order Φ_2 and ζ_2 can be solved accordingly. Note that there is a mean set-up of $h(e^{-i2t} + \text{c.c.})/4$ in the second-order free-surface elevation which is equal to the fluid volume displaced by the wavemaker, $\int_{-h}^{0} \xi(z,t)\mathrm{d}z$. This mean free-surface elevation is the only contribution from the wavemaker at this order ($O(\varepsilon)$) which causes a secularity at the next order ($O(\varepsilon^{3/2})$) through its interaction with the transverse wave.

At third order, $O(\varepsilon^{3/2})$, the inhomogeneous wavemaker boundary condition is

$$\frac{\partial \Phi_3}{\partial x} = \frac{\partial \chi}{\partial z}\frac{\partial \Phi_1}{\partial z} \qquad (x = 0). \tag{4.2}$$

From (4.2), we see that the resonant excitation of the cross wave is caused directly by the interaction between the wavemaker motion and the transverse wave without involving the longitudinal waves. Again, we transform the inhomogeneous boundary condition by the substitution

$$\Phi_3 = \phi_3 + (B^\star e^{-\mathrm{i}t} + Be^{-\mathrm{i}3t} + \text{c.c.})\ \theta(x,z)\ \cos \ell\pi y, \tag{4.3a}$$

where

$$\theta(x,z) = \frac{\cosh \ell\pi h - 1}{\ell\pi^4 h^2 \sinh \ell\pi h} \sum_{m=0}^{\infty} \left[\frac{\sin m_1 \pi z}{2m+1} \left(\frac{1}{\ell^2 + m_1^2} + \frac{2}{\pi} \sum_{n=1}^{\infty} \frac{\cos n\pi x}{\ell^2 + m_1^2 + n^2} \right) \right]$$
$$- \frac{\ell}{2\pi^3 h^2 \sinh \ell\pi h} \sum_{m=0}^{\infty} \left[\frac{[(-1)^m \cosh \ell\pi h - 1] \cos m_2 \pi (z+h)}{\ell^2 + m_2^2} \right.$$
$$\left. \times \left(\frac{1}{\ell^2 + m_2^2} + \frac{2}{\pi} \sum_{n=1}^{\infty} \frac{\cos n\pi x}{\ell^2 + m_2^2 + n^2} \right) \right], \tag{4.3b}$$

and $m_1 = (2m+1)/2h$, $m_2 = m/h$. Combining the kinematic and dynamic free-surface boundary conditions for ϕ_3 and applying the solvability condition yields the evolution equation for $B(\tau)$:

$$\mu_y \frac{\mathrm{d}B}{\mathrm{d}\tau} + \mathrm{i}2\lambda_y \mu_y B - \mathrm{i}\beta B^\star - \mathrm{i}\Gamma_b B^2 B^\star = 0, \tag{4.4}$$

where

$$\beta = -\frac{1}{\mu_y}(1 + \ell^2\pi^2\mu_y^2)(f_0 - d_0) - \frac{1}{2}f_0' + \frac{\mu_y}{2}f_0'' + \frac{1}{4}g_0 - \frac{\mu_y}{4}g_0', \tag{4.5a}$$

$$\Gamma_b = \frac{1}{64\mu_y}(2 + 3\mu_y^2\ell^2\pi^2 + 12\mu_y^4\ell^4\pi^4 - 9\mu_y^6\ell^6\pi^6), \tag{4.5b}$$

$$f_0 = -\frac{h^2}{24}, \qquad f_0' = \frac{h}{2}, \qquad f_0'' = 1, \tag{4.5c,d,e}$$

$$g_0 = -\frac{1}{2\ell^2\pi^2 h} + \frac{1}{\ell^3\pi^3 h^2} \tanh \frac{\ell\pi h}{2}, \tag{4.5f}$$

$$g_0' = \frac{1}{\ell^2\pi^2 h^2} \tanh \ell\pi h\ \tanh \frac{\ell\pi h}{2}. \tag{4.5g}$$

The coefficient β of $B^\star$ in (4.4) represents the parametric resonance and is negative for all depths. Note that the f-terms in β come from the first-order wavemaker boundary condition, and are equivalent to those of Garrett's linear results obtained by averaging the longitudinal motions. The g-terms in β correspond to the second-order wavemaker boundary condition representing the direct interaction between the motions of the wavemaker and the cross wave. The primes on f and g denote respectively derivatives with respect to z of $\varphi(x,z)$ and $\theta(x,z)$; and the zero subscripts mean that only the constant terms in the series contribute to resonance. For example, g_0' is the contribution coming from the constant terms of $\partial\varphi/\partial z$ at $z=0$.

Equation (4.4) is isomorphic to equation (5.1) of Miles (1988) after a $\pi/4$ phase shift of his complex amplitude. Such type of equation also governs the evolution of 1/2-subharmonic free-surface resonance in a vertically oscillatory basin i.e., Faraday problem (Faraday 1831). In Appendix B, the Faraday problem for the interface of a two-layer stratified flow is considered and the details of the phase-plane trajectories and stability analysis of the stationary solutions of (4.4) are also given. For the stable response, the free surface is flat when the wavemaker reaches its outermost position; while for the unstable response the free surface is flat when the wavemaker is in its innermost position. This phase relation was also observed in Lin & Howard's experiments. Note that since β is negative in the whole range of water depth, the phase-plane trajectories of (4.4) correspond to a $\pi/2$ rotation of those in figures 17 of Appendix B. For periodic solutions, the evolution equation (4.4) can be integrated in closed form in terms of elliptic integrals. The details of solving the evolution equation governing parametric resonance are given in Appendix C.

Again, we note that there exists a depth $h=h^{\star\star}$ where $\Gamma_b(h^{\star\star})=0$, and the perturbation analysis above breaks down. To obtain a uniformly valid description near that depth, we expand Φ and ζ in powers of $\varepsilon^{1/4}$, and carry out the perturbation analysis to fifth order, $O(\varepsilon^{5/4})$. The final evolution equation is

$$\mu_y\frac{\mathrm{d}B}{\mathrm{d}\tau}+\mathrm{i}2\lambda_y\mu_y B-\mathrm{i}\beta B^\star-\mathrm{i}\overline{\Gamma}_b B^3 B^{\star^2}=0, \qquad (4.6a)$$

where

$$\overline{\Gamma}_b = \frac{\ell^2\pi^2}{1024\mu_y}\left[\frac{1151}{6} - \frac{7509}{8}\ell^2\pi^2\mu_y^2 + \frac{52919}{48}\ell^4\pi^4\mu_y^4 + \frac{14683}{24}\ell^6\pi^6\mu_y^6\right.$$

$$\left. - \frac{6093}{8}\ell^8\pi^8\mu_y^8 + 45\ell^{10}\pi^{10}\mu_y^{10}\frac{2526}{16}\ell^{12}\pi^{12}\mu_y^{12}\right]. \qquad (4.6b)$$

Finally, we compare the present results to the measurements of Lin & Howard (1960). Figures 2 show these comparisons for the frequency-amplitude relation of the stationary resonant cross waves. The dimensional parameters are $L = 7$ in., $2\theta = 0.287°$ (figure 2*a*) and $L = 8.75$ in., $2\theta = 0.279°$ (figure 2*b*) respectively, with $H = 24$ in. and $W = 24.1875$ in. in both cases. The present results are in reasonably good agreement with the experimental data but with a slight overprediction of the response amplitudes which may be due to the absence of dissipation in the present theoretical model.

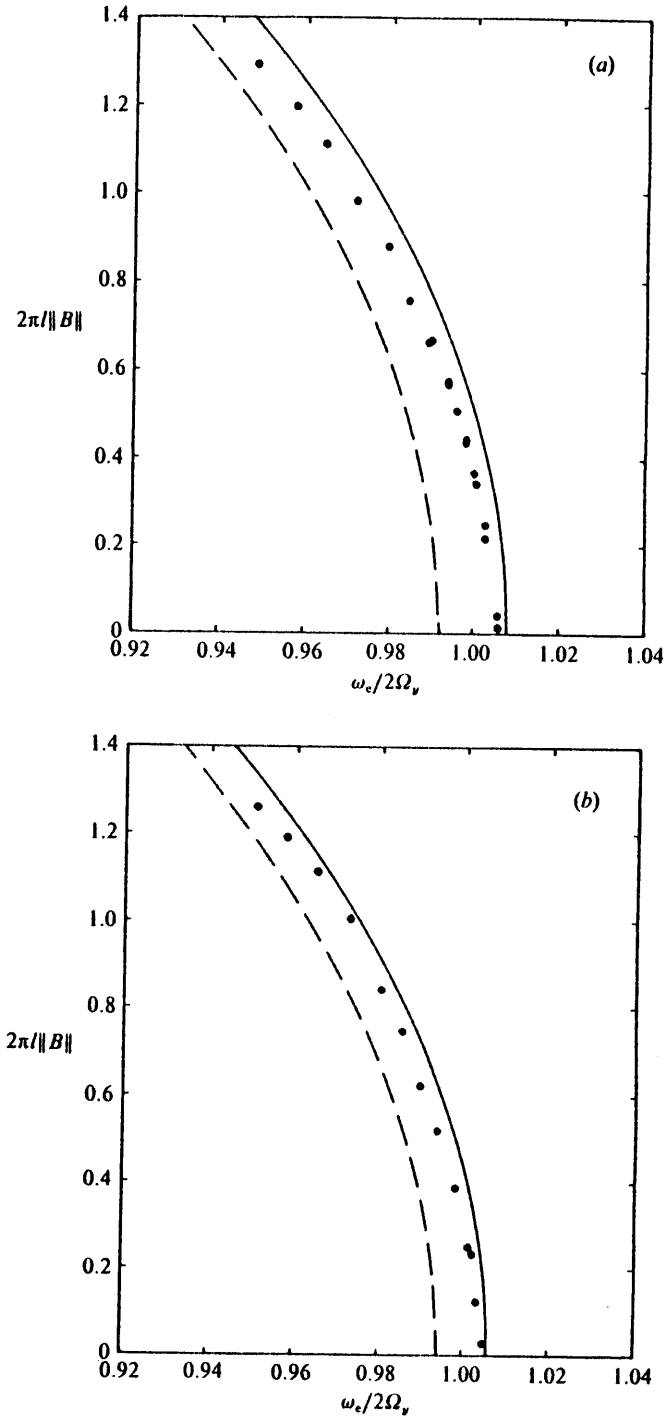

Figure 2. Comparisons of the frequency-response relationship for stationary cross waves between the present analytic results (solid lines for stable and broken lines for unstable responses) and Lin & Howard's (1960) experimental measurements (circles) for $H = 24$ in., $W = 24.1875$ in. and (*a*) $L = 7$ in., $2\theta = 0.287°$; and (*b*) $L = 8.75$ in., $2\theta = 0.279°$.

5. Interaction between resonant longitudinal and transverse standing waves

5.1. Evolution equations

When the excitation frequency of the wavemaker is approximately equal to the natural frequency of the longitudinal nth harmonic standing wave and the length-to-width ratio ℓ is close to $n/4$ (for first-mode cross-waves), the longitudinal wave is directly resonated by the wavemaker while the transverse wave is parametrically excited. Both waves are now of the same order of magnitude, $O(\varepsilon^{1/2})$, and internal interactions must be included. To account for the two resonances which are involved at different orders, two long timescales are introduced: $\tau_1 = \varepsilon^{1/2}t$ and $\tau_2 = \varepsilon t$. The relative degree of resonance between the wavemaker motion and the longitudinal and transverse standing waves are measured by $\Omega_y/\omega_e = 1/2 + \varepsilon^{1/2}\lambda$ and $\Omega_x/\Omega_y = 2 + \varepsilon^{1/2}\gamma$, where λ and γ are the detuning parameters.

The first-order velocity potential for this case of three-dimensional motion is

$$\Phi_1 = \left[A(\tau_1,\tau_2)e^{-\mathrm{i}(2+\gamma\varepsilon)t} + \text{c.c.}\right]\cos n\pi x\,\frac{\cosh n\pi(z+h)}{n\pi\sinh n\pi h}$$

$$+\frac{1}{2}\left[B(\tau_1,\tau_2)e^{-\mathrm{i}t} + \text{c.c.}\right]\cos n\pi y\,\frac{\cosh \ell\pi(z+h)}{\ell\pi\sinh \ell\pi h}. \tag{5.1}$$

At the second order, $O(\varepsilon)$, the inhomogeneous wavemaker boundary condition (3.2) results in a secular forcing which gives the following solvability condition for Φ_2:

$$\mu\frac{\partial A}{\partial\tau_1} + \mathrm{i}2\lambda\mu(2+\gamma\varepsilon^{1/2})A\ + (1+\gamma\varepsilon^{1/2})\,\delta e^{\mathrm{i}\gamma\tau_1} = 0, \tag{5.2a}$$

and

$$\mu\frac{\partial B}{\partial\tau_1} + \mathrm{i}2\lambda\mu B = 0, \tag{5.2b}$$

where $\mu \equiv \mu_y \cong 4\mu_x$ and δ is given in (3.5a). The higher order terms in the coefficients of (5.2a) come from expressing μ_x and μ_y in terms of the common μ and are retained to be consistent at the next order. Note that because of

the detuning between the natural frequencies of the longitudinal and cross waves, $\mu_y/\mu_x = (\Omega_x/\Omega_y)^2 = 4 + O(\varepsilon^{1/2})$, the corresponding error in the evolution equation at third order will be $O(\varepsilon^{1/2})$ if we replace μ_x by $\mu_y/4$ in the sequel. Applying (5.2a) and (5.2b) to the second-order boundary-value problem, we can solve for Φ_2 and ζ_2 (see Appendix D).

At third order, $O(\varepsilon^{3/2})$, the inhomogeneous wavemaker boundary condition (2.6c) appears. Since the first term of the forcing in (2.6c) does not cause resonant secularity, only the form of the boundary condition (4.2) needs to be considered and the same substitution as (4.3a) is used for Φ_3. Combining the free-surface boundary conditions, sorting out the secular forcing terms and invoking the solvability condition for Φ_3, we obtain the evolution equations with modulation time scale τ_2:

$$\mu\frac{\partial A}{\partial \tau_2} + \mathrm{i}4\lambda^2\mu A + \lambda\delta e^{\mathrm{i}\Gamma\tau_1} - \mathrm{i}\Gamma_a A^2 A^\star - \mathrm{i}\Sigma_a ABB^\star = 0, \tag{5.3a}$$

and

$$\mu\frac{\partial B}{\partial \tau_2} + \mathrm{i}2\lambda^2\mu B - \mathrm{i}\beta B^\star - \mathrm{i}\Gamma_b B^2 B^\star - \mathrm{i}\Sigma_b BAA^\star = 0, \tag{5.3b}$$

where δ is given by (3.5a), β by (4.5a), Γ_a is four times the expression of (3.5b), and Γ_b is the same as (4.5b). The coefficients Σ_a and Σ_b governing the nonlinear coupling between the longitudinal and transverse waves are given by

$$\Sigma_a = a_2\left[1 - \frac{1}{2}(\frac{n^2}{2} + \ell^2)\pi^2\mu\tilde{\mu}\right] + b_2\left[-1 + \frac{1}{2}(\frac{n^2}{2} - \ell^2)\pi^2\mu\tilde{\mu}\right] + \frac{1}{2}\tilde{a}_2 - \frac{1}{2}\tilde{b}_2 - \frac{1}{4}\pi^2\ell^2\mu, \tag{5.4a}$$

$$\Sigma_b = \frac{1}{2}\Sigma_a, \tag{5.4b}$$

where the coefficients a_2, b_2, $\tilde{a}_2$ and $\tilde{b}_2$ are given in Appendix D.

Equations (5.2) and (5.3) respectively govern the evolution of the first-order amplitudes with respect to τ_1 and τ_2, and A and B in general varies over both τ_1 and τ_2 (see figures 7 for some sample evolutions). Since τ_1 appears explicitly in (5.3a), it is more convenient to consider A and B as functions of τ_1 (only), and combine (5.2a,b) and (5.3a,b) into a single pair of equations. Defining $\tau_1 \equiv \tau$ for convenience, recalling the chain rule $(\partial/\partial\tau_1) + \varepsilon^{1/2}(\partial/\partial\tau_2) \to (\partial/\partial\tau)$, and factoring

out the modulation of the forcing in (5.2a) and (5.3a) by letting $A \equiv \sqrt{2}\tilde{A}e^{i\gamma\epsilon\tau}$, we obtain the final result:

$$\mu\frac{d\tilde{A}}{d\tau} + i\gamma_a\tilde{A} + \tilde{\delta} - i\tilde{\Gamma}_a\tilde{A}^2\tilde{A}^\star - i\tilde{\Sigma}_a\tilde{A}BB^\star = 0, \tag{5.5a}$$

and

$$\mu\frac{dB}{d\tau} + i\gamma_b B - i\tilde{\beta}B^\star - i\tilde{\Gamma}_b B^2 B^\star - i\tilde{\Sigma}_b B\tilde{A}\tilde{A}^\star = 0. \tag{5.5b}$$

where

$$\gamma_a = \mu[4\lambda + \gamma + 2\varepsilon^{1/2}(\lambda\gamma + 2\lambda^2)], \qquad \gamma_b = 2\mu[\lambda + \varepsilon^{1/2}\lambda^2], \tag{5.6a,b}$$

$$\tilde{\delta} = \frac{\delta}{\sqrt{2}}[1 + \varepsilon^{1/2}(\gamma + \lambda)], \qquad \tilde{\beta} = \varepsilon^{1/2}\beta, \tag{5.6c,d}$$

$$\tilde{\Gamma}_a = 2\varepsilon^{1/2}\Gamma_a, \qquad \tilde{\Gamma}_b = \varepsilon^{1/2}\Gamma_b, \tag{5.6e,f}$$

$$\tilde{\Sigma}_a = \varepsilon^{1/2}\Sigma_a = 2\varepsilon^{1/2}\Sigma_b = \tilde{\Sigma}_b \equiv \tilde{\Sigma}. \tag{5.6g}$$

The evolution equation (5.5a) reduces to that of (3.4) for the longitudinal wave amplitude in the absence of the transverse wave, and the transverse wave equation (5.5b) reduces to that of (4.4) if the longitudinal motions are small.

If we write $\tilde{A} \equiv C_a + iD_a$ and $B \equiv C_b + iD_b$, (5.5a,b) can be represented as an autonomous Hamiltonian system with the Hamiltonian $\mathcal{H}$ given by

$$\mathcal{H} = -\frac{1}{\mu}\left[\tilde{\delta}D_a + \frac{1}{2}\tilde{\beta}(C_b^2 - D_b^2) - \frac{1}{2}\gamma_a(C_a^2 + D_a^2) + \frac{1}{4}\tilde{\Gamma}_a(C_a^2 + D_a^2)^2 \right.$$
$$\left. - \frac{1}{2}\gamma_b(C_b^2 + D_b^2) + \frac{1}{4}\tilde{\Gamma}_b(C_b^2 + D_b^2)^2 + \frac{1}{2}\tilde{\Sigma}(C_a^2 + D_a^2)(C_b^2 + D_b^2)\right] \tag{5.7}$$

The conjugate variables, C_a, D_a and C_b, D_b satisfy the Hamiltonian equations

$$\frac{dC_{a,b}}{d\tau} = \frac{\partial\mathcal{H}}{\partial D_{a,b}}, \quad \text{and} \quad \frac{dD_{a,b}}{d\tau} = -\frac{\partial\mathcal{H}}{\partial C_{a,b}}. \tag{5.8a,b}$$

The Hamiltonian system (5.8) is invariant under the reflection $(C_b, D_b) \to -(C_b, D_b)$ by virtue of symmetry with respect to the centreplane of the wave tank $y = W/2$.

The coefficients $\Gamma_{a,b}$ and $\Sigma_{a,b}$ of the cubic nonlinear terms in the evolution equations, which govern the self and internal interactions respectively, are functions

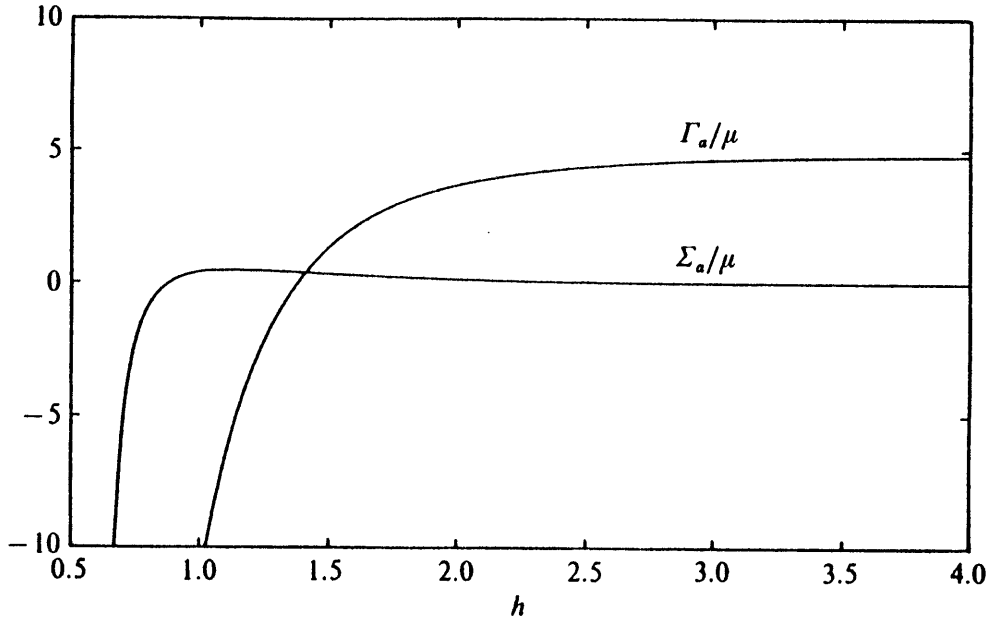

Figure 3. Parameters Γ_a/μ and Σ_a/μ plotted against water depth h for $n = 1$ and $\ell = 0.248062$.

of the length-to-width ratio ℓ, longitudinal wave number n, and water depth h. Figure 3 shows Γ_a/μ and Σ_a/μ as the functions of h for $n = 1$ and $\ell = 6.0/24.1875 \cong 0.248062$ (a value corresponding to that of RUN 101 in Lin and Howard's experiment). For shallow depths, the magnitudes of Γ_a and Σ_a become much larger than $O(1)$ and the present perturbation analysis becomes invalid. For deep water, Γ_a is $O(1)$ while Σ_a approaches a small value, and the interaction between the longitudinal and cross waves becomes weak. The internal interaction is strongest around intermediate depths, where the magnitudes of Γ_a and Σ_a are comparable. For higher n with the corresponding ℓ, the coefficients of the nonlinear terms have behavior similar to that for the $n = 1$ mode.

5.2. *Stationary solutions and bifurcation diagrams*

The stationary solutions of the evolution equations (5.8a,b) are obtained by solving a system of cubic equations, and are given by:

$$\left\{\begin{array}{l} C_{a0}=0, \quad C_{b0}=0, \quad D_{b0}=0, \\ \tilde{\Gamma}_a D_{a0}^3-\gamma_a D_{a0}+\tilde{\delta}=0, \end{array}\right\} \tag{5.9a}$$

$$\left\{\begin{array}{l} C_{a0}=0, \quad D_{b0}=0, \\ D_{a0}^3+\dfrac{[\tilde{\Gamma}_b\gamma_a-\tilde{\Sigma}_a(\gamma_b-\tilde{\beta})]}{\Xi_{ab}}D_{a0}-\dfrac{\tilde{\delta}\tilde{\Gamma}_b}{\Xi_{ab}}=0, \\ C_{b0}=\pm\sqrt{\dfrac{(\gamma_b-\tilde{\beta})-\tilde{\Sigma}_b D_{a0}^2}{\tilde{\Gamma}_b}}, \end{array}\right\} \tag{5.9b}$$

$$\left\{\begin{array}{l} C_{a0}=0, \quad C_{b0}=0, \\ D_{a0}^3+\dfrac{[\tilde{\Gamma}_b\gamma_a-\tilde{\Sigma}_a(\gamma_b+\tilde{\beta})]}{\Xi_{ab}}D_{a0}-\dfrac{\tilde{\delta}\tilde{\Gamma}_b}{\Xi_{ab}}=0, \\ D_{b0}=\pm\sqrt{\dfrac{(\gamma_b+\tilde{\beta})-\tilde{\Sigma}_b D_{a0}^2}{\tilde{\Gamma}_b}}, \end{array}\right\} \tag{5.9c}$$

where $\Xi_{ab}\equiv\tilde{\Sigma}_a\tilde{\Sigma}_b-\tilde{\Gamma}_a\tilde{\Gamma}_b$. The solutions (5.9$a$) correspond to the two-dimensional longitudinal waves of §3, while (5.9b,c) are the stationary three-dimensional wave solutions arising from the coupling between the forced longitudinal wave and the parametrically excited transverse wave.

Stability of these stationary solutions are determined by the real parts of all the eigenvalues ω of the equation

$$F(\omega)=\parallel \underline{\underline{M}}(\underline{X}=\underline{X}_0)-\mu\omega\underline{\underline{I}} \parallel =0, \tag{5.10}$$

where $\underline{X}\equiv(C_a,D_a,C_b,D_b)$, $\underline{\underline{M}}\equiv\partial\underline{S}/\partial\underline{X}$, $\underline{S}\equiv\nabla_{\underline{X}}\mathcal{H}$, and $\underline{\underline{I}}$ is the unit matrix. One property of (5.10) is that if ω is an eigenvalue, so is $-\omega$. Therefore a stationary solution is stable if, and only if, the eigenvalue ω is pure imaginary.

For the two-dimensional solution (5.9a), the eigenvalue equation (5.10) can be simplified as

$$F(\omega) = [\mu^2\omega^2 + (3\tilde{\Gamma}_a D_{a0}^4 - 4\gamma_a\tilde{\Gamma}_a D_{a0}^2 + \gamma_a^2)] \times [\mu^2\omega^2 + (\tilde{\Sigma}_b D_{a0}^4 - 2\gamma_b\tilde{\Sigma}_b D_{a0}^2 + \gamma_b^2 - \tilde{\beta}^2)] = 0. \quad (5.11)$$

The stationary solution is stable if, and only if, $(3\tilde{\Gamma}_a D_{a0}^4 - 4\gamma_a\tilde{\Gamma}_a D_{a0}^2 + \gamma_a^2) > 0$ and $(\tilde{\Sigma}_b D_{a0}^4 - 2\gamma_b\Sigma_b D_{a0}^2 + \gamma_b^2 - \tilde{\beta}^2) > 0$. The first condition determines the stability of the stationary longitudinal wave subject to perturbations in the longitudinal direction. This type of bifurcation corresponds to the turning point. The second inequality refers to the stability of the stationary longitudinal wave subject to transverse perturbations. This is the so-called pitchfork bifurcation which determines the incidence of three-dimensional wave motions. The bifurcation of the two-dimensional transverse wave in §4 is a special case of this kind of bifurcation which bifurcates from the state $D_{a0} = 0$.

For the three-dimensional stationary waves (5.9b) and (5.9c), (5.10) becomes

$$F(\omega) = \mu^4\omega^4 + F_2\mu^2\omega^2 + F_0 = 0, \quad (5.12)$$

where

$$F_2 = D_{a0}^4(\tilde{\Sigma}_b^2 + 3\tilde{\Gamma}_a^2) + \binom{C_{b0}^4}{D_{b0}^4}(\tilde{\Sigma}_a^2 + 3\tilde{\Gamma}_b^2) + \binom{C_{b0}^2}{D_{b0}^2} D_{a0}^2(4\tilde{\Gamma}_b\tilde{\Sigma}_b + 4\tilde{\Gamma}_a\tilde{\Sigma}_a) + D_{a0}^2(-2\gamma_b\tilde{\Sigma}_b - 4\gamma_a\tilde{\Gamma}_a) + \binom{C_{b0}^2}{D_{b0}^2}[-2\gamma_a\tilde{\Sigma}_a - (4\gamma_b \pm 2\tilde{\beta})\tilde{\Gamma}_b] + \gamma_a^2 + \gamma_b^2 - \tilde{\beta}^2, \quad (5.13a)$$

and

$$F_0 = \pm 2\tilde{\beta}(\tilde{\Gamma}_a D_{a0}^2 + \tilde{\Sigma}_a C_{b0}^2 - \gamma_a)\Big\{-\gamma_a(\gamma_b \mp \tilde{\beta}) + D_{a0}^4(-3\tilde{\Gamma}_a\tilde{\Sigma}_b) + \binom{C_{b0}^4}{D_{b0}^4}(-3\tilde{\Gamma}_b\tilde{\Sigma}_a) + \binom{C_{b0}^2}{D_{b0}^2} D_{a0}^2(3\tilde{\Sigma}_a\tilde{\Sigma}_b - 9\tilde{\Gamma}_a\tilde{\Gamma}_b) + D_{a0}^2[\gamma_a\tilde{\Sigma}_b + (3\gamma_b \mp 3\tilde{\beta})\tilde{\Gamma}_a] + \binom{C_{b0}^2}{D_{b0}^2}[(\gamma_b \mp \tilde{\beta})\tilde{\Sigma}_a + 3\gamma_a\tilde{\Gamma}_b]\Big\}. \quad (5.13b)$$

The upper and lower expressions in (5.13a) and (5.13b) correspond to the stationary solutions (5.9b) and (5.9c), respectively. The necessary and sufficient conditions for (5.12) to have pure imaginary solutions ω, i.e. for the critical points to be stable, are $F_2 > 0$, $F_0 > 0$ and $F_2^2 - 4F_0 > 0$.

The system (5.8) has a total of five parameters: h, ℓ, λ, ε and n. For a given tank dimension and wavemaker amplitude, h, ℓ, ε and n are constant. We thus perform the bifurcation analysis of codimension-one in terms of the detuning λ of the excitation frequency. Figures 4 show the bifurcation diagram of the amplitude of the stationary solution, $[(C_{a0}^2 + D_{a0}^2) + 0.5(C_{b0}^2 + D_{b0}^2)]^{1/2}$, as a function of the detuning parameter λ, for $\ell = 0.248062$, $n = 1$, $\varepsilon = 0.009072$ and different water depths, $h = 1.5$, 1.6, 1.7, 1.9, 2.2, 4.0. The solid and broken lines in the figures represent respectively the stable centers and unstable saddle points of the stationary solutions. The branches labelled (a), (b), and (c) correspond to the families (5.9a), (5.9b) and (5.9c) respectively.

The features of the bifurcation diagrams change abruptly around the intermediate depths, $h = 1.5 - 1.9$. For h greater than 2.5, the bifurcation diagrams are qualitatively similar to that of the $h = 4.0$ case. For $h = 1.5$ and 1.6, a three-dimensional wave family, branch (b_3), bifurcates from the family of two-dimensional longitudinal waves (a_3). Along this three-dimensional family, both longitudinal and transverse components grow with increasing detuning λ, but the transverse wave increases at a faster rate. Stability of this three-dimensional wave is lost when the transverse wave grows to about one order of magnitude greater than the longitudinal wave, and the wave motion becomes essentially that of a two-dimensional cross wave.

Figure 5 shows the real and imaginary parts of the eigenvalue ω along the branch (b_3) for $h = 1.6$. The branch starts at the pitchfork bifurcation point $\lambda = \lambda_1$ where a pair of pure imaginary eigenvalues separate into two pairs along the imaginary ω axis. These two pairs of ω coalesce in pairs again along the imaginary axis at $\lambda = \lambda_2$ and then split into two complex conjugate pairs leaving the imaginary

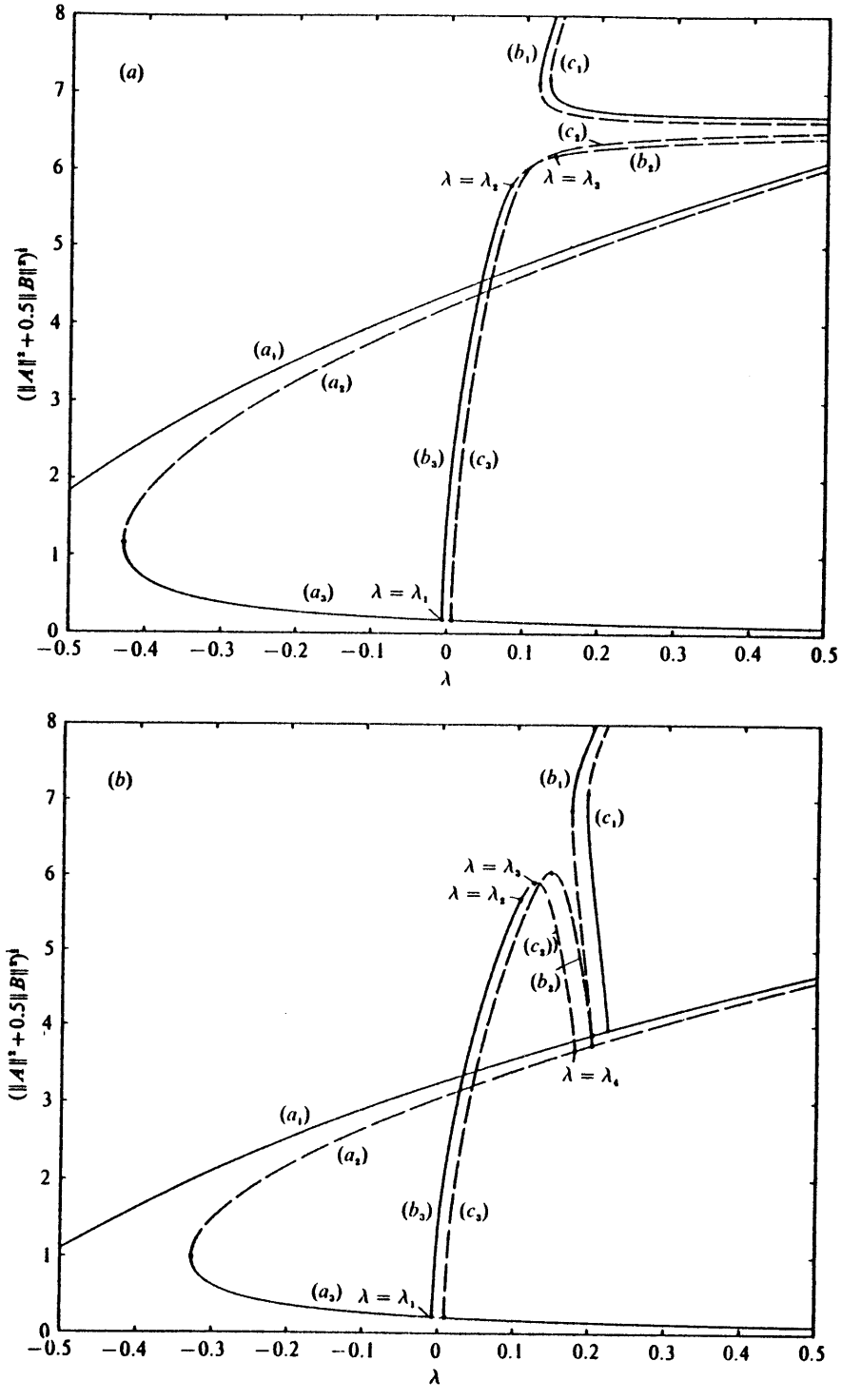

Figure 4(a, b). For caption see following page.

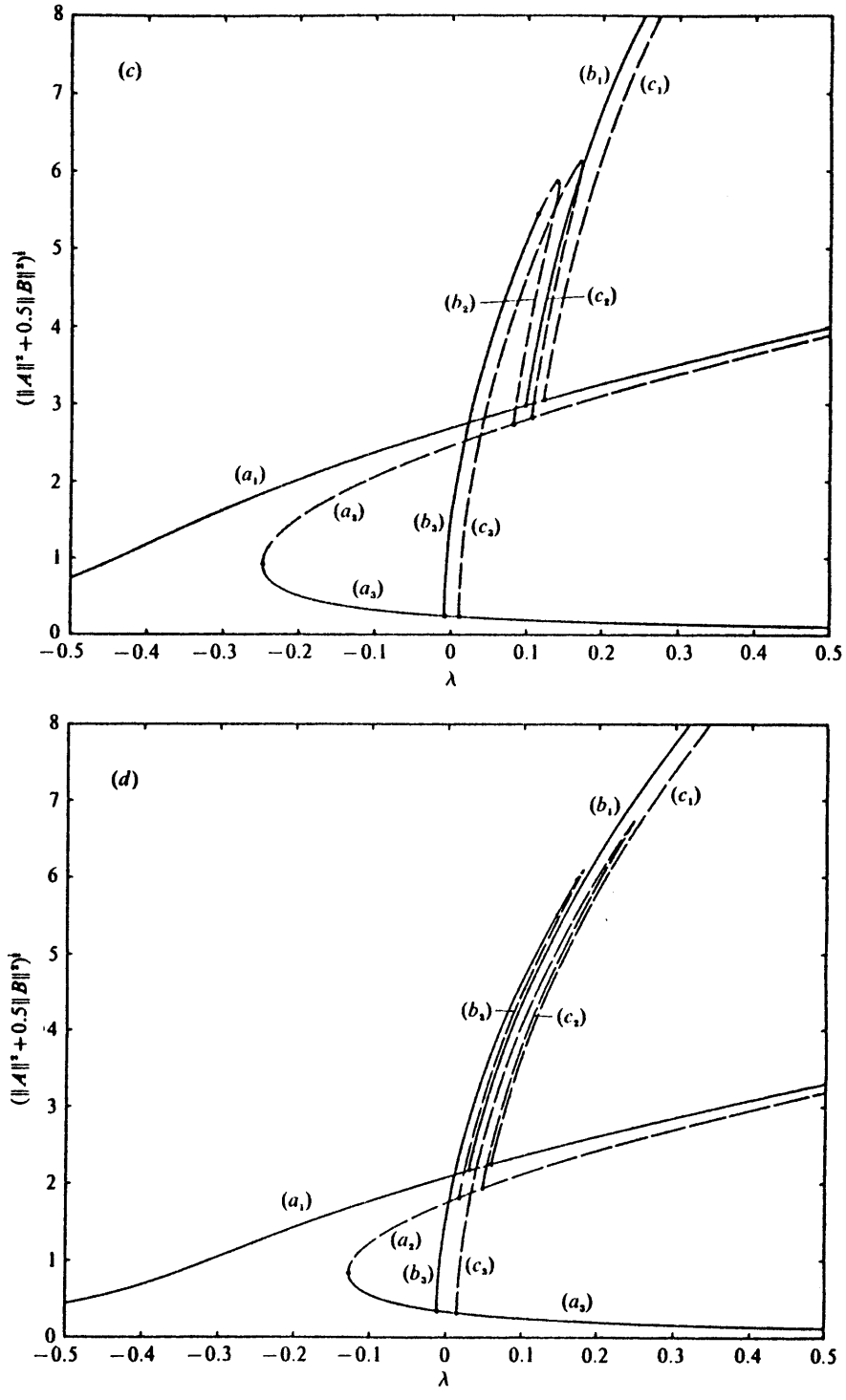

Figure 4(c, d). For caption see following page.

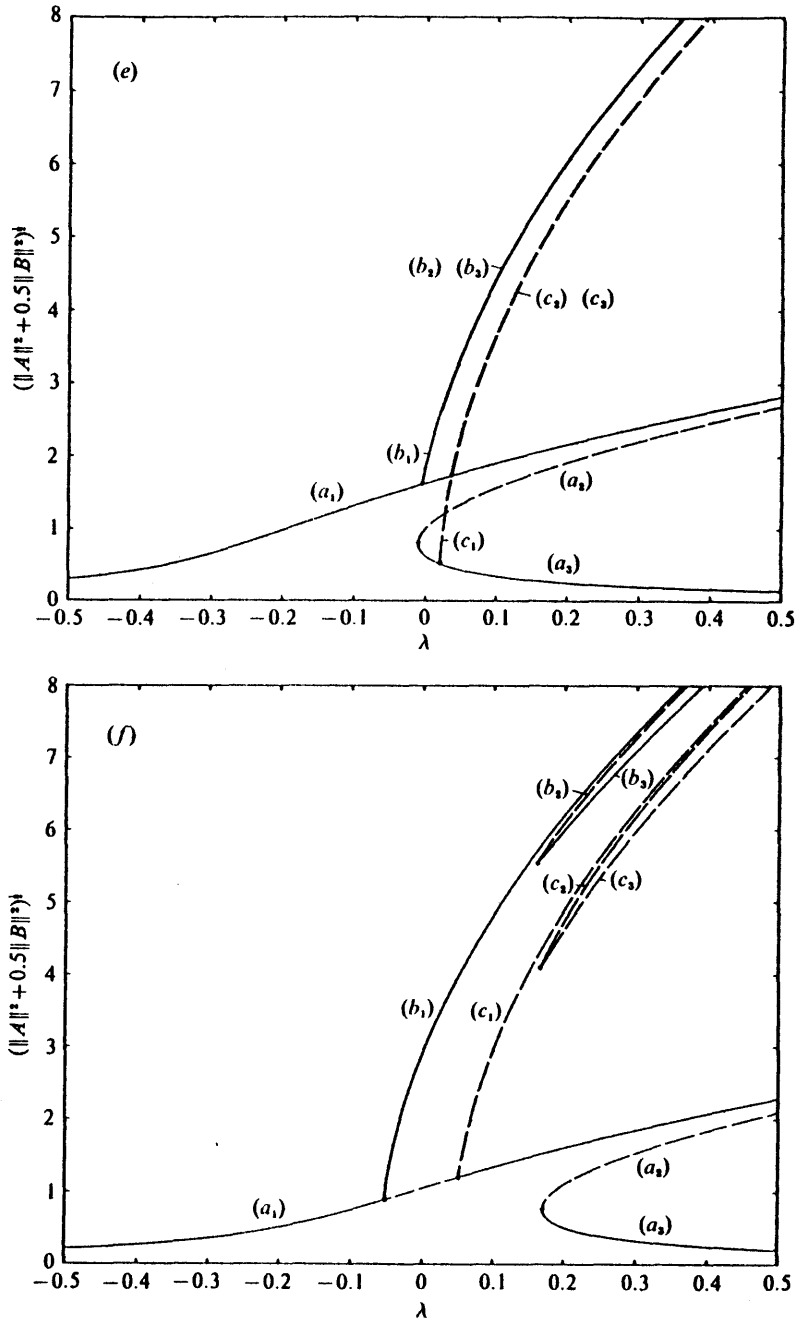

Figure 4. Codimension-one bifurcation diagrams of the stationary solution amplitude $(\| A \|^2 + 0.5\| B \|^2)^{1/2}$ versus the excitation detuning parameter λ for $n = 1$, $\ell = 0.248062$, $\varepsilon = 0.009072$ and $h =$ (a) 1.5; (b) 1.6; (c) 1.7; (d) 1.8; (e) 2.2; (f) 4.0. The solid and broken lines are respectively the stable and unstable solutions and the bifurcation points are marked by solid dots.

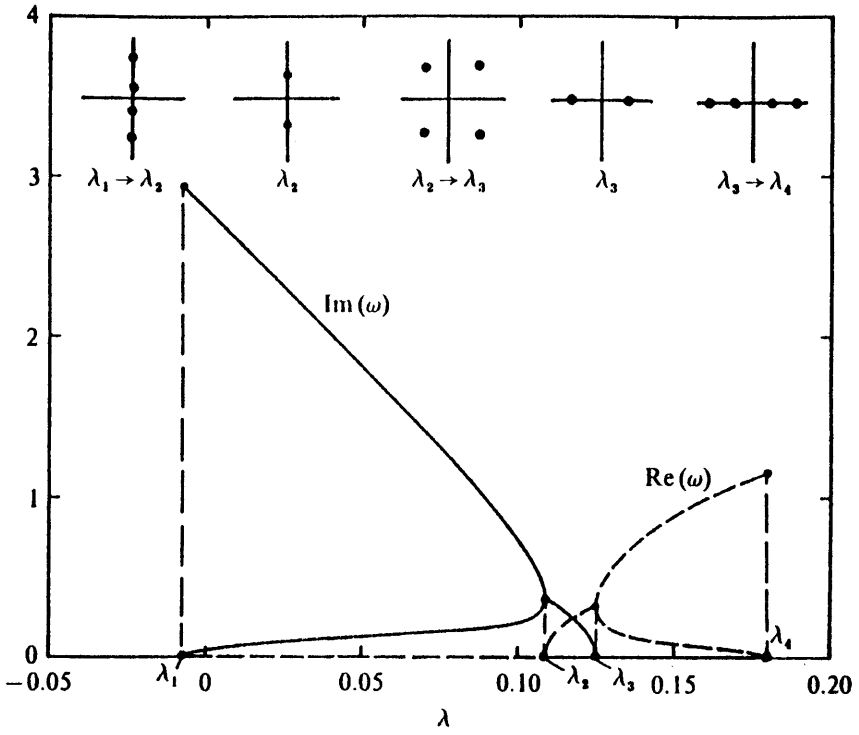

Figure 5. Variations of the real and imaginary parts of the eigenvalue ω along branch (b_3) in figure 4(b) for $h = 1.6$. Pitchfork bifurcation occurs at $\lambda = \lambda_1$ and Hamiltonian-Hopf bifurcation occurs at $\lambda = \lambda_2$.

axis. This kind of bifurcation at $\lambda = \lambda_2$ is known as Hamiltonian-Hopf bifurcation. It corresponds to the Benjamin-Feir instability (Benjamin & Feir 1967) for two-dimensional steady progressive waves (Zufiria 1988). Continuing along the branch (b_3), the two pairs of conjugate complex eigenvalues coalesce on the real ω axis at $\lambda = \lambda_3$, and then split into another two pairs of real eigenvalues along the real ω axis. It should be mentioned that at the bifurcation point $\lambda = \lambda_2$, where the three-dimensional wave becomes unstable, the amplitude of the transverse wave is not the maximum along the entire branch (b_3). The amplitude of the cross wave continues to increase until $\lambda = \lambda_3$ and then deceases to zero at $\lambda = \lambda_4$ where the family of three-dimensional waves ends. Branch (c_1) is another family of stable three-dimensional waves which bifurcates from the two-dimensional longitudinal wave family (a_1) in

the reverse direction of branch (b_3). Two inverse pitchfork bifurcations, branch (b_1) bifurcating from (a_1), and (c_3) from (a_3) are all unstable wave families.

Figures $4(c)$ and $4(d)$ are bifurcation diagrams for $h = 1.7$ and 1.9. Similar to the cases of $h = 1.5$ and 1.6, the stable three-dimensional family bifurcates from branch (a_3) and ends at branch (a_1). Hamiltonian-Hopf bifurcation occurs on the (b_3) branch where the three-dimensional wave becomes unstable. Unlike the case of $h = 1.5$ and 1.6, however, the branch (b_1) which bifurcates from the (a_1) longitudinal wave is stable for the present depths. All the families of the stationary solution (5.9c) are unstable.

For the deep water case $h = 4.0$ (figure $4f$), both three-dimensional wave families (5.9b) and (5.9c) bifurcate from the (a_1) branch of longitudinal waves. On the stable branch (b_1), both the longitudinal and transverse waves grow monotonically with increasing detuning parameter λ. The transverse wave grows faster than the longitudinal wave near the bifurcation, and then reaches the same growth rate as λ increases. The amplitude of the transverse wave finally increases to about 2.7 times that of the longitudinal wave. The other two solutions of (5.9b), one stable and one unstable branch, which are separated by a turning point, make up the family (b_2). On the stable branch, starting from the turning point, the amplitude of the longitudinal wave decreases while the amplitude of the transverse wave increases and dominates the three-dimensional wave motion. It is possible that some of the steady-state cross waves observed by Lin & Howard are on this stable wave family which is more visible physically than the first stable branch (b_1).

Bifurcation diagram figure $4(e)$ is the transition between the cases of intermediate depths (figures $4a-d$) and deep water (figure $4f$). The three branches of both the families (5.9b) and (5.9c) are indistinguishable in the figures. As in the case of $h = 4.0$, branch (b_1) of family (5.9b) bifurcates from branch (a_1) of the longitudinal wave. On the other hand, the three unstable branches (c_1, c_2, c_3) of family (5.9c) bifurcate from branches (a_1, a_2, a_3) respectively, similar to the case of $h = 1.8$.

Through a careful and difficult bifurcation analysis, it may, in principle, be

possible to identify regions of the frequency parameter in figures 4 for which more complex motions are likely to occur. In the present case, at least one stable solution exists for any value of λ and it is not immediately evident where chaotic solutions are most probable. From later Poincaré section plots (figures 12 for $\lambda = 0.1$ and figures 13 for $\lambda = 0.2$), chaotic motions appear to be more widespread near $\lambda = 0.2$ than $\lambda = 0.1$ corresponding to the somewhat more complex stationary solution picture near the higher frequency in figure 4(b). A more quantitative prediction based on bifurcation analyses may not be possible.

The comparison between the theoretical results and Lin & Howard's experimental data for the transverse stationary wave amplitude are shown in figures 6 for the cases of $L = 6$ in., $W = 24.1875$ in., $H = 24$ in., $\ell = 0.248062 \cong 1/4$, $2\theta = 0.279°$ (figure 6a), and $L = 12$ in., $W = 24.1875$ in., $H = 20$ in., $\ell = 0.496124 \cong 1/2$, $2\theta = 0.990°$ (figure 6b) respectively. For the $\ell \cong 1/4$ case, both longitudinal and transverse waves are first spatial harmonic modes, while for $\ell \cong 1/2$, the oscillation of the first mode transverse wave is associated with the second mode longitudinal wave. The solid and broken lines represent respectively the stable and unstable analytic results which consider the parametric resonance only (§4). The chain line is for the amplitude of the stable transverse wave response for which the interaction between resonant longitudinal and transverse waves is included. Similar to figures 2 but somewhat less satisfactory, the figures again show overpredictions of the theoretical response amplitude for both comparisons. One explanation for the discrepancy is the difficulty of separating the longitudinal and transverse wave components from the wave gauge measurements which was done graphically by Lin & Howard. The possible importance of dissipation again can not be ruled out.

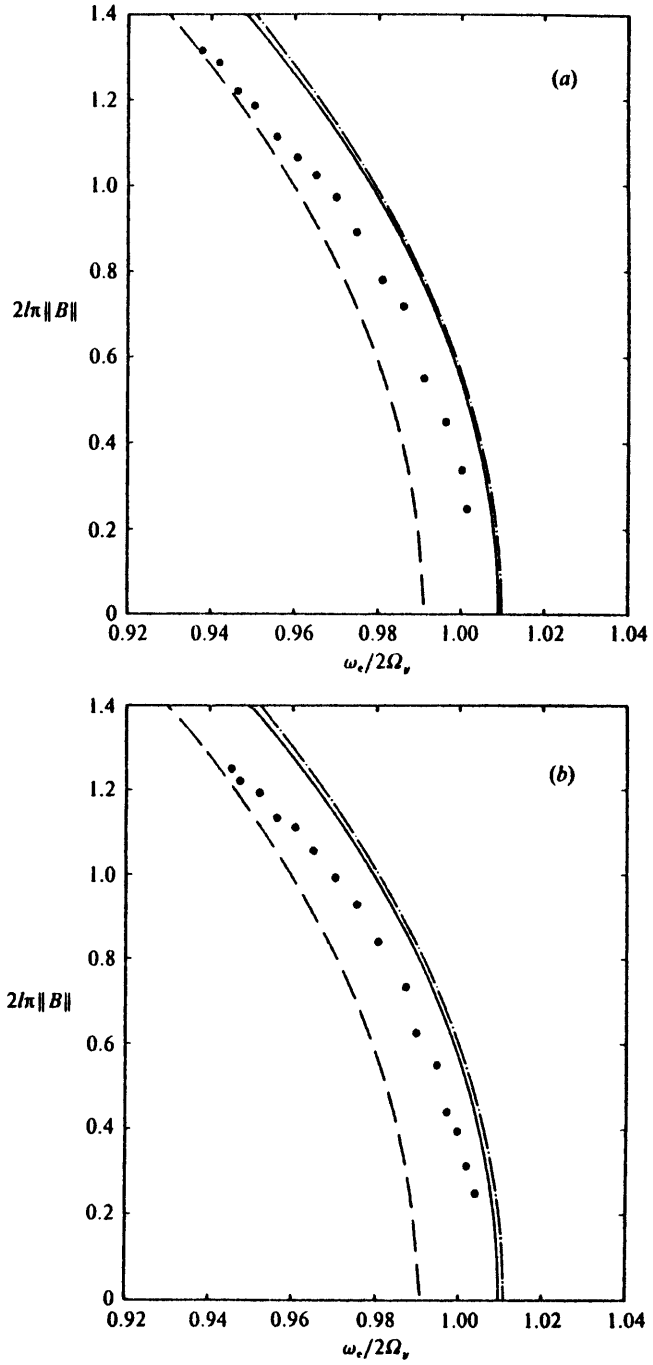

Figure 6. Comparisons of the frequency-response relationship for stationary transverse waves between the present analytic results and Lin & Howard's (1960) experimental measurements (circles) for (*a*) $L = 6$ in., $W = 24.1875$ in., $H = 24$ in., $2\theta = 0.279°$; and (*b*) $L = 12$ in., $W = 24.1875$ in., $H = 20$ in., $2\theta = 0.990°$. The solid and broken lines are stable and unstable stationary solutions of (4.4). The chain line is the stable cross-wave stationary solution (5.9*b*).

5.3. Regular and chaotic behavior

To obtain some understanding of the nonlinear evolutions, (5.5), or equivalently (5.8), are integrated numerically. A fourth-order Runge-Kutta time integration scheme with a typical time step $\Delta\tau = 0.005$ is used for the numerical simulations. For all the numerical results, the value of the Hamiltonian is conserved to nine decimal places. Depending on the parameters selected, and the initial conditions, the simulated temporal trajectories may exhibit either regular (periodic and quasi-periodic) or chaotic behavior.

Figures 7 and 8 show the temporal evolutions for the case of $h = 1.6$, $\lambda = 0.2$, $\ell = 0.248062$, $\varepsilon = 0.009072$, but with initial conditions $(C_a, D_a, C_b, D_b) = (0, -4.1373221, 0, 6)$ and $(0, -4.5269170, 4, 0)$ respectively. Both sets of initial conditions have the same Hamiltonian $\mathcal{H} = 9.0$. For the first set of initial conditions, the temporal evolutions in figure 7 are regular (quasi-periodic). Since the two time scales τ_1 and τ_2 are combined into the shorter scale τ_1, the transverse wave modulates over a longer time scale than the longitudinal wave. The interactions between the two are relatively weak. When the initial conditions are changed (figure 8), the resulting evolution becomes aperiodic and chaotic. The resonant interactions between the longitudinal and transverse waves are quite apparent.

For the chaotic evolution, two solutions with slightly different initial conditions in general depart from each other at an exponential rate, and the differences in the initial conditions are manifested at a later time by vastly different dynamical states. Such a characteristic of sensitivity to initial conditions can be quantified in terms of Lyapunov characteristic exponents which measure the mean rate of exponential separation of neighboring evolution trajectories. For numerical calculations, we adopt a renormalization scheme suggested by Beneltin, Galgani & Strelcyn (1976) to compute the maximum Lyapunov exponent. Figure 9 shows the variation of the maximum Lyapunov exponent σ for the parameter values and the different initial conditions of figures 7 and 8. For the regular evolution (figure 7), it is seen

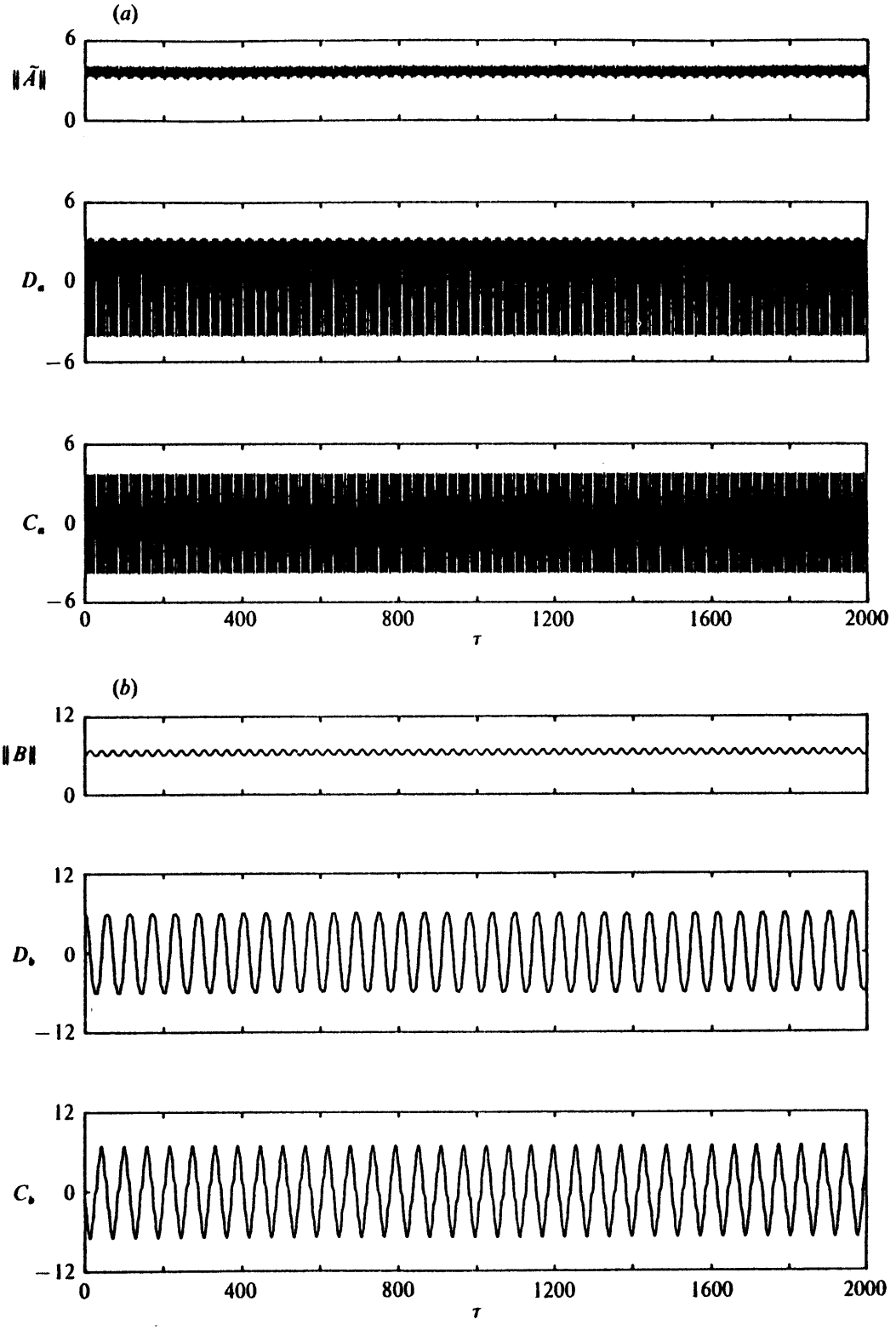

Figure 7. Time evolutions of (a) the longitudinal wave envelope, and (b) the transverse wave envelope for $h = 1.6$, $\lambda = 0.2$, $\ell = 0.248062$, $\varepsilon = 0.009072$ with the initial condition $(C_a, D_a, C_b, D_b) = (0, -4.137221, 0, 6)$.

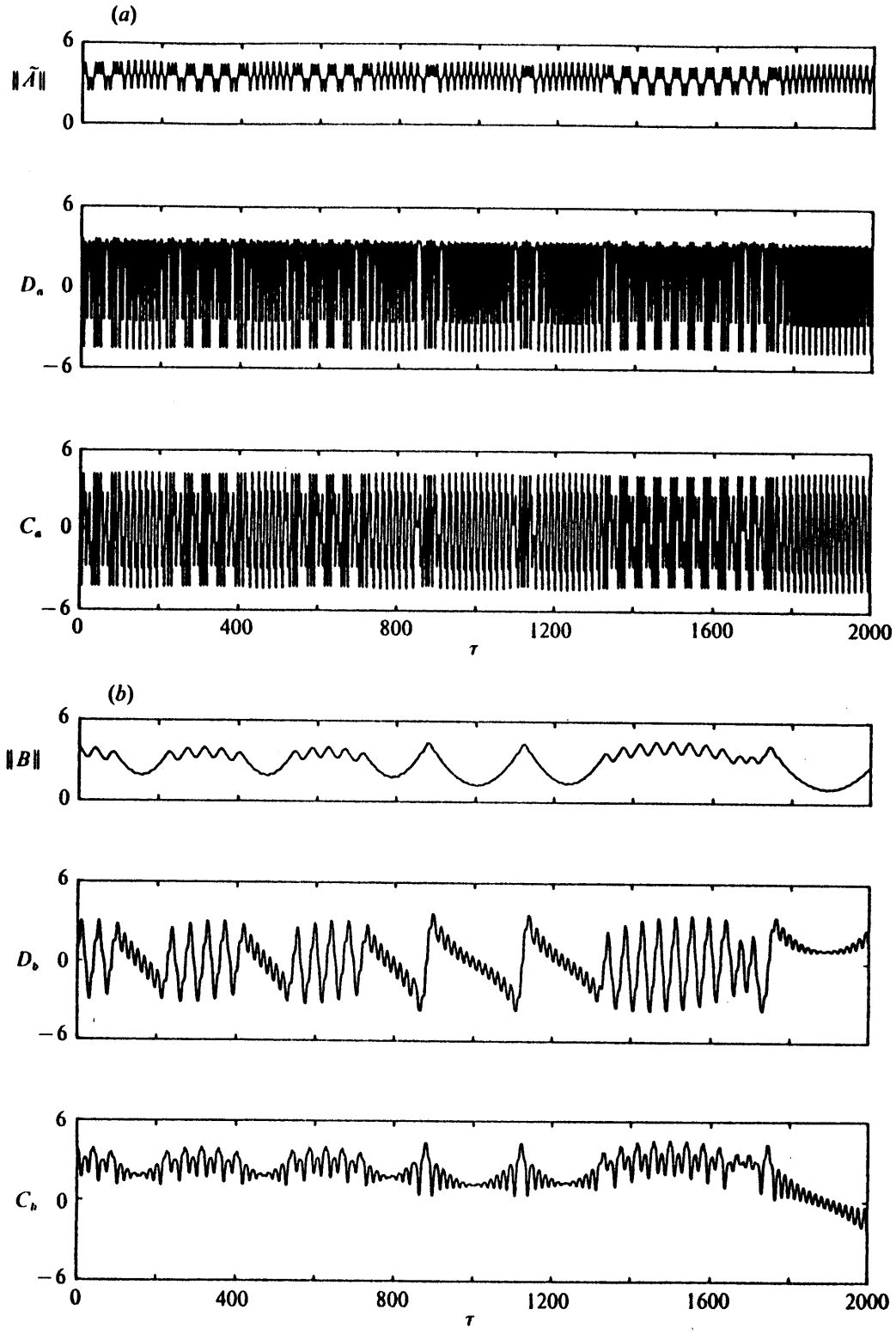

Figure 8. Time evolutions of (a) the longitudinal wave envelope, and (b) the transverse wave envelope for $h = 1.6$, $\lambda = 0.2$, $\ell = 0.248062$, $\varepsilon = 0.009072$ with the initial condition $(C_a, D_a, C_b, D_b) = (0, -4.526917, 4, 0)$.

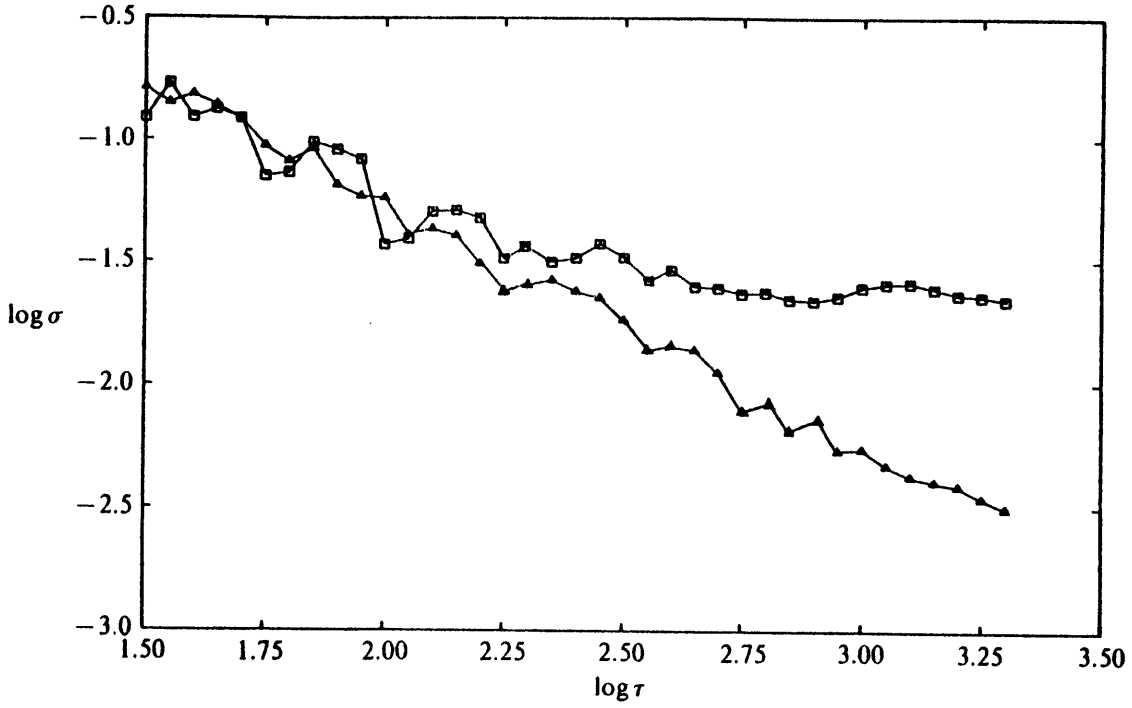

Figure 9. Variation of the maximum Lyapunov exponent σ with τ for the evolutions of figures 7 (triangles) and 8 (rectangles).

that σ (triangles) decreases and eventually vanishes in the limit of large τ. For the chaotic motion of figure 8, however, σ (rectangles) approaches a positive finite value measuring the exponential divergence of neighboring trajectories.

Another characterization for regular and chaotic behavior is the power spectrum of the evolution amplitude. From the numerical solution of the evolution over a time interval $N\Delta\tau$, the power spectrum of a time series amplitude $E(\tau_k)$ can be estimated using fast Fourier transform according to

$$P(f_n) = \frac{2\Delta\tau}{N}\left\|\sum_{k=0}^{N-1} E(\tau_k)w(\tau_k)\exp(\mathrm{i}2\pi\frac{kn}{N})\right\|^2, \qquad (5.14)$$

where $\tau_k = k\Delta\tau$ is the discrete time, $f_n = n/(N\Delta\tau)$ is the discrete frequency,

and $w(\tau_k) = (2/3)^{1/2}[1 - \cos(2\pi k/N)]$ is the Hamming window function employed. The power spectra P_a and P_b of the modulus $\|\tilde{A}\|$ and $\|B\|$ for two sets of initial conditions of figures 7 and 8 are shown in figures 10 and 11. For the regular evolution, the power spectrum (figures 10) consists of a finite series of discrete spikes which corresponds to multiharmonic motions in the quasi-periodic evolution. For the chaotic evolution (figure 11) the spectrum exhibits broad-band features characteristics of such motions.

To understand the global behavior of the Hamiltonian system in phase space, we construct the two-dimensional first return map on the hypersurface $\Sigma_{\mathcal{H}}$ of codimension-one. Such a hypersurface is known as a Poincaré surface of section which we choose for our problem to be defined by

$$\Sigma_{\mathcal{H}} = \left\{(C_a, D_a, C_b, D_b):\ C_a = 0,\ \frac{dC_a}{d\tau} > 0,\ \mathcal{H} = \mathcal{H}(C_a, C_b, D_a, D_b; \lambda, h, \ell, n)\right\}. \tag{5.15}$$

On the Poincaré section, a fixed point corresponds to a periodic trajectory, points lying on smooth curves (invariant curves) belong to a quasi-periodic orbit, while those belonging to a chaotic orbit will appear to fill a region.

Figures 12 show the Poincaré sections for the same geometric parameters as those for figures 7 and 8 but with λ=0.1 and for Hamiltonian values $\mathcal{H}$=2.0, 4.0 and 6.0 respectively. For the lowest energy level $\mathcal{H}$=2.0, the phase portrait figure 12(a) appears completely regular: an elliptic fixed point at the origin surrounded by a nested sequence of invariant curves. As the energy level increases, for example figure 12(b) for $\mathcal{H}$=4.0, a chaotic region is seen between the inner and outer regular phase space. When the energy level is further raised, the outermost energy surface shrinks in the phase space and regular motions become predominant again as shown in figure 12(c) for $\mathcal{H}$=6.0. We call this scenario the 'banded-energy' phenomenon since chaotic motions appear to be limited to an interval (or band) of energy values.

Completely different pictures emerge as one or more of the other physical parameters are altered. For illustration, we keep the same geometry and detuning value of $\lambda = 0.2$ as figures 7 and 8, and consider the Poincaré sections for energy

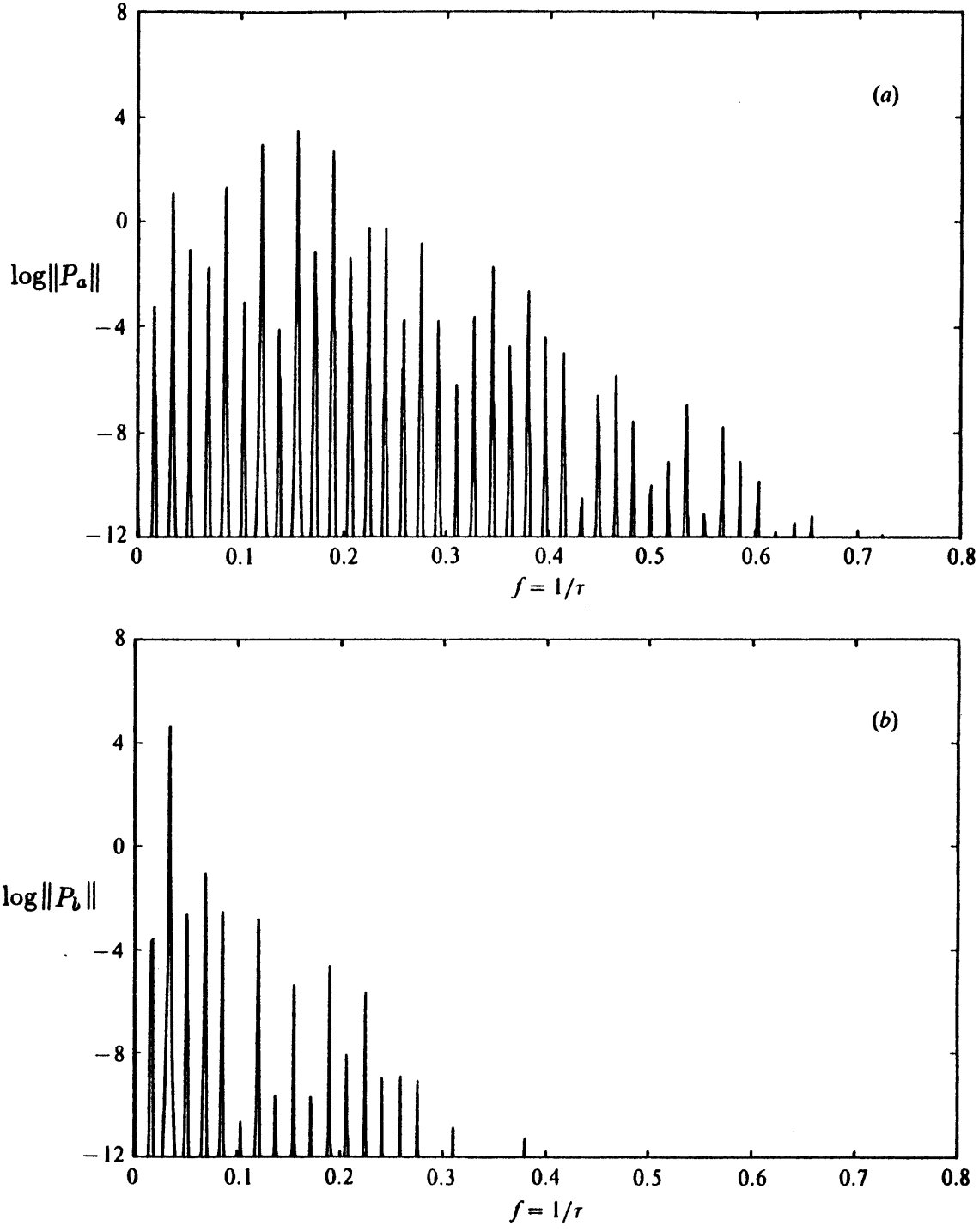

Figure 10. Power spectrum log $\| P_a \|$ and log $\| P_b \|$ of the evolution amplitudes (*a*) $\| \tilde{A} \|$; and (*b*) $\| B \|$ in figure 7.

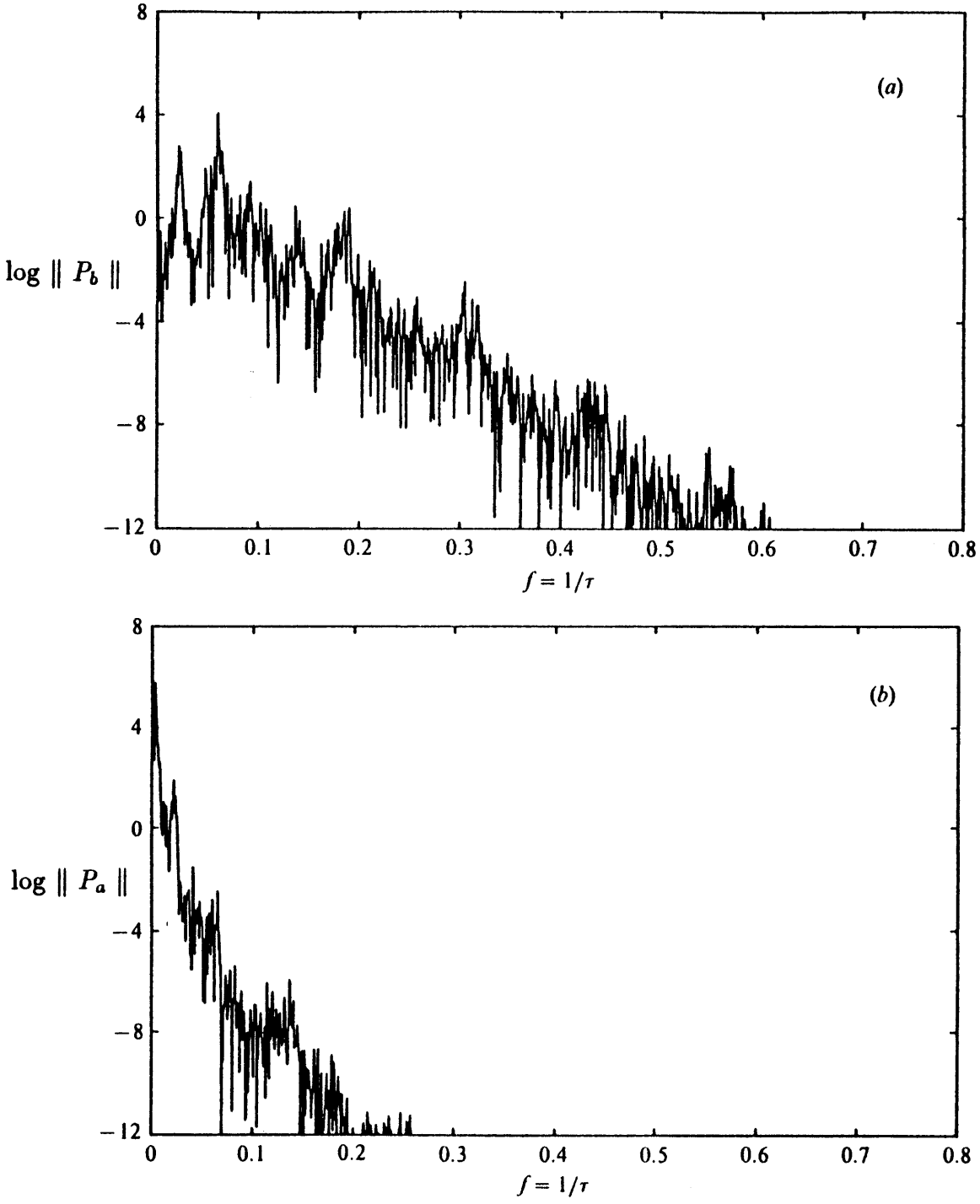

Figure 11. Power spectrum log || P_a || and log || P_b || of the evolution amplitudes (*a*) || $\tilde{A}$ ||; and (*b*) || B || in figure 8.

levels corresponding to $\mathcal{H} = 8.0$, 9.0, 10.0 and 11.968215 respectively. The fourth value of $\mathcal{H}$ is the Hamiltonian of the two-dimensional longitudinal stationary wave (branch a_1 in figure 4*a*) with a perturbation of $0.001(\delta D_{a0})$. The phase portraits in figure 13(*a*) for $\mathcal{H} = 8.0$ are completely regular. For somewhat higher energies, say $\mathcal{H} = 9.0$, we see that the elliptic fixed point at the origin loses its stability, becoming hyperbolic and gives rise to two elliptic fixed points (figure 13*b*). Note that the simulations of figures 7 and 8 correspond to this case and the resulting regular and chaotic evolutions starting from the two different initial conditions are evident from figure 13(*b*). As the energy level is further increased, a large chaotic zone occupies most of the energy surface while the region of regular orbits shrinks as shown in figure 13(*c*) for $\mathcal{H} = 10.0$. When $\mathcal{H}$ reaches close to its maximum value, for example for $\mathcal{H} = 11.968215$ in figure 13(*d*), the elliptic fixed point at the origin reappears and the outermost energy surface forms a shell-like shape occupied mostly by chaotic orbits surrounded by a small layer of regular orbits. We refer to this as the 'critical-energy' phenomenon because there seems to be a critical energy level beyond which chaotic orbits dominate the phase space.

As we have seen, the present nonlinear dynamical system possesses remarkably rich and varied solution features depending in subtle ways on the physical parameters, h, ℓ, n, λ and ε, the total energy, $\mathcal{H}$, as well as the specific initial phases of the motions. Given the large number of variables, a more global understanding of the problem, for example a criterion for the onset of widespread chaos, would be most useful.

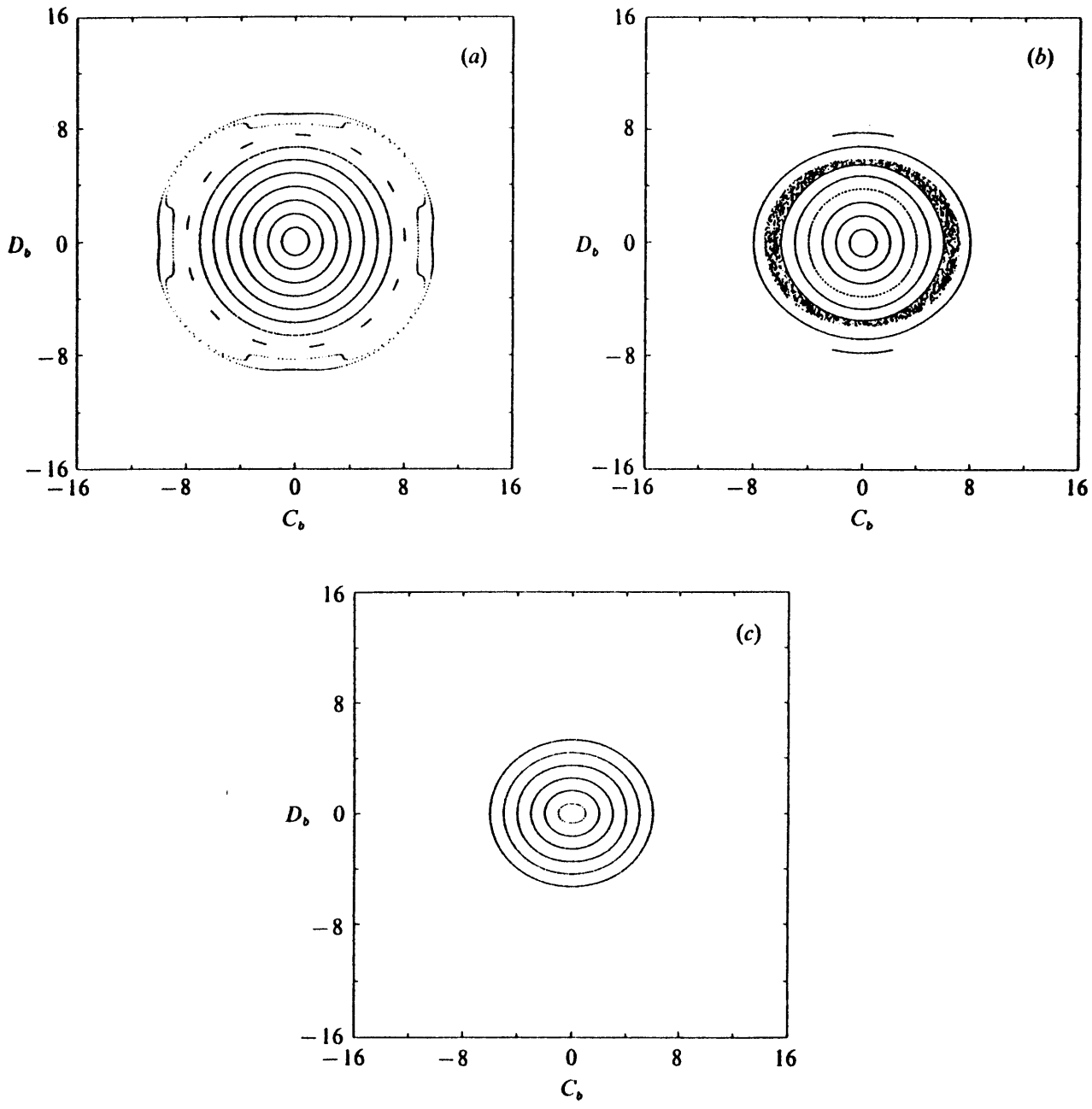

Figure 12. Poincaré sections for $h = 1.6$, $\lambda = 0.1$, $\ell = 0.248062$, $\varepsilon = 0.009072$ on energy surfaces corresponding to $\mathcal{H} =$ (a) 2.0; (b) 4.0; (c) 6.0.

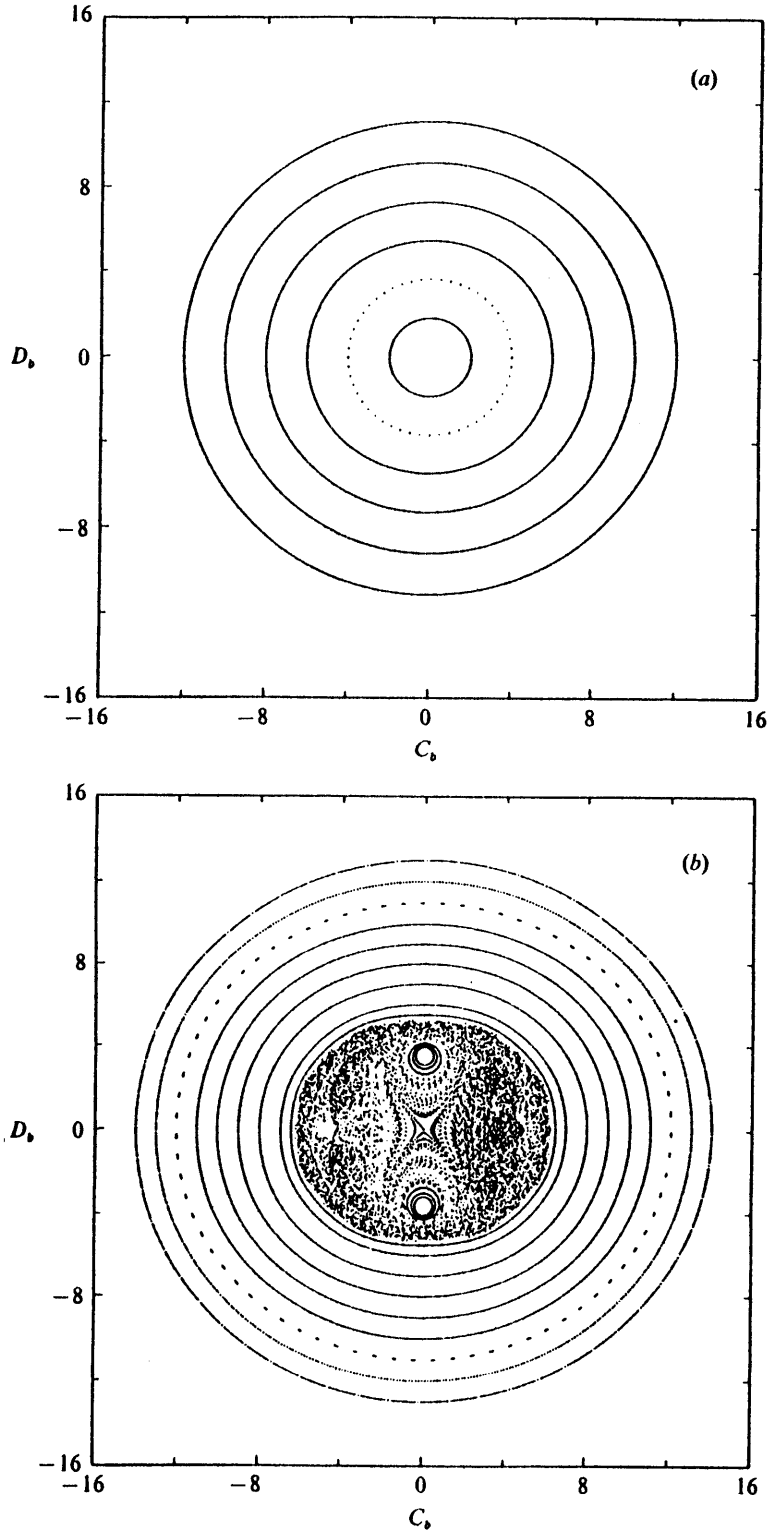

Figure 13(a, b). For caption see following page.

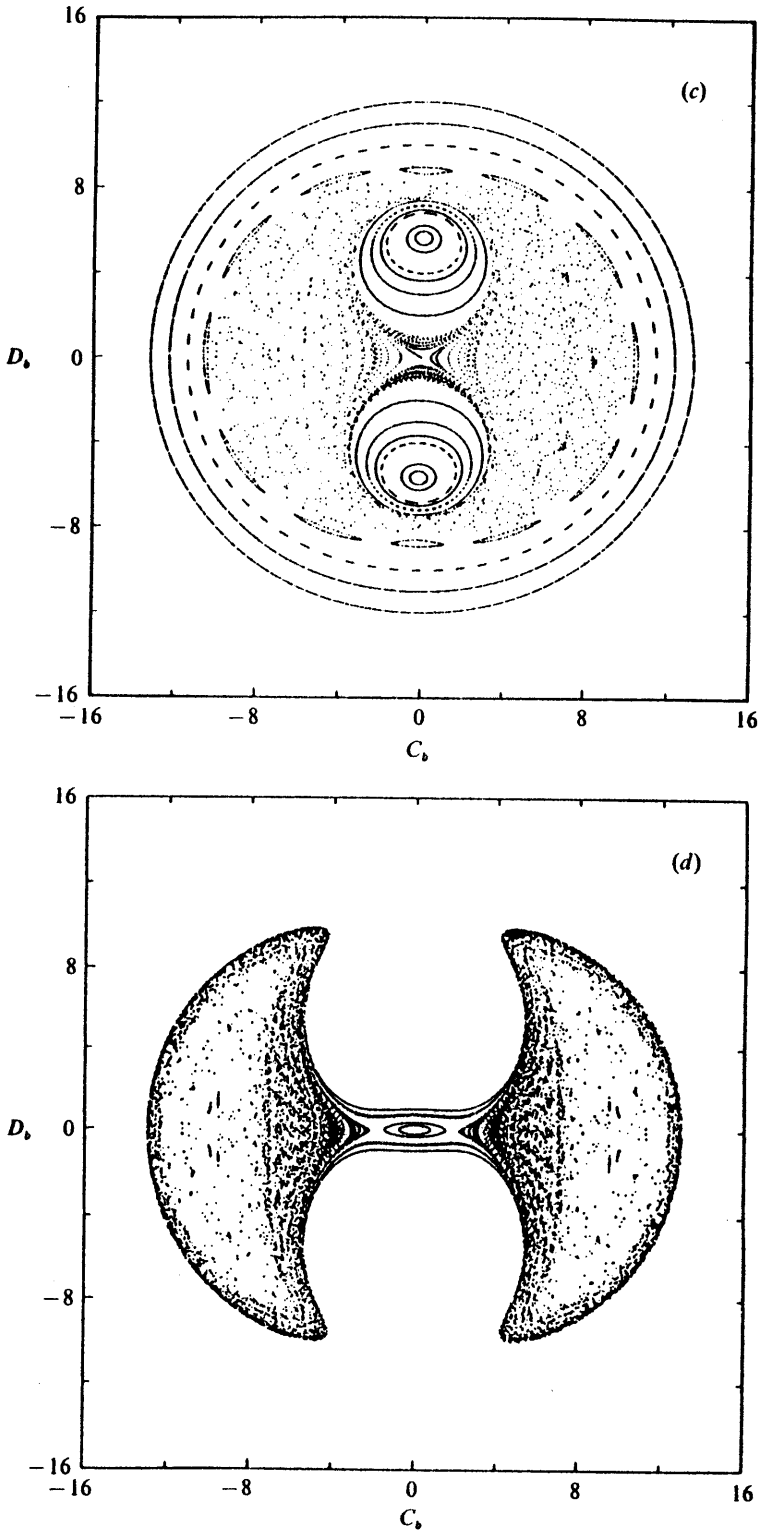

Figure 13. Poincaré sections for $h = 1.6$, $\lambda = 0.2$, $\ell = 0.248062$, $\varepsilon = 0.009072$ on energy surfaces corresponding to $\mathcal{H} = (a)$ 8,0; (b) 9.0; (c) 10.0; (d) 11.968215.

6. Resonance overlap criterion for the onset of widespread chaos

In the preceding chapter we characterize the dynamical features (regular and chaotic) of the Hamiltonian system (5.8) by the Lyapunov characteristic exponent and power spectrum of the evolutions. Both of these only identify and quantify the *local* nature of the dynamical system. The global behavior of the two degrees of freedom Hamiltonian system almost always exhibit a divided phase space: for some regimes the evolutions are regular and for others chaotic, as shown for example in figures 12 and 13. To explore the global dynamic behavior of the system directly in the large parameter space of h, ℓ, λ, ε, n and $\mathcal{H}$ plus the relative phases is clearly difficult if not prohibitive. It would be valuable to obtain an estimate in terms of the physical parameters the likelihood, say, of chaotic motions without resorting to detailed time-consuming numerical simulations in the entire phase and parameter space.

One approximate but effective technique for giving estimates of the onset of chaos for a large class of Hamiltonian systems is the method of resonance overlap due to Chirikov (see Chirikov 1979). The basic supposition of the method is that the destruction of tori and the appearance of widespread chaos can be attributed to the overlapping of the primary nonlinear resonances. According to the Kolmogorov-Arnol'd-Moser (KAM) theorem (Arnol'd 1978), for an integrable system, those invariant curves with sufficiently incommensurate winding numbers persist under small perturbations. As the strength of the perturbation increases, neighboring resonance zones will interact and chaotic motion is confined to a narrow regime around the separatrices bounding the resonance zones. As two resonance zones grow and eventually overlap, invariant curves between them will be destroyed, resulting in the onset of widespread chaos. The method of resonance overlap postulates that the last invariant curve between the two lowest-order resonances is destroyed when the sum of the half widths equals the distance between the reso-

nance centers. A major approximation is that the width of each resonance zone can be calculated independently of all the others. This simple criterion results in a conservative estimate, i.e. a sufficient condition, for the onset of widespread chaos because chaotic motion may result from interactions of the secondary resonances lying between the two primary resonances before the two primary resonance zones actually touch. Nevertheless the criterion yields a practical estimate for the critical parameters governing the transition to widespread chaos.

Applying the canonical transformation:

$$\tilde{A} = \mathrm{i}\sqrt{2I_a}\exp(\mathrm{i}\theta_a), \qquad B = \mathrm{i}\sqrt{2I_b}\exp(\mathrm{i}\theta_b),$$

where $I_{a,b}$ and $\theta_{a,b}$ are action and angle variables, the Hamiltonian (5.7) takes the new form:

$$\mathcal{H} = \mathcal{H}_0 + \mathcal{H}_a + \mathcal{H}_b, \tag{6.1a}$$

$$\mathcal{H}_0 = -\frac{1}{\mu}(-\gamma_a I_a - \gamma_b I_b + \tilde{\Gamma}_a {I_a}^2 + \tilde{\Gamma}_b {I_b}^2 + 2\tilde{\Sigma} I_a I_b), \tag{6.1b}$$

$$\mathcal{H}_a = -\frac{\tilde{\delta}}{\mu}\sqrt{2I_a}\cos\theta_a, \qquad \mathcal{H}_b = \frac{\tilde{\beta}}{\mu} I_b \cos 2\theta_b. \tag{6.1c,d}$$

The new form of the Hamiltonian consists of an integrable part $\mathcal{H}_0$ and two nonintegrable perturbations $\mathcal{H}_a$ and $\mathcal{H}_b$ responsible for the two primary resonances caused by the forced and parametric resonances respectively. The strategy is to calculate the resonance conditions and the widths of the resonance zones of $\mathcal{H}_A = \mathcal{H}_0 + \mathcal{H}_a$ and $\mathcal{H}_B = \mathcal{H}_0 + \mathcal{H}_b$ independently, and find the perturbation strength at which these two primary resonances touch. That the calculation can be done for each resonance in isolation is clearly a major approximation in the method of resonance overlap.

For a general Hamiltonian $\mathcal{H}(\underline{I}, \underline{\theta})$, where $\underline{I}$ and $\underline{\theta}$ are the vectors of action and angle variables, a resonance arises at those values of $\underline{I} = \underline{I}^r$ where the frequencies are commensurate. That is, there exists a vector $\underline{k}$ with irreducible integer components such that

$$\underline{k} \cdot \underline{\omega}^T(\underline{I}^r) = \underline{k} \cdot \left[\nabla_{\underline{I}} \mathcal{H}(\underline{I})\right]^T_{\underline{I}=\underline{I}^r} = 0, \tag{6.2}$$

where $\underline{k}$ is called the resonance vector. In general, for a Hamiltonian system of N degrees of freedom, each resonance vector defines an $(N-1)$-dimensional resonance surface in the N-dimensional action variables space. For the Hamiltonian $\mathcal{H}_A$, the resonance vector $\underline{k} = (1,0)$, which gives the resonance condition

$$2\tilde{\Gamma}_a I_a^r + 2\tilde{\Sigma} I_b^r - \gamma_a = 0. \tag{6.3}$$

Similarly for the Hamiltonian $\mathcal{H}_B$ with resonance vector $\underline{k} = (0,2)$, the resonance condition is

$$2\tilde{\Sigma} I_a^r + 2\tilde{\Gamma}_b I_b^r - \gamma_b = 0. \tag{6.4}$$

The next step is to transform the Hamiltonians $\mathcal{H}_A$ and $\mathcal{H}_B$ into canonical pendulum Hamiltonians. We proceed by introducing the generating function

$$F(\underline{J}, \underline{\theta}) = (\underline{I}^{r\,T} + \underline{J} \cdot \underline{\underline{\mu}}) \cdot \underline{\theta}^T, \tag{6.5}$$

where $\underline{J}$ is the new vector of action variables and $\underline{\underline{\mu}}$ is a constant matrix. The new angle variables are then given by

$$\underline{\psi}^T = \underline{\underline{\mu}} \cdot \underline{\theta}^T, \tag{6.6}$$

where the kth element is the resonant phase $\psi_k = \underline{k} \cdot \underline{\theta}^T$, and is slow relative to the other phases. Following Tabor (1981), we choose the constant matrix $\underline{\underline{\mu}}$ in such a way that $\psi_j = \theta_j$ for $j \neq k$. The new angle variables $\psi_j = \theta_j$, $j \neq k$ therefore are linearly independent and are fast relative to the resonant phase ψ_k. For the Hamiltonian $\mathcal{H}_A$, the transformation between the original and new action and angle variables are

$$\underline{I}^T = \begin{Bmatrix} I_a \\ I_b \end{Bmatrix} = \underline{I}^{r\,T} + \underline{J} \cdot \underline{\underline{\mu}}, \tag{6.7a}$$

and

$$\underline{\theta}^T = \begin{Bmatrix} \theta_a \\ \theta_b \end{Bmatrix} = \underline{\underline{\mu}}^{-1} \cdot \underline{\psi}^T. \tag{6.7b}$$

Transforming the Hamiltonian $\mathcal{H}_A$ to the new action and angle variables, averaging the Hamiltonian over the fast variables ψ_j, $j \neq k$, and expanding $\mathcal{H}_0(I_a, I_b)$ about the resonant actions $\underline{I} = \underline{I}^r = (I_a^r, I_b^r)$ yields

$$\overline{\mathcal{H}_A} \cong \mathcal{H}_0(I_a^r, I_b^r) - \frac{\tilde{\delta}}{\mu}\sqrt{2I_a^r}\cos\psi_a + \left[J_a\frac{\partial\mathcal{H}_0}{\partial I_a} + J_b\frac{\partial\mathcal{H}_0}{\partial I_b} + \frac{1}{2}{J_a}^2\frac{\partial^2\mathcal{H}_0}{\partial {I_a}^2} + J_aJ_b\frac{\partial^2\mathcal{H}_0}{\partial I_a\partial I_b} + \frac{1}{2}{J_b}^2\frac{\partial^2\mathcal{H}_0}{\partial {I_b}^2}\right]_{\underline{I}=(I_a^r, I_b^r)}. \quad (6.8)$$

Dropping the constant term $\mathcal{H}_0(I_a^r, I_b^r)$ and applying the resonance condition $\partial\mathcal{H}_0/\partial I_a = 0$, $\overline{\mathcal{H}_A}$ becomes

$$\overline{\mathcal{H}_A} \cong -\frac{\tilde{\Gamma}_a}{\mu}{J_a}^2 - \frac{\tilde{\delta}}{\mu}\sqrt{2I_a^r}\cos\psi_a + \left[J_b\frac{\partial\mathcal{H}_0}{\partial I_b} + J_aJ_b\frac{\partial^2\mathcal{H}_0}{\partial I_a\partial I_b} + \frac{1}{2}{J_b}^2\frac{\partial^2\mathcal{H}_0}{\partial {I_b}^2}\right]_{\underline{I}=(I_a^r, I_b^r)}. \quad (6.9)$$

The next approximation of the method of resonance overlap is to assume that the net contribution from the last three terms is small, and we finally obtain the pendulum form of the resonant Hamiltonian as

$$\overline{\mathcal{H}_A^r} = -\frac{\tilde{\Gamma}_a}{\mu}{J_a}^2 - \frac{\tilde{\delta}}{\mu}\sqrt{2I_a^r}\cos\psi_a. \quad (6.10)$$

The resonance half-width is then given by

$$\Delta J = \left(\frac{2\tilde{\delta}}{\tilde{\Gamma}_a}\right)^{1/2}(2I_a^r)^{1/4}. \quad (6.11)$$

From this we can obtain the vector of resonance widths in the original action variables as

$$\underline{\Delta I}^T = \begin{Bmatrix}\Delta I_a \\ \Delta I_b\end{Bmatrix} = \underline{k}^T \cdot \Delta J = \begin{Bmatrix}\left(2\tilde{\delta}/\tilde{\Gamma}_a\right)^{1/2}(2I_a^r)^{1/4} \\ 0\end{Bmatrix}. \quad (6.12)$$

Similarly, for the Hamiltonian $\mathcal{H}_B$, the corresponding canonical pendulum resonant Hamiltonian is

$$\overline{\mathcal{H}_B^r} = -\frac{8\tilde{\Gamma}_b}{\mu}{J_b}^2 - \frac{-\tilde{\beta}}{\mu}I_b^r\cos\psi_b, \quad (6.13)$$

and the resonance half-width is

$$\Delta J = \left(\frac{-\tilde{\beta}}{2\tilde{\Gamma}_b} I_b^r\right)^{1/2}, \tag{6.14}$$

which gives the width of resonance in the original action variable as

$$\underline{\Delta I}^T = \left\{ \begin{array}{c} 0 \\ (-2\tilde{\beta} I_b^r/\tilde{\Gamma}_b)^{1/2} \end{array} \right\}. \tag{6.15}$$

The above analysis can be applied graphically to determine the value of the Hamiltonian at which resonance overlap occurs and hence provide an estimate for the onset of widespread chaos. In figures 14 we plot in the space of the original action variables (I_a, I_b) the resonance conditions (6.3) and (6.4) (curves (a_1) and (b_1)), the boundaries of resonance zone (6.12) and (6.15) (curves (a_2) and (b_2)), and the curves of constant $\mathcal{H}_0$ for the cases of h=1.6, ℓ=0.248062, ε=0.009072 and λ=0.1, 0.15, 0.2, 0.3. Superposing the two resonance zones, we obtain the overlap region as shown by the shaded areas in the figures. The global behavior of the Poincaré sections in figures 12 and 13 can be completely explained in terms of these resonance overlap diagrams.

From figure 14(a) for $\lambda = 0.1$, we see that the level curve of $\mathcal{H}_0 \cong \mathcal{H} = 2.0$ does not intersect the resonance overlap zone. This suggests that isolated resonance zones dominate at this low energy and we should see only regular motions as figure 12(a) shows. As $\mathcal{H}_0$ is increased, part of the level curves sweep across the interior of the resonance overlap regime, indicating the onset of chaotic motion. Figure 12(b) shows the Poincaré section of such an energy level, $\mathcal{H}$=4.0, where a chaotic region is seen between the inner and outer regular phase portraits. As the energy level is further raised, the level curves no longer intersect the overlap region and regular motions become predominant again in the phase space as shown in figure 12(c) for $\mathcal{H}$=6.0. This explains the so called banded-energy phenomenon.

The critical-energy phenomenon for $\lambda = 0.2$ with the energy levels of $\mathcal{H}_0 \cong \mathcal{H} =$ 8.0, 9.0, 10.0 and 11.968215 as presented in figures 13 can also be predicted according to the resonance overlap diagram figure 14(c). That the phase portraits in figure

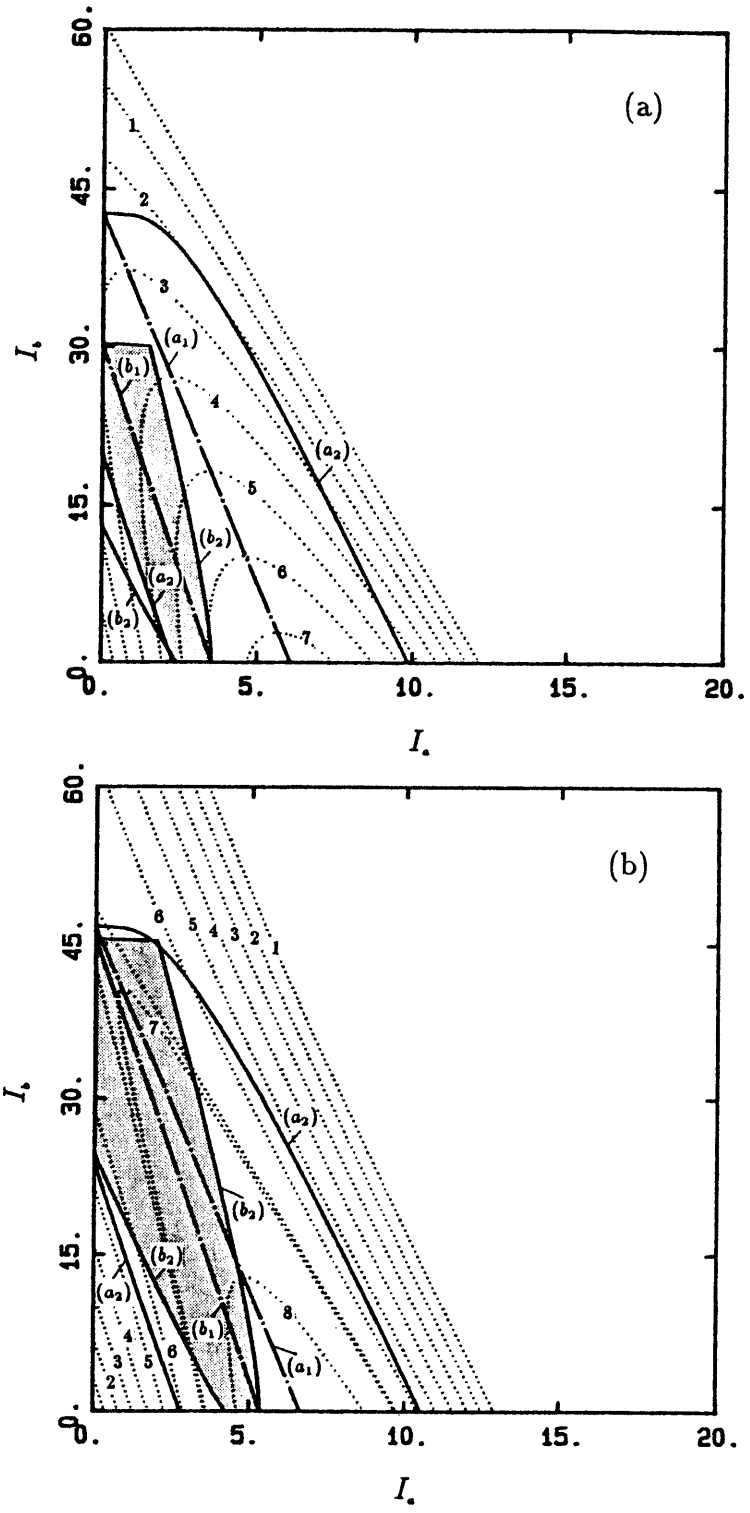

Figure 14(a, b). For caption see following page.

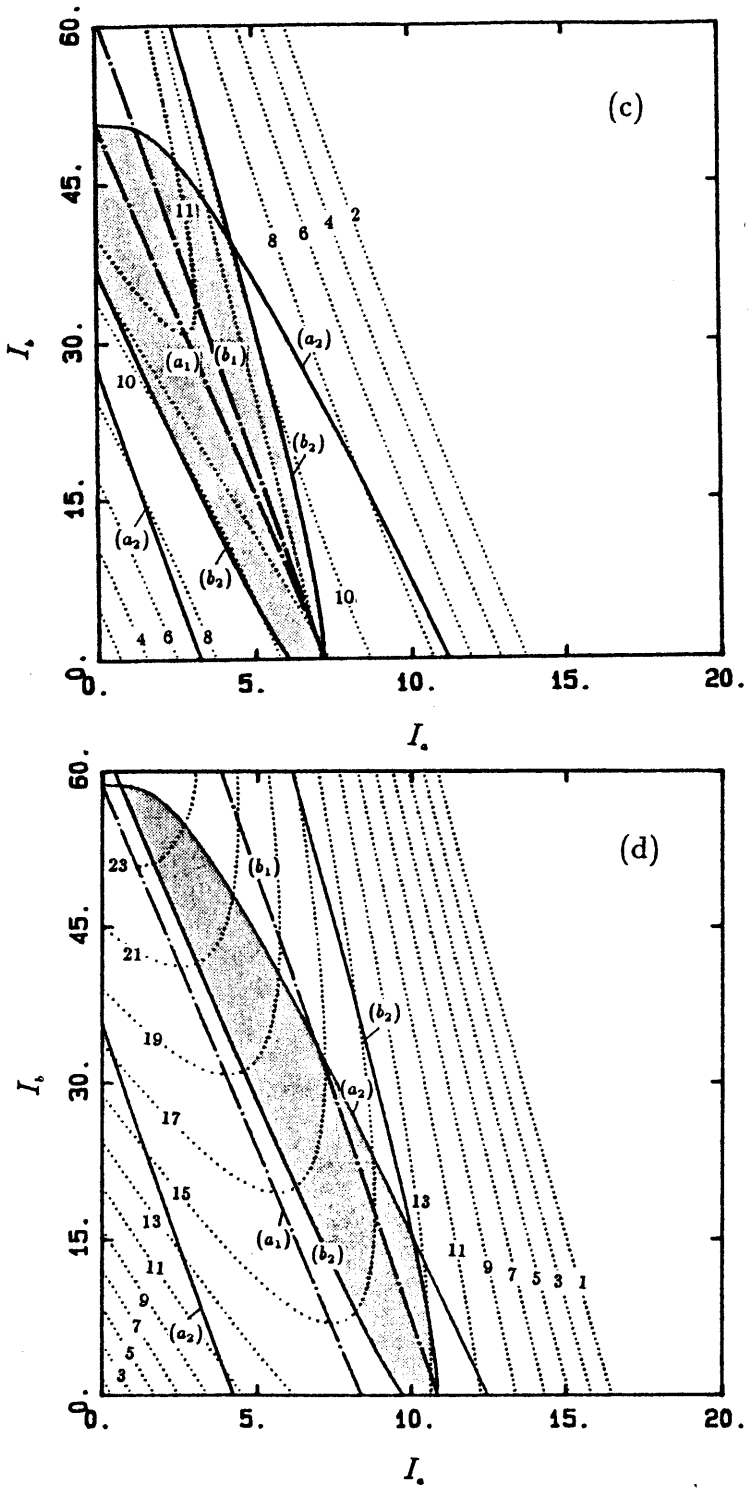

Figure 14. Resonance overlap diagrams for $h = 1.6$, $\ell = 0.248062$, $\varepsilon = 0.009072$ with different values of $\lambda =$ (a) 0.1; (b) 0.15; (c) 0.2; (d) 0.3. The chain lines (a_1) and (b_1) are resonance conditions for $\mathcal{H}_A$ and $\mathcal{H}_B$, and the thick solid lines (a_2) and (b_2) denote resonance boundaries of $\mathcal{H}_A$ and $\mathcal{H}_B$ respectively. The shaded area is the overlap region of the two resonances. The dotted lines are level cures of constant $\mathcal{H}_0$.

13(a) are completely regular can be seen from figure 14(c) where the level curve of $\mathcal{H}_0 \cong \mathcal{H} = 8.0$ is away from the overlap zone. As the energy level is raised beyond a critical value the level curves never leave the overlap region once they are inside. This corresponds to the critical-energy phenomenon we have seen in the numerical experiments. The phase space will be dominated by chaotic trajectories as indicated in figures 13($b - d$) for energy levels greater than the critical value.

Since the physical parameters are related in a very complicated way to the coefficients in the Hamiltonian system, the resonance overlap diagrams suggest an effective way to search the space of the parameters. One important information of the resonance overlap diagram is the area of the overlap zone which gives a measure of the degree or likelihood of chaotic motions for the specific set of physical parameters. Thus we simply plot the areas of the overlap zone as a function of the changing parameters. As an illustration, we show the variation of the overlap area with the excitation frequency detuning parameter λ for ℓ=0.248062, ε=0.009072 and three different depths h=1.6, 1.8 and 2.2 in figure 15. For h=2.2, the overlap area increases monotonically with increasing detuning λ. For the intermediate depths, h=1.6 and 1.8, however, the overlap areas increase to a maximum and then fall off as λ is further increased. The effect of the excitation amplitude ε on the degree of chaos can likewise be examined. Figure 16 shows the change of overlap area with ε for the cases ℓ=0.248062, h=1.6 and λ=0.1, 0.15, 0.2 and 0.3. Surprisingly, the overlap area increases rapidly first for increasing excitation amplitude and then decreases for larger amplitudes so that the most widespread chaotic responses need not be associated with the largest driving amplitudes.

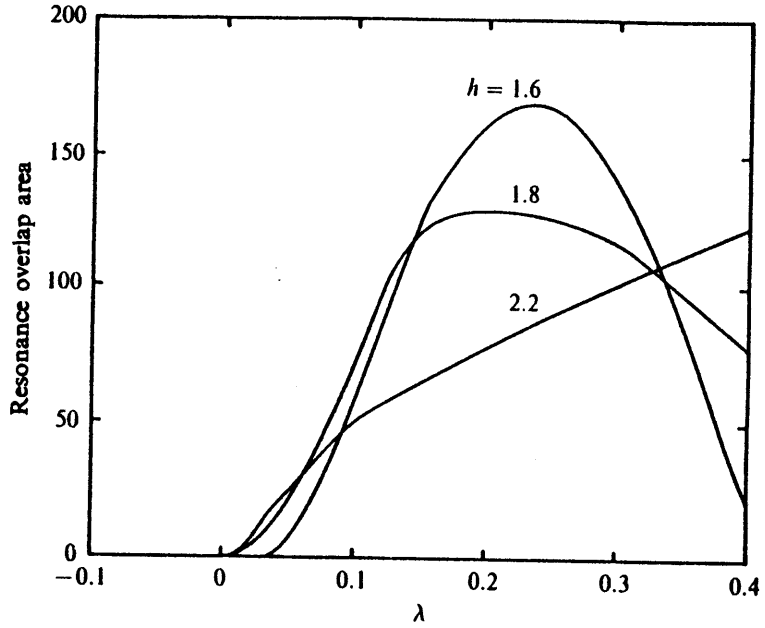

Figure 15. Resonance overlap area versus detuning parameter λ for $\ell = 0.248062$, $\epsilon = 0.009072$ and different values of $h = 1.6$, 1.8 and 2.2.

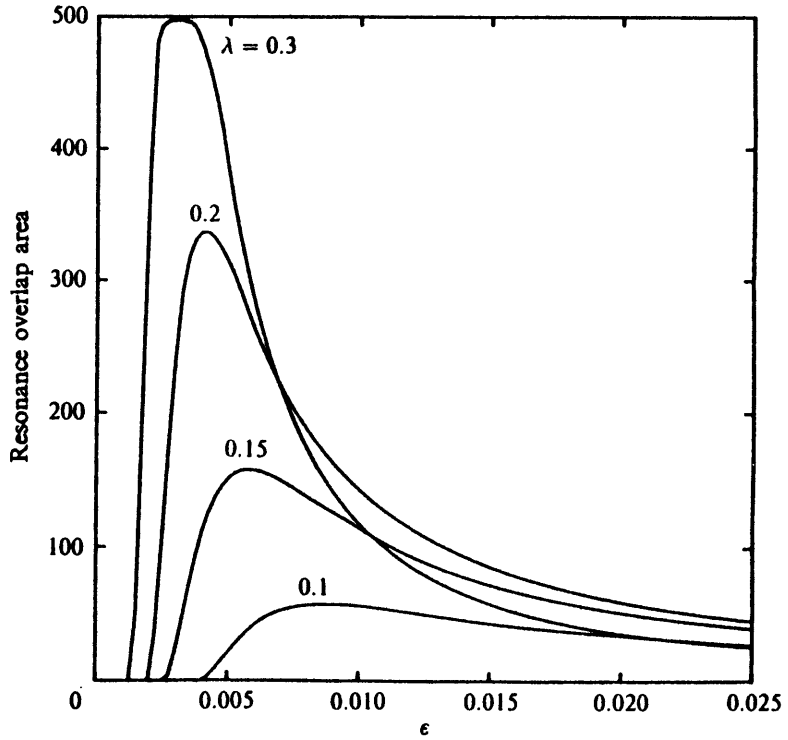

Figure 16. Resonance overlap area versus excitation amplitude ϵ for $\ell = 0.248062$, $h = 1.6$ and different values of $\lambda = 0.1$, 0.15, 0.2 and 0.3.

7. Concluding remarks

In recent years, the generic two-degree-of-freedom internally resonant system of weakly nonlinear gravity waves in a (rectangular or circular) cylinder subject to either horizontal (directly forced) or vertical (parametrically resonant) excitation has been widely studied primarily for the weakly dissipative system. These include, for example, Keolian *et al.* (1981), Gollub & Meyer (1983), Ciliberto & Gollub (1984, 1985*a,b*), Meron & Procaccia (1986*a,b*, 1987), Nayfeh (1987), Umeki & Kambe (1989) for the vertically oscillated circular cylinder; Gu & Sethna (1987), Feng & Sethna (1989), Simonelli & Gollub (1989) for the vertically oscillated square cylinder; and Miles (1984*b*), Funakoshi & Inoue (1987, 1988) for the horizontally oscillated circular cylinder. As pointed out earlier, the present cases I and II differ mainly in detail and in providing direct comparisons to the measurements of Lin & Howard (1960). The dynamic system of case III, however, is new and differs from the above problems in the incorporation of both direct and parametric excitations simultaneously.

We have not considered dissipation in this work although it is known that such effects play a role in the physical problem (e.g. Shemer & Kit 1988). For numerical studies, a small phenomenological linear damping term can be readily included in the dynamical system (e.g. Miles 1984*b*). At present, studies of the onset of chaos in dissipative dynamical systems are yet in an infant stage and much of the work to predict global properties still relies on numerical simulations. Although the method of resonance overlap is strictly applicable only to conservative systems, it is a useful analysis tool for some weakly dissipative problems by providing a global prediction to the corresponding Hamiltonian system with the dissipation terms neglected. Some of our preliminary simulation results indicate that for weakly dissipative systems, Hamiltonian chaos is preserved. Given the uncertainty of the actual phenomenological damping to use, the sensitive dependence of the resulting evolutions on the damping, and the lack of mature methodologies for analyzing dissipative

dynamical systems, it is hoped that the present study of the conservative system would facilitate the understanding of the physical problem and provide an analytic basis for examining the global behaviors. Clearly, much further work remains for the study of dissipative systems.

Appendix A. Treatment of the inhomogeneous wavemaker boundary conditions

We expand the shape function $F(z) = 1+z/h$ in the inhomogeneous wavemaker boundary condition (3.2) in terms of a Fourier series:

$$F(z) = -\frac{2}{\pi}\sum_{m=0}^{\infty}\left[\frac{\sin\frac{(2m+1)}{2h}z}{(2m+1)}\right] - \frac{4}{\pi^2}\sum_{m=0}^{\infty}\left[\frac{\cos\frac{(2m+1)}{h}(z+h)}{(2m+1)^2}\right]. \qquad (A.1)$$

The potential $\varphi(x,z)$ in (3.3) which satisfies the Laplace equation, homogeneous boundary conditions on the walls and the bottom, and $\partial\varphi/\partial x = F(z)$ at $x = 0$ can then be written as

$$\varphi(x,z) = \frac{4h}{\pi^2}\sum_{m=0}^{\infty}\left[\frac{\sin\frac{(2m+1)\pi}{2h}z\ \cosh\frac{(2m+1)\pi}{2h}(x-1)}{(2m+1)^2\sinh\frac{2m+1)\pi}{2h}}\right]$$
$$+\frac{4h}{\pi^3}\sum_{m=0}^{\infty}\left[\frac{\cos\frac{(2m+1)\pi}{h}(z+h)\ \cosh\frac{(2m+1)\pi}{h}(x-1)}{(2m+1)^3\sinh\frac{(2m+1)\pi}{h}}\right]. \qquad (A.2)$$

Expanding the hyperbolic cosine terms in (A.2) into Fourier cosine series and after some manipulation we obtain the expression (3.3*b*) for $\varphi(x,z)$. The terms which appear in the free-surface boundary conditions (2.4c) and (2.5c) are φ and its first and second z derivatives evaluated at $z = 0$. These can be further simplified from (3.3*b*) as

$$\varphi(x,0) = -\frac{h^2}{24} - \frac{1}{\pi^2}\sum_{n=1}^{\infty}\frac{1}{n^2}\left(1 - \frac{2}{n\pi h}\tanh\frac{n\pi h}{2}\right)\cos n\pi x, \qquad (A.3a)$$

$$\left.\frac{\partial\varphi}{\partial z}(x,z)\right|_{z=0} = \frac{h}{2} + \frac{1}{\pi}\sum_{n=1}^{\infty}\frac{1}{n}\tanh n\pi h\ \cos n\pi x, \qquad (A.3b)$$

$$\left.\frac{\partial^2\varphi}{\partial z^2}(x,z)\right|_{z=0} = 1 + \frac{2}{\pi h}\sum_{n=1}^{\infty}\frac{1}{n}\tanh\frac{n\pi h}{2}\ \cos n\pi x, \qquad (A.3c)$$

where the results involving generalized functions (Oberhettinger 1973) are used in the summation of the Fourier series for the second derivative (A.3c). The constant terms in (A.3) correspond to f_0, f_0' and f_0'' in the expression of β in (4.5*a*), and the coefficients of $\cos n\pi x$ are designated as f_n, f_n' and f_n'' respectively.

For the inhomogeneous wavemaker boundary condition (4.2), we write

$$\frac{\partial \Phi_3}{\partial x} = (B^* e^{-it} + B e^{-i3t} + \text{c.c.}) \cos \ell\pi y \; G(z), \tag{A.4a}$$

where

$$G(z) = \frac{\sinh \ell\pi(z+h)}{4h \sinh \ell\pi h}. \tag{A.4b}$$

Again, we expand $G(z)$ into a Fourier series and after some manipulation obtain the expression (4.3*b*) for $\theta(x,z)$ which satisfies the Laplace equation, and the inhomogeneous boundary condition (A.4*a*). The contributions $\theta(x,0)$ and $\partial\theta/\partial z \mid_{z=0}$ can be further simplified and expressed as

$$\theta(x,0) = g_0 + \sum_{n=1}^{\infty} g_n \cos n\pi x, \tag{A.5a}$$

$$\left.\frac{\partial \theta}{\partial z}(x,z)\right|_{z=0} = g_0' + \sum_{n=1}^{\infty} g_n' \cos n\pi x, \tag{A.5b}$$

where g_0 and g_0' are given by (4.5*f*, *g*).

Appendix B. Two-dimensional Faraday problem for stratified two-layer flow

We consider the resonant motion of a stratified two-layer fluid in a two-dimensional rectangular basin subject to a vertical oscillation $-a_e \cos\omega_e t$. The densities of the lower and upper fluids are ρ' and ρ'' respectively, with the lower layer heavier than the upper layer ($\rho' > \rho''$). For convenience, in what follows, all physical variables are non-dimensionalized by the half length of the basin L, and the timescale $2/\omega_e$. A coordinate system fixed with the basin is chosen so that the origin and x-axis are in the undisturbed interface, z is positive upwards, the side walls of the basin are at $x = \pm 1$, and the lower bottom and the upper lid are at $z = -h'$ and $z = h''$ respectively. For ideal, incompressible and irrotational fluids, the velocity potentials of lower and upper flows, $\Phi'(x,z,t)$ and $\Phi''(x,z,t)$, satisfy the Laplace equations with the solid boundary conditions on the side walls, bottom and lid. The kinematic boundary conditions on the interface $z = \zeta(x,t)$ are

$$\frac{\partial\zeta}{\partial t} + \frac{\partial\zeta}{\partial x}\frac{\partial\Phi'}{\partial x} - \frac{\partial\Phi'}{\partial z} = 0, \tag{B.1a}$$

$$\frac{\partial\zeta}{\partial t} + \frac{\partial\zeta}{\partial x}\frac{\partial\Phi''}{\partial x} - \frac{\partial\Phi''}{\partial z} = 0, \tag{B.1b}$$

and the dynamic boundary condition is

$$\left\{\frac{\partial\Phi'}{\partial t} + \frac{1}{2}\nabla\Phi'\cdot\nabla\Phi' + 4(N^2\mu + \varepsilon\cos 2t)\zeta\right\}$$
$$= \rho\left\{\frac{\partial\Phi''}{\partial t} + \frac{1}{2}\nabla\Phi''\cdot\nabla\Phi'' + 4(N^2\mu + \varepsilon\cos 2t)\zeta\right\}, \tag{B.2}$$

where the density ration $\rho = \rho''/\rho' < 1$, the nondimensional amplitude of excitation $\varepsilon = a_e/L \ll O(1)$, $\mu = (\mu' + \rho\mu'')/(1-\rho)$, $\mu' = (m\pi\tanh m\pi h')^{-1}$, and $\mu'' = (m\pi\tanh m\pi h'')^{-1}$. We consider here the 1/2-subharmonic resonance of the mth-mode standing wave, so that $N = \Omega/\omega_e = 1/2 + \lambda\varepsilon$, where $\Omega = (g/(L\mu))^{1/2}$ is the dimensional natural frequency of the mth-mode internal standing wave, and λ is the detuning parameter.

Multiple-scale analysis of the boundary value problem is processed with the same long timescale τ and the same asymptotic expansions of Φ', Φ'' and ζ as for the cross-wave case (§4). At the leading order, $O(\varepsilon^{1/2})$, the velocity potentials Φ'_1 and Φ''_1 are

$$\Phi'_1 = \frac{1}{2}[B(\tau)e^{-\mathrm{i}t} + \text{c.c.}]\ \cos kx\ \frac{\cosh k(z+h')}{k\sinh kh'}, \tag{B.3a}$$

$$\Phi''_1 = -\frac{1}{2}[B(\tau)e^{-\mathrm{i}t} + \text{c.c.}]\ \cos kx\ \frac{\cosh k(z-h'')}{k\sinh m\pi h''}, \tag{B.3b}$$

where $k = m\pi$. The solvability condition at the third order ($O(\varepsilon^{2/3})$) yields the evolution equation for $B(\tau)$ as

$$\mu\frac{\mathrm{d}B}{\mathrm{d}\tau} + \mathrm{i}2\mu\lambda\, B - \mathrm{i}\beta B^{\star} - \mathrm{i}\Gamma\, B^2B^{\star} = 0, \tag{B.4}$$

where

$$\beta = 1, \qquad \Gamma = \frac{1}{1-\rho}(\Gamma' - \rho\Gamma'') \tag{B.5a,b}$$

$$\Gamma' = -\frac{p'_2}{8}(k^2\mu'^2 + k^2\mu\mu' - \frac{\mu}{\mu'} - 1) - \frac{p_2}{4}(k^2\mu\mu' - 1) + \frac{q_2}{4}(k^2\mu\mu' + 1) + \frac{k^2}{64}(\mu' - \mu), \tag{B.5c}$$

$$\Gamma'' = \frac{p''_2}{8}(k^2\mu''^2 - k^2\mu\mu'' + \frac{\mu}{\mu''} - 1) + \frac{p_2}{4}(k^2\mu\mu'' + 1) - \frac{q_2}{4}(k^2\mu\mu'' - 1) - \frac{k^2}{64}(\mu'' + \mu), \tag{B.5d}$$

$$p_2 = \frac{3k^4\mu'\mu''(\rho\mu''^2 - \mu'^2) + k^2(1-\rho)\mu'\mu''}{16(\rho\mu' + \mu'')}, \tag{B.5e}$$

$$q_2 = -\frac{k^2(\rho\mu''^2 - \mu'^2) + (\rho - 1)}{8(\rho\mu'' + \mu')}, \tag{B.5f}$$

$$p'_2 = -\frac{3k^4\mu'\mu''(\rho\mu''^2 - \mu'^2) + k^2\mu'[(3-\rho)\mu'' + 2\rho\mu']}{8(\mu'' + \rho\mu')}, \tag{B.5g}$$

$$p''_2 = \frac{3k^4\mu'\mu''(\rho\mu''^2 - \mu'^2) + k^2\mu''[(1-3\rho)\mu' - 2\mu'']}{8(\mu'' + \rho\mu')}. \tag{B.5h}$$

The evolution equation (B.4) has the same form as that of the cross wave, equation (4.4) in §4, or oscillations of a pendulum under parametric excitation (Struble 1963). The limiting case, $\rho = 0$, of (B.4) corresponds to the equation of free surface Faraday wave as in Ockendon & Ockendon (1973) and Miles (1984*a*). The stationary solutions and the linear stability analyses of (B.4) have been given in Ockendon & Ockendon (1973) and Miles (1984*a*). For the sake of later discussions, the phase-plane trajectories $B(\tau) = C(\tau) + \mathrm{i}D(\tau)$ for $\rho = 0$, $h' = \infty$, $\Gamma = \pi/8$ and $\mu\lambda = -1$, 0, 1 respectively are shown in figures 17$(a-c)$. Note that $\mu\lambda = \beta/2$ and $-\beta/2$ correspond to sub- (super-) and supercritical (subcritical) pitchfork bifurcation points for $\Gamma > 0$ ($\Gamma < 0$). For $\mu\lambda < -\beta/2$ when $\Gamma > 0$ (figure 17*a*), and $\mu\lambda > \beta/2$ when $\Gamma < 0$, the only critical point is a stable center at $C = 0$, $D = 0$. For $|\mu\lambda| < \beta/2$, the zero solution $C = 0$, $D = 0$ becomes an unstable saddle point and the stable centers are at $C = 0$, $D = \pm[(2\mu\lambda + \mathrm{sgn}(\Gamma)\beta)/\Gamma]^{1/2}$, as shown in figure 17(*b*). The equations of the two separatrices are $C^2 + D^2 \pm 2\{[\beta CD - \mu\lambda(C^2 + D^2)]/\Gamma\}^{1/2} = 0$. For $\mu\lambda > \beta/2$ when $\Gamma > 0$ (figure 17*c*), and $\mu\lambda < -\beta/2$ when $\Gamma < 0$, there are three stable centers: $C = 0$, $D = 0$ and $C = 0$, $D = \pm[(2\mu\lambda + \mathrm{sgn}(\Gamma)\beta)/\Gamma]^{1/2}$; and two unstable saddle points: $C = \pm[(2\mu\lambda - \mathrm{sgn}(\Gamma)\beta)/\Gamma]^{1/2}$, $D = 0$. For this case, the two separatrices are the circles given by $C^2 + [D^2 \pm (\beta/\Gamma)^{1/2}]^2 = 2\mu\lambda/\Gamma$.

In figure 18, the stationary solutions are compared with the experimental results of Skalak & Yarymovych (1962) for free surface Faraday problem ($\rho = 0$) with deep water ($h = \infty$). The maximum free surface displacement z_0 is defined as the maximum vertical distance between the trough and the crest of the free surface, and the response frequency $\sigma \equiv \omega_e/\Omega$. The comparison between the present results and measurements is remarkably close and is much better than that of the perturbation theory of Skalak & Yarymovych (1962).

For the stratified Faraday problem, the stationary (harmonic) responses of the present analysis are compared with the experimental measurements of Sekerzh-Zen'kovich & Kalinichenko (1979). Note that the experiments were carried out with

a free surface on the upper lid, but the free surface was not perturbed within the range of excitation frequency as indicated in Sekerzh-Zen'kovich & Kalinichenko (1979). The rectangular tank, with width $2L$=11.2 cm, was filled with distilled water (ρ=1 g/cm^3) in lower layer and kerosene (ρ=0.782 g/cm^3) in upper layer, each with equal thickness (6.8 cm). In figure 18, the dimensional amplitudes of harmonic responses (cm) are plotted versus the excitation frequency (Hz) for $m = 1$, 3/2 and 2 internal standing-wave modes. The comparisons are fairly good for the first-mode ($m = 1$) wave, but for higher modes the theoretical results overpredict the responses.

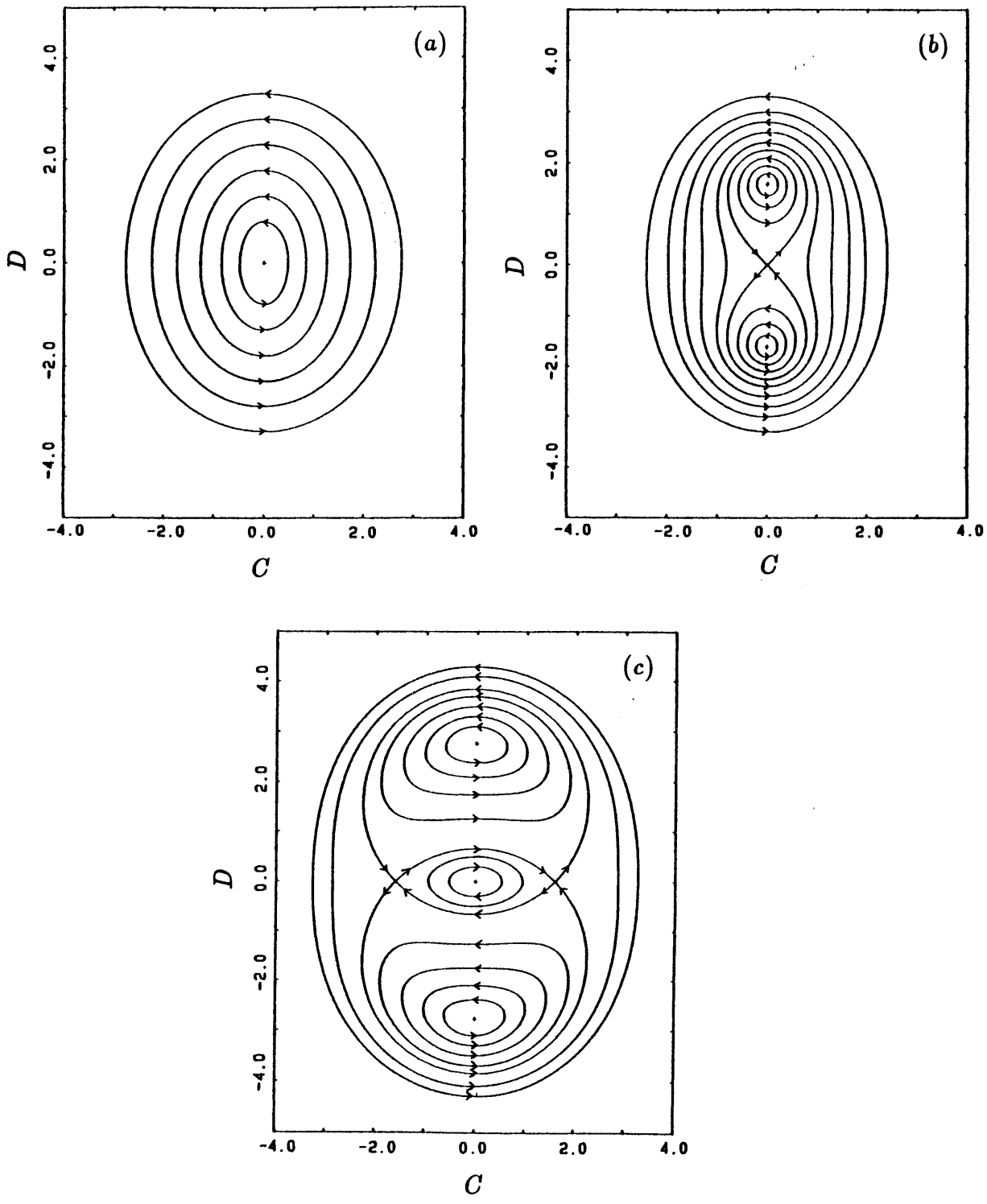

Figure 17. Phase-plane solutions of the evolution (B.4) for $\rho = 0$, $h = \infty$, and $\mu\lambda =$ (*a*) -1; (*b*) 0; (*c*) 1.

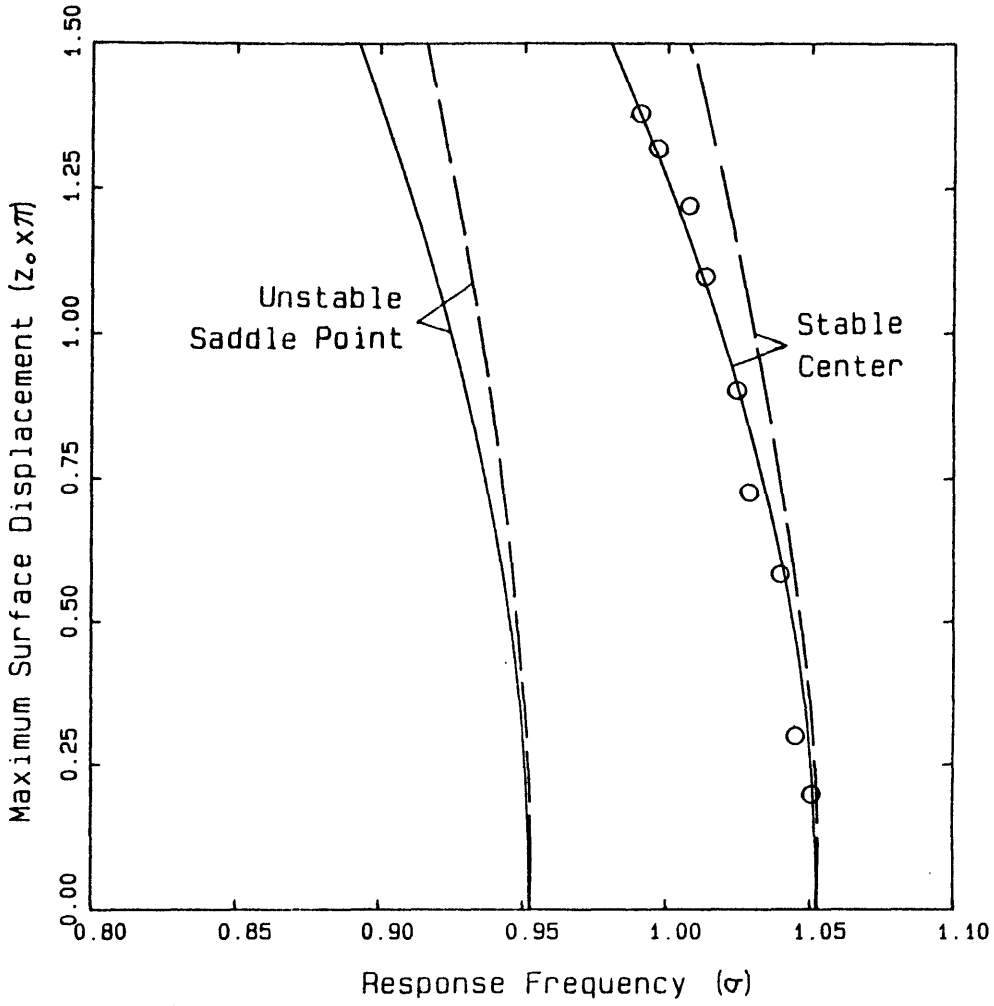

Figure 18. Comparisons between the present theory (solid lines) and third-order perturbation results (broken lines) and experimental measurements (circles) of Skalak & Yarymovych (1962) for the harmonic response of free-surface Faraday problem as a function of the response frequency $\sigma \equiv \omega\Omega$.

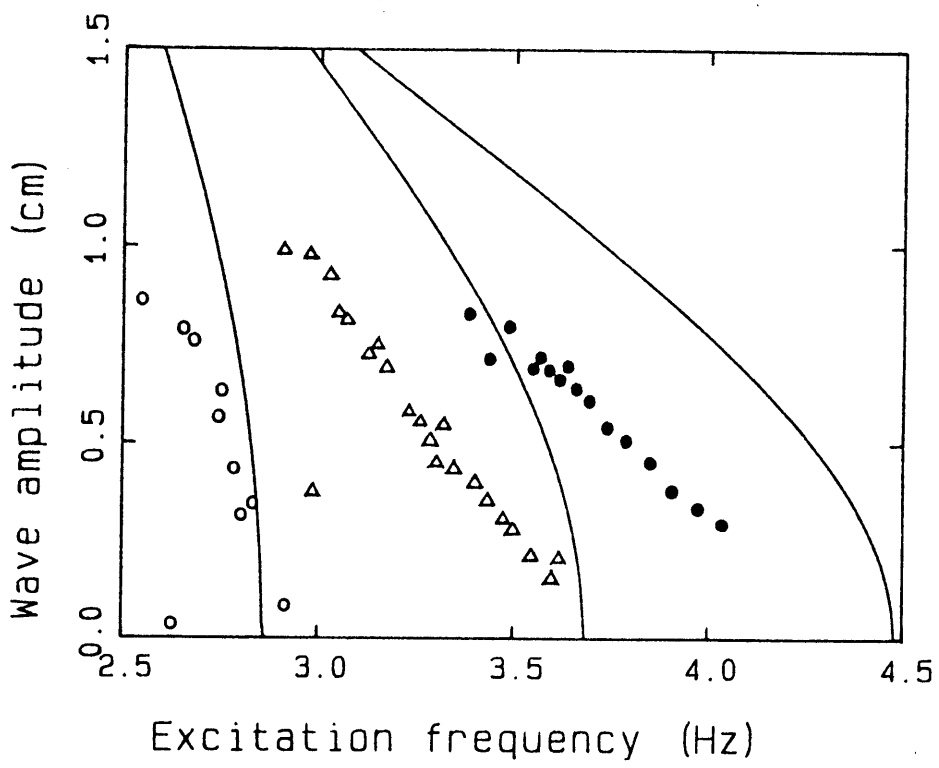

Figure 19. Comparisons between the present theory (solid lines) and experimental measurements of Sekerzh-Zen'kovich & Kalinichenko (1979) for the harmonic response of the stratified two-layer Faraday problem as a function of the excitation frequency.

Appendix C. Periodic solutions of the evolution equation governing parametric resonance

Periodic solutions of the evolution equation (B.4) (or 4.4) can be obtained analytically. Representing the complex amplitude $B(\tau)$ as

$$B(\tau) = C(\tau) + \mathrm{i}D(\tau) \equiv a(\cos\gamma + \mathrm{i}\sin\gamma), \tag{C.1}$$

where a and γ are functions of τ, (B.4) can now be written as

$$\mu\frac{\mathrm{d}\gamma}{\mathrm{d}\tau} = -2\mu\lambda + \Gamma^2 a + \beta\cos 2\gamma, \tag{C.2a}$$

and

$$\mu\frac{\mathrm{d}a}{\mathrm{d}\tau} = a\beta\sin 2\gamma. \tag{C.2b}$$

Combining (C.2a,b) and eliminating τ, we obtain

$$\frac{\mathrm{d}\gamma}{\mathrm{d}a} = \frac{\beta\cos 2\gamma - 2\mu\lambda + \Gamma^2 a}{a\beta\sin 2\gamma}. \tag{C.3}$$

Equation (C.3) is an exact integral and upon integration we have

$$2a^2(\beta\cos 2\gamma - 2\mu\lambda) + \Gamma a^4 = E, \tag{C.4}$$

where E is an integration constant. Equations (C.2b) and (C.4) can be further combined as

$$\frac{\mu}{a}\frac{\mathrm{d}a}{\mathrm{d}\tau} = \pm\sqrt{\beta - \left(2\mu\lambda + \frac{E - \Gamma a^4}{2a^2}\right)^2},$$

which gives

$$\tau = \pm\frac{\mu}{2}\int \frac{\mathrm{d}a^2}{\sqrt{a^4\beta - (2\mu\lambda a^2 + \frac{1}{2}E - \frac{1}{2}\Gamma a^4)^2}}. \tag{C.5}$$

Thus, the slow time τ is expressed as an elliptic integral of the square of the amplitude a. At any specified τ, a^2 is given in terms of an elliptic function of τ, and the phase angle γ can be obtained from (C.4).

The period of the modulation, T, may be expressed in a more explicit form. For simplicity, we classify the phase-plane trajectories of figures 17 in Appendix B into three different types: **(i)** All the trajectories in figures 17(a,b) which are outside the separatrix, and the trajectories in figure 17(c) which are outside the trajectory with $E = 0$ (this trajectory is outside the separatrix). Each of these trajectories has a different positive integration constant E. **(ii)** Trajectories in figures 17(b,c) which are inside the upper and lower separatrices forming two nested sets about the centers $C = \pm[(2\mu\lambda - \beta)/\Gamma]^{1/2}$, $D = 0$. Each pair of trajectories which are symmetric about the C axis share the same negative E value. **(iii)** Trajectories in figure 17(c) which are inside the inner separatrix and those which are outside the upper and lower separatrices but inside the $E = 0$ trajectory, forming two nested sets about the stable center $C = 0$, $D = 0$. For each trajectory in the first set with a given negative integration constant E, there is a trajectory of the other set sharing the same constant.

We rewrite (C.5) in the form:

$$\tau = \pm\frac{\mu}{\Gamma}\int \frac{\mathrm{d}s}{\sqrt{(s_1 - s)(s - s_2)(s - s_3)(s - s_4)}}, \tag{C.6}$$

where $s \equiv a^2\sqrt{\beta}$, and s_1, s_2, s_3, s_4 are the zeros of the denominator in (C.5).

For type **(i)** trajectories, only two of the zeros are real, which correspond to the intercepts of the trajectories with the C and D axes according to (C.4). From (C.6), the period for the type **(i)** trajectories is given by

$$T = \frac{4\mu}{\Gamma}\int_{a_m^2}^{a_M^2} \frac{\mathrm{d}s}{\sqrt{(a_M^2 - s)(s - a_m^2)[(s - b_1)^2 + a_1^2]}}, \tag{C.7a}$$

where a_M and a_m are respectively the maximum and minimum of the amplitude, and

$$a_1^2 = \frac{E^2}{\Gamma^2 a_M^2 a_m^2} - \left[\frac{4\mu\lambda}{\Gamma} - \frac{1}{2}(a_M^2 + a_m^2)\right]^2, \tag{C.7b}$$

$$b_1 = \frac{4\mu\lambda}{\Gamma} - \frac{1}{2}(a_M^2 + a_m^2). \tag{C.7c}$$

Equations (C.7) can be further reduced into the standard form of a complete elliptic integral (Byrd & Friedman 1954):

$$T = \frac{4\mu g}{\Gamma}\int_0^{\pi/2}\frac{\mathrm{d}\theta}{\sqrt{1-k^2\sin^2\theta}} = \frac{4\mu g}{\Gamma}K(k^2), \tag{C.8a}$$

where

$$g = \frac{2}{\sqrt{AB}}, \tag{C.8b}$$

$$k = \frac{1}{2}\sqrt{\frac{(a_M^2 - a_m^2) - (A-B)^2}{AB}}, \tag{C.8c}$$

$$A = \sqrt{(a_M^2 - b_1)^2 + a_1^2}, \tag{C.8d}$$

$$B = \sqrt{(a_m^2 - b_1)^2 + a_1^2}, \tag{C.8e}$$

and K is the complete elliptic integral of the first kind (Abramowitz & Stegun 1965). For type **(ii)** modulations, the periods of the upper and lower loops are equal and given by half times the expression (C.8a).

For type **(iii)** trajectories, the inner and outer loops associated with the same constant E have equal periods even though the motions are quite different. From (C.6), the period T can be represented as

$$T = \frac{4\mu}{\Gamma}\int_{a_m^2}^{a_M^2}\frac{\mathrm{d}s}{\sqrt{(\overline{a}_M^2 - s)(\overline{a}_m^2 - s)(a_M^2 - s)(s - a_m^2)}}, \tag{C.9}$$

where $\overline{a}_M$ and $\overline{a}_m$ are respectively the maximum and minimum of the outer trajectory, and a_M and a_m the corresponding values for the inner trajectories. Reducing to standard form, (C.9) becomes (Byrd & Friedman 1954):

$$T = \frac{4\mu g}{\Gamma}K(k^2), \tag{C.10a}$$

where

$$g = \frac{2}{\sqrt{(\overline{a}_M^2 - a_M^2)(\overline{a}_m^2 - a_m^2)}}, \tag{C.10b}$$

$$k = \sqrt{\frac{(\bar{a}_M^2 - \bar{a}_m^2)(a_M^2 - a_m^2)}{(\bar{a}_M^2 - a_M^2)(\bar{a}_m^2 - a_m^2)}}. \qquad \text{(C.10}c\text{)}$$

The preceding results for the period of the slowly-varying modulations are plotted in figure 20 as a function of the amplitude on the positive D axis for $\rho = 0$, $h = \infty$ and $\mu\lambda = -1,\ 0,\ 1$ respectively. Note that the periods are discontinuous across the separatrices and saddle points.

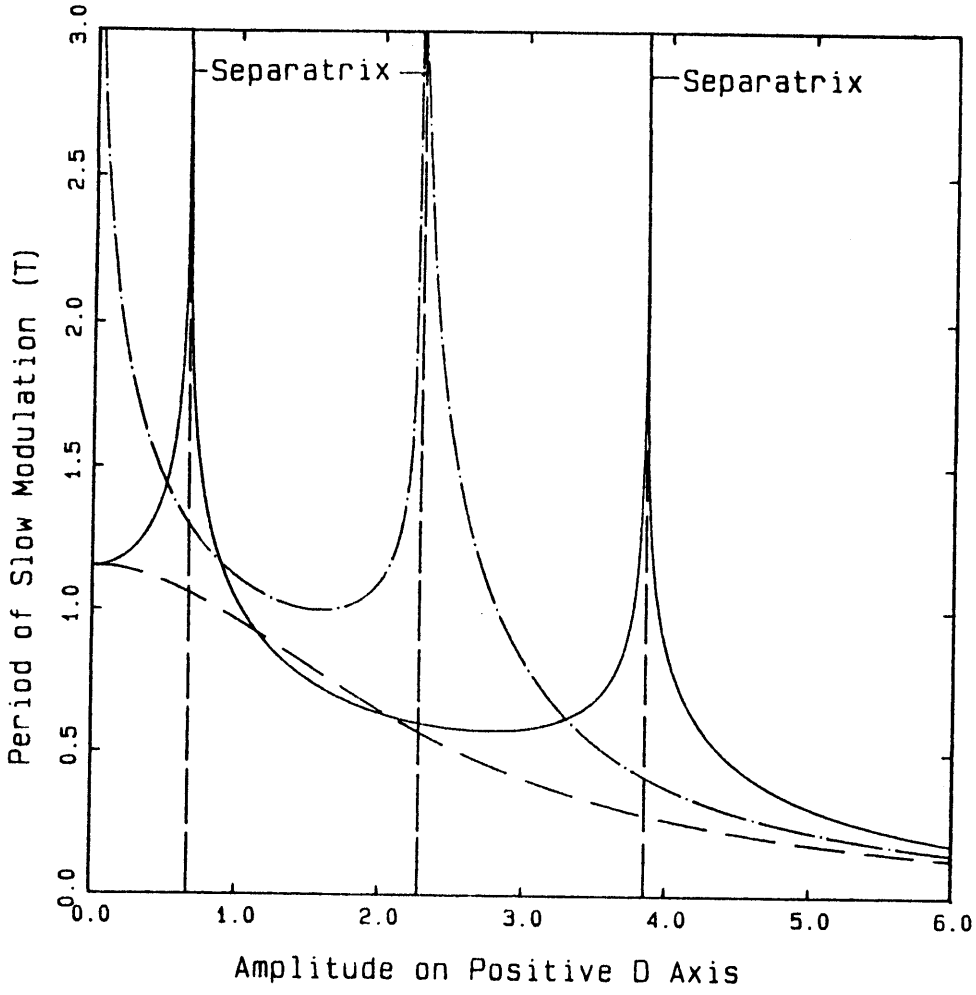

Figure 20. Period of the slowly-varying modulation of evolution equation (B.4) as a function of the amplitude on the positive D axis for $\rho = 0$, $h = \infty$ and $\mu\lambda = -1$ (broken line), 0 (dashed line) and 1 (solid line) respectively

Appendix D. Second-order solutions for the internal interaction system

The solutions Φ_2 and ζ_2 for the second-order boundary-value problem of the internal interaction case are

$$\begin{aligned}\Phi_2 = {} & \mathrm{i}(e^{-\mathrm{i}2t} - \mathrm{c.c.})\Big[\sum_{\substack{m=0\\ m\neq n}}^{\infty} d_m \cos m\pi x \cosh m\pi(z+h) - \varphi(x,z)\Big] \\ & + \mathrm{i}\big[A^2 e^{-\mathrm{i}(4+2\gamma\epsilon^{1/2})t} - \mathrm{c.c.}\big]\left[a_0 + a_1 \cos 2n\pi x \, \frac{\cosh 2n\pi(z+h)}{2n\pi \sinh 2n\pi h}\right] \\ & + \mathrm{i}\big[B^2 e^{-\mathrm{i}2t} - \mathrm{c.c.}\big]\left[b_0 + b_1 \cos 2\ell\pi y \, \frac{\cosh 2\ell\pi(z+h)}{2\ell\pi \sinh 2\ell\pi h}\right] \\ & + \mathrm{i}\big[(ABe^{-\mathrm{i}\,(3+\gamma\epsilon^{1/2})t} - \mathrm{c.c.})a_2 + (AB^* e^{-\mathrm{i}(1+\gamma\epsilon^{1/2})t} - \mathrm{c.c.})b_2\big] \\ & \qquad \times \left[\cos m\pi x \cos \ell\pi y \, \frac{\cosh(\sqrt{n^2+\ell^2}\pi(z+h))}{\sqrt{n^2+\ell^2}\pi \sinh(\sqrt{n^2+\ell^2}\pi h)}\right] \\ & + (AA^*)a_3 t \; + (BB^*)b_3 t, \end{aligned} \tag{D.1}$$

and

$$\begin{aligned}\zeta_2 = {} & -\frac{2}{\mu}(e^{-\mathrm{i}2t} + \mathrm{c.c.})\Big[\sum_{\substack{m=0\\ m\neq n}}^{\infty} d_m \cos m\pi x \cosh m\pi h - \varphi(x,0)\Big] \\ & - \frac{1}{\mu}(e^{-\mathrm{i}2t} + \mathrm{c.c.})\big(f_n - \frac{\mu}{4} f_n'\big)\cos m\pi x \\ & - \mathrm{i}\lambda\big[Ae^{-\mathrm{i}(2+\gamma\epsilon^{1/2})t} - \mathrm{c.c.}\big]\cos m\pi x \; - \mathrm{i}\lambda(Be^{-\mathrm{i}t} - \mathrm{c.c.})\cos \ell\pi y \\ & - \big[A^2 e^{-\mathrm{i}(4+2\gamma\epsilon^{1/2})t} + \mathrm{c.c.}\big]\tilde{a}_1 \cos 2n\pi x \; - \big[B^2 e^{-\mathrm{i}2t} + \mathrm{c.c.}\big]\tilde{b}_1 \cos 2\ell\pi y \\ & - \big[(ABe^{\mathrm{i}(3+\gamma\epsilon^{1/2})t} + \mathrm{c.c.})\tilde{a}_2 + (AB^* e^{-\mathrm{i}(1+\gamma\epsilon^{1/2})t} + \mathrm{c.c.})\tilde{b}_2\big]\cos n\pi x \cos \ell\pi y \\ & - (AA^*)\tilde{a}_3 \cos 2n\pi x \; - (BB^*)\tilde{b}_3 \cos 2\ell\pi y, \end{aligned} \tag{D.2}$$

where

$$\begin{aligned} a_0 &= -\frac{1}{256}(n^2\pi^2\mu^2 + 48), \\ b_0 &= -\frac{1}{32}(3 + \mu_y^2 \ell^2 \pi^2), \\ a_1 &= \frac{n^2\pi^2\mu}{256}(3n^2\pi^2\mu^2 - 48), \\ b_1 &= -\frac{3}{8}\mu_y \ell^2 \pi^2 (1 - \mu_y^2 \ell^2 \pi^2), \end{aligned}$$

$$a_2 = \frac{(n^2+2\ell^2)\pi^2\mu^2 - 42}{72\tilde{\mu} - 8\mu},$$

$$b_2 = \frac{(2\ell^2-n^2)\pi^2\mu^2 + 6}{8\tilde{\mu} - 8\mu},$$

$$a_3 = \frac{1}{32}(16 - n^2\pi^2\mu^2),$$

$$b_3 = \frac{1}{8}(1 - \mu_y^2\ell^2\pi^2),$$

$$\tilde{a}_1 = \frac{n^2\pi^2\mu}{1024}(3n^2\pi^2\mu^2 - 16),$$

$$\tilde{b}_1 = \frac{1}{16}\mu_y\ell^2\pi^2(1 - 3\mu_y^2\ell^2\pi^2),$$

$$\tilde{a}_2 = \frac{\ell^2\pi^2\mu}{16}(3\ell^2\pi^2\mu^2 - 1),$$

$$\tilde{b}_2 = \frac{(2\ell^2-n^2)\pi^2\mu\tilde{\mu} + 6}{8\tilde{\mu} - 8\mu},$$

$$\tilde{a}_3 = \frac{3(n^2+2\ell^2)\pi^2\mu\tilde{\mu} - 14}{8\tilde{\mu} - 8\mu},$$

$$\tilde{b}_3 = \frac{1}{8\mu_y}(1 + \mu_y^2\ell^2\pi^2),$$

$$d_0 = -\frac{h^2}{24} - \frac{\mu_y h}{8},$$

$$d_m = \frac{4 + m\pi\mu_y \tanh m\pi h - \frac{8}{m\pi h}\tanh\frac{m\pi h}{2}}{m^2\pi^2(m\pi\mu_y \sinh m\pi h - 4\cosh m\pi h)},$$

and

$$\tilde{\mu} = \frac{1}{\sqrt{n^2+\ell^2}\pi \tanh\sqrt{n^2+\ell^2}\pi h}.$$

References

Abramowitz, M. & Stegun, I.A. 1965. *Handbook of Mathematical Functions.* Dover.

Arnol'd, V.I. 1978. *Mathematical Methods of Classical Mechanics.* Springer.

Benjamin, T.B. & Feir, J.E. 1967. The disintegration of wave trains in deep water. Part 1. Theory. *J. Fluid Mech.* **27**, 417–430.

Benettin, G., Galgani, L. & Strelcyn, J.M. 1976. Kolmogorov entropy and numerical experiments. *Phys. Rev.* **A14**, 2338–2345.

Byrd, P.F. & Friedman, M.D. 1954. *Handbook of Elliptic Integrals for Physicists and Engineers.* Springer.

Chirikov, B. 1979. A universal instability of many dimensional oscillation systems. *Phys. Rep.* **52**, 263–379.

Ciliberto, S. & Gollub, J.P. 1984. Pattern competition leads to chaos. *Phys. Rev. Lett.* **52**, 922–925.

Ciliberto, S. & Gollub, J.P. 1985*a*. Chaotic mode competition in parametrically forced surface waves. *J. Fluid Mech.* **158**, 381–398.

Ciliberto, S. & Gollub, J.P. 1985*b*. Phenomenological model of chaotic mode competition in surface waves. *Il Nuovo Cimento* **6D**, 309–316.

Faraday, M. 1831. On a peculiar class of acoustical figures; and on certain forms assumed by groups of particles upon vibrating elastic surface. *Philos. Trans. R. Soc. London.* **121**, 299–340.

Feng, Z.C. & Sethna, P.R. 1989. Symmetry-breaking bifurcations in resonant surface waves. *J. Fluid Mech.* **199**, 495–518.

Fultz, D. 1962. An experimental note on finite-amplitude standing gravity waves. *J. Fluid Mech.* **13**, 193–212.

Funakoshi, M. & Inoue, S. 1987. Chaotic behavior of resonantly forced surface water waves. *Phys. Lett.* **A121**, 229–232.

Funakoshi, M. & Inoue, S. 1988. Surface waves due to resonant horizontal oscillation. *J. Fluid Mech.* **192**, 219–247.

Garrett, C.J.R. 1970. On cross-waves. *J. Fluid Mech.* **41**, 837–849.

Gollub, J.P. & Meyer, C.W. 1983. Symmetry-breaking instabilities on a fluid surface. *Physica* **6D**, 337–346.

Gu, X.M. & Sethna, P.R. 1987. Resonant surface waves and chaotic phenomenon. *J. Fluid Mech.* **183**, 543–565.

Havelock, T.H. 1929. Forced surface-waves on water. *Phil. Mag.* **8**, 304–311.

Keolian, R., Turkevich, L.A., Putterman, S.J. & Rudnick, I. 1981. Subharmonic sequences in the Faraday experiment: Departures from period doubling. *Phys. Rev. Lett.* **47**, 1133–1136.

Lin, J.N. & Howard, L.N. 1960. Non-linear standing waves in a rectangular tank due to forced oscillation. *MIT Hydrodynamics Laboratory, Rep.* 44.

Meron, E. & Procaccia, I. 1986*a*. Theory of chaos in surface waves: The reduction from hydrodynamics to few-dimensional dynamics. *Phys. Rev. Lett.* **56**, 1323–1326.

Meron, E. & Procaccia, I. 1986*b*. Low-dimensional chaos in surface waves: Theoretical analysis of an experiment. *Phys. Rev.* **A34**, 3221–3237.

Meron, E. & Procaccia, I. 1987. Gluing bifurcations in critical flows: The route to chaos in parametrically excited surface waves. *Phys. Rev.* **A35**, 4008–4011.

Miles, J.W. 1984*a*. Nonlinear Faraday resonance. *J. Fluid Mech.* **146**, 285–302.

Miles, J.W. 1984*b*. Resonantly forced surface waves in a circular cylinder. *J. Fluid Mech.* **149**, 15–31.

Miles, J.W. 1988. Parametrically excited, standing cross-waves. *J. Fluid Mech.* **186**, 119–127.

Nayfeh, A.H. 1987. Surface waves in closed basins under parametric and internal resonances. *Phys. Fluids* **30**, 2976–29883.

Oberhettinger, F. 1973. *Fourier Expansions, A Collection of Formulas.* Academic.

Ockendon, J.R. & Ockendon, H. 1973. Resonant surface waves in a circular cylinder. *J. Fluid Mech.* **59**, 397–413.

Penney, W. G. & Price, A.T. 1952. Some gravity wave problem in the motion of

perfect liquids. Part II. Finite periodic stationary gravity waves in a perfect liquid. *Phil. Trans.* A **244**, 254–284.

Sekerzh-Zen'kovich, S. Ya. & Kalinichenko, V.A. 1979. Excitation of internal waves in a two-layered liquid by vertical oscillations. *Sov. Phys. Dokl.* **24**, 960–961.

Shemer, L. & Kit, E. 1988. Study of the role of dissipation in evolution of nonlinear sloshing waves in a rectangular channel. *Fluid Dyn. Res.* **4**, 89–105.

Simonelli, F. & Gollub, J.P. 1989. Surface wave mode interactions: effects of symmetry and degeneracy. *J. Fluid Mech.* **199**, 471–494.

Skalak, R. & Yarymovych, M.I. 1962. Forced large amplitude surface waves. *Proc. 4th U.S. Nat. Cong. Appl. Mech.* 1411–1418.

Struble, R.A. 1963. Oscillations of a pendulum under parametric excitation. *Q. Appl. Math.* **21**, 121–131.

Tabor, M. 1981. The onset of chaotic motion in dynamical systems. *Adv. Chem. Phys.* **46**, 73–151.

Tadjbakhsh, I. & Keller, J.B. 1960. Standing surface waves of finite amplitude. *J. Fluid Mech.* **8**, 442–451.

Taylor, G.I. 1953. An experimental study of standing waves. *Proc. Roy. Soc.* A **218**, 44–59.

Umeki, M. & Kambe, T. 1989. Nonlinear dynamics and chaos in parametrically excited surface waves. *J. Phys. Soc. Japan* **58**, 140–154.

Ursell, F., Dean, R.G. & Yu, Y.S. 1959. Forced small-amplitude water waves: a comparison of theory and experiment. *J. Fluid Mech.* **7**, 33–52.

Zufiria, J. 1988. Oscillatory spatially periodic weakly nonlinear gravity waves on deep water. *J. Fluid Mech.* **191**, 341–372.

II

Interactions between a free surface and a shed vortex sheet

The nonlinear interactions between a free surface and a shed vortex shear layer in the inviscid wake of a surface-piercing plate is studied numerically using mixed-Eulerian-Lagrangian method. For the plate with initial submergence d and moves abruptly from rest to a constant horizontal velocity U, the problem is governed by a single parameter, the Froude number $F_n = U/\sqrt{gd}$, where g is the gravitational acceleration. Depending on the Froude number, three classes of interaction dynamics (subcritical, transcritical and supercritical) are identified in the wake of the plate. The early stage of the free surface and vortex sheet evolutions are similar for the three cases: the shed vortex sheet quickly rolls up into a single-branched spiral and the forward side of free surface rapidly forms a thin jet. For subcritical Froude numbers ($F_n <\sim 0.7$), the free surfaces begin to plunge on both forward and lee sides of the plate before significant interactions with the vortex sheet occur. For both transcritical and supercritical Froude numbers, the depressed deformation of the free surface behind the plate stretches the vortex sheet and finite-amplitude Kelvin-Helmholtz instabilities arise which roll up into double-branched spirals. In the transcritical range ($F_n \sim 0.7 - 1.0$), the interaction between the free surface and the Kelvin-Helmholtz instabilities remains weak, which allows the latter to roll up continuously into a series of double-branched spirals. For supercritical case ($F_n >\sim 1.0$), the double-branched spiral grows and entrains into the free surface resulting in large surface deformations, and the lee side free surface near the plate moves downward continuously which eventually sluices from the lower tip of the plate.

1. Introduction

The fundamental problem of free surface and shear layer interaction attracted increasing attention in recent years motivated by the observation of persistent observable features in the ship wake. Considerable progress in both experimental investigation and numerical simulation of such phenomena has been made with emphasis on the interaction dynamics between the free surface and a given vortical flow. An example is the recent work of Yu & Tryggvason (1990), who studied numerically the interaction of two-dimensional vortex flows with a free surface. The vorticity is modeled as point vortices, vortex sheets and vortex patches. They found that distinct free surface motions are generated depending on the initial vortex configuration.

Another recent numerical experiment is that of Dimas (1991) in which a shear flow with a mean velocity profile in the vertical direction is used to simulate the wake behind a two-dimensional submerged body. An Euler equation subject to free-surface boundary conditions is solved numerically. It is found that for a sufficiently large submergence, the interaction between the shear layer and the free surface is suppressed, and the flow reaches a quasi-steady state. For a smaller submergence, vortices form very near the free surface causing breaking surface waves. The mechanisms involved in the interaction dynamics between the free surface and vorticity flow, however, were not completely identified. Moreover, no quantification of the interaction features with respect to the submergence and velocity of the body was carried out.

The primary goal of this research is to identify and quantify, through careful numerical simulations, the basic mechanisms of the fully nonlinear body-vortex-free surface interactions including generation, evolution and the coupled dynamics. Of special interest is the understanding and quantification of the critical role of the Froude number.

To reach these objectives, we consider the canonical problem of a thin vertical

surface-piercing plate of initial submergence d, moving abruptly from rest to a constant horizontal velocity U. The free surface rises sharply on the forward face and is drawn down on the rearward face into close proximity of the trailing vortex sheet shed from the lower edge of the strut. The resulting interaction dynamics among the body, free surface and the vortex sheet in an *actual* wake are extremely complex and are heretofore not completely understood. Significantly, the present problem is governed by only a single parameter, the Froude number $F_n = U/\sqrt{gd}$, where g is the gravitational acceleration, so that a systematic study varying this parameter allows us to reach a complete understanding and quantification of the underlying mechanisms.

One important distinction between this and previous computational studies in which the strengths and positions of the vorticity are prescribed as initial conditions, is that the vortex shear layer here is shed by the strut under the influence of the free surface and vorticity flow, *i.e.*, in the actual wake of the body. While the problem is simplified by a body possessing a sharp edge for which simple models for vortex generation can be used, the problem includes all the important interaction dynamics of vortex-body-free surface flows. Indeed, from a computational point of view, the present model is the most general and in fact the most difficult of all two-dimensional vortex-free surface interaction problems. Aside from fundamental scientific interests, the present problem is of practical importance in the analysis of damping of shallow-draft bodies, the performance of lifting surfaces near a free surface, as well as the wave resistance and disturbances generated by the operation of such surfaces.

In the present work, the fluid is assumed to be inviscid and the free shear layer confined in an infinitesimal vortex sheet, outside of which the flow is irrotational. Thus the characteristics of real, high Reynolds number flows are approximated by assuming the effects of viscosity to be confined to infinitesimally-thin boundary and shear layers. The validity of such discrete-vortex approximations has been controversial, and is the subject of vigorous debate since the pioneering work of

Rosenhead (1931) and its subsequent criticism by Birkhoff & Fisher (1959). A comprehensive review of the various vortex methods and their practical applications can been found in Sarpkaya (1989), which also includes an extensive bibliography of these and related work.

For an infinitesimal vortex sheet, it is well known that the rate of growth of Kelvin-Helmholtz instabilities increases with the wavenumber of the disturbance (*e.g.*, Lamb 1932). For initial conditions which are not smooth, then, the resulting evolution develops into singularities within finite time (*cf.*, Moore 1979), and the problem is strictly not well posed. In practice, such singularities manifest themselves in the form of numerical instabilities such as saw-tooth oscillations (Longuet-Higgins & Cokelet 1976) on the free surface and irregular motions on a thin vortex sheet (Moore 1981). In the physical problem, such singularities are absent due to the presence of (a small amount of) viscosity. By introducing a small degree of numerical filtering (or damping) of the highest wavenumbers, the singularity of the mathematical problem is likewise removed in the computational problem. It should be point out that such filtering/damping of short waves is essential in any inviscid model, since the presence of strong nonlinear interactions will inevitably cause energy to transfer to and ultimately accumulate at the highest wavenumber modes represented.

There have been a number of successful filtering/damping techniques for direct simulation of vortex (and free-surface) flows. These include smoothing (Longuet-Higgins & Cokelet 1976), rediscretization (Fink & Soh 1974) and regularization methods (Chorin & Bernard 1973), which modify or stabilize the numerical scheme. A common feature of these techniques is the effective introduction of damping into the dynamical system, or of a filter which suppresses the unstable modes.

A common criticism of all these techniques is that the precise relationship between the computational results and the 'exact' mathematical solution and ultimately the actual physical problem is unclear. Our view is that with the limitations of the mathematical formulation in representing the physical model, and with the

complexity of the physical system itself, there is much to be gained by accurate simulation and quantification of the global features despite the inevitable use of stabilizing techniques. The alternative of adopting full viscous free-surface codes is prohibitive in most cases. We are especially encouraged by the promising results of Vinje & Brevig (1981) for simulation of nonlinear free surface motions, and by Faltinsen & Pettersen (1982) for vortex sheet shed from a moving body. Our goal is that, by performing accurate numerical simulations and systematic convergence tests especially with respect to the regularization parameters, a reliable description of the fundamental physical processes can be obtained.

Mathematical formulation of the mixed first- and second-kind Cauchy integration equations which describe the initial-boundary-value problem is given in §2. The mixed-Eulerian-Lagrangian method we employ and the detailed numerical implementation are described in §3. Of special importance is the use of cubic smoothing splines and an adaptive curvature-controlled rediscretization algorithm to suppress spurious short-wavelength instabilities, and to optimize the resolution and efficiency of the simulations. Extensive numerical tests to validate the accuracy and show the convergence of the numerical scheme are also presented. Detailed simulation results for the entire range of interest of the Froude number are given in §4. Three critical ranges of Froude number — subcritical, transcritical and supercritical — are identified based on the features of interaction between the free surface and the shed vortex sheet which are described in detail. Finally, physical properties of the motions which characterize the Froude number dependence are presented.

2. Mathematical formulation

2.1. Mixed first- and second-kinds integral equation

We consider as a canonical problem the abrupt starting from rest to horizontal velocity U of an infinitesimally thin vertical surface-piercing strut of initial submergence d. A thin shear layer is shed from the edge of the submerged strut continuously as time proceeds. The fluids, excluding the shear layer, are assumed to be inviscid, incompressible and irrotational which imply the existence of an analytic velocity potential $\phi(x,y,t)$ and stream function $\psi(x,y,t)$. We define Cartesian coordinates with the origin at the interaction point of the undisturbed free surface ($y = 0$) and the rest position of the plate ($x = 0$), with y positive up. Significantly, for deep water, this problem is governed by only one parameter, the Froude number $F_n = U/\sqrt{gd}$, where g is the gravitational acceleration. In the following, length and time units are chosen so that d, g=1. The computational domain is enclosed by imposing periodic boundary conditions on the upstream ($x = \ell/2$) and downstream ($x = -\ell/2$) vertical boundaries. The contour of the domain consists of the free surface (C_f), the plate with fluid on one side (C_p), the submerged portion of plate (C_s) and the vortex sheet (C_v).

Since the complex potential $\beta(z,t) = \phi(x,y,t) + \mathrm{i}\psi(x,y,t)$ is analytical inside the fluid domain, where $z = x + \mathrm{i}y$, Cauchy's integral theorem gives for each time instant t:

$$\beta(z_k,t) = \frac{1}{\mathrm{i}\pi} \int\!\!\!\!\!\!-_{C_f \cup C_p} \beta(z,t)K(z;z_k)dz + \frac{1}{\mathrm{i}\pi} \int_{C_s \cup C_v} [\phi(z,t)]K(z;z_k)dz + \mathrm{i}2\tilde{\beta}_\infty(t); \quad (2.1)$$

when $z_k \in C_f$ and C_p, and

$$\beta^{\pm}(z_k,t) = \pm\frac{1}{2}[\phi(z_k,t)] + \frac{1}{\mathrm{i}2\pi} \int_{C_f \cup C_p} \beta(z,t)K(z;z_k)dz + \frac{1}{\mathrm{i}2\pi} \int\!\!\!\!\!\!-_{C_s \cup C_v} [\phi(z,t)]K(z;z_k)dz + \mathrm{i}\tilde{\beta}_\infty(t)\} \quad (2.2)$$

when $z_k \in C_s$ and C_v; where $[\phi(z,t)] = \phi^+ - \phi^-$ is the potential jump across C_s and C_v, and $\tilde{\beta}_\infty(t)$ is a complex constant resulting from contour integration along $z = [-\ell/2 - i\infty, \ell/2 - i\infty]$. The kernel function,

$$K(z; z_k) = (\frac{\pi}{\ell}) \cot[(\frac{\pi}{\ell})(z - z_k)], \tag{2.3}$$

is the complex potential which satisfies the Laplace's equation inside the fluid domain excluding $z = z_k$ and with periodic boundary condition at $x = \pm\ell/2$. We define the direction of contour integration in the anticlockwise sense such that wind/lee side of the plate and shear layer are the positive/negative side of the contour. Taking the imaginary and real parts of (2.1) for $z_k \in C_f$ and C_p respectively, we obtain second-kind Fredholm integral equations for ψ on C_f and ϕ on C_p. The imaginary part of (2.2) when $z_k \in C_s$ gives first-kind integral equations for the potential jump $[\phi]$ on C_s. To avoid a weak singularity at the intersection point we specify the known β at both upper $(C_f \cap C_p)$ and lower $(C_f \cap C_p \cap C_s)$ intersection points (Lin 1984).

2.2. *Boundary and initial conditions*

On the plate surfaces C_p and both sides $(+/-)$ of C_s, the prescribed uniform horizontal velocity gives the Neumann boundary condition in term of the stream function as

$$\psi(x = t, y, t) = y \qquad (z \in C_p \cup C_s). \tag{2.4}$$

On the free surface C_f, the kinematic boundary condition is

$$\frac{\mathrm{D}z}{\mathrm{D}t} = \frac{\partial \beta^*}{\partial z} = w^* \qquad (z \in C_f), \tag{2.5}$$

where $\mathrm{D}/\mathrm{D}t$ is the material time derivative, and $w^*(z,t) = u(x,y,t) + \mathrm{i}v(x,y,t)$ is the conjugate of complex velocity. From Bernoulli's equation, the dynamic boundary condition for zero atmospheric pressure on the free surface C_f gives

$$\frac{\mathrm{D}\phi}{\mathrm{D}t} = \frac{1}{2} w w^* - \frac{1}{F_n^2} \Im(z) \qquad (z \in C_f). \tag{2.6}$$

The vortex sheet C_v is a material surface with zero pressure jump across the shear layer and is convected according to

$$\frac{\mathrm{D}z}{\mathrm{D}t} = \frac{1}{2}(w^+ + w^-) \qquad (z \in C_v). \tag{2.7}$$

The unsteady Kutta condition at the separation point is that the flow leaves the trailing edge tangentially to the surface of the strut. Such a condition ensures that at the trailing edge the velocity is finite and the pressure jump vanishes. Applying this Kutta condition to the unsteady Bernoulli's equation gives the rate of shear strength shedding at the tip of the plate as

$$\frac{\mathrm{D}[\phi]}{\mathrm{D}t} = \frac{1}{2}(w^- w^{-^*} - w^+ w^{+^*}) \qquad (z = t + \mathrm{i}). \tag{2.8}$$

The initial conditions at $t = 0$ are specified with the free surface quiescent ($\phi = 0$ and $\Im(z) = 0$) and a starting point vortex shed out according to the similarity solution (*e.g.*, Graham 1983) with the strength and position given.

2.3. *Unsteady force and energy*

The unsteady horizontal force F_x acting on the plate can be calculated by integrating the pressure distributions on both sides of the plate. An alternative formulation of F_x, which inferred from the conservation of momentum as shown in Newman (1977), can be derived for the present flow motion in nondimensional form as

$$F_x = -\frac{\mathrm{d}}{\mathrm{d}t}\int\limits_{C_f \cup C_p} \phi\, n_x \,\mathrm{d}s \; - \frac{\mathrm{d}}{\mathrm{d}t}\int\limits_{C_s \cup C_v} [\phi]\, n_x \,\mathrm{d}s \; - \frac{1}{F_n^2}\int\limits_{C_f \cup C_p} y\, n_x^+ \,\mathrm{d}s, \tag{2.9}$$

where n_x is the horizontal component of the unit outward-pointing normal vector. The third integral vanishes in the present formulation due to the periodic conditions on the up- and downstream boundaries. The first two integrals in the unsteady force formulation (2.9) also give the nondimensional work W done on the fluids by the forced plate motion.

The nondimensional total energy of the flow motions is

$$E = \frac{1}{2}\int\limits_{C_f \cup C_p} \phi \,\mathrm{d}\psi + \frac{1}{2}\int\limits_{C_s \cup C_v} [\phi] \,\mathrm{d}\psi + \frac{1}{2F_n^2}\int\limits_{C_f} y^2\, n_y \,\mathrm{d}s, \tag{2.10}$$

where n_y is the component of the unit outward-pointing normal in the vertical direction. The first and second integrals correspond to the kinetic energies of the free surface and vortex sheet motions respectively. The third integral represents the potential energy of the free surface. The inviscid flow formulation of the problem guarantees that the conservation of energy as $W = E$.

3. Numerical implementation

3.1. Mixed-Eulerian-Lagrangian method

The initial-boundary-value problem of (2.1) – (2.8) in §2, including the motions of the free surface, shear layer and moving plate, is solved using a mixed-Eulerian-Lagrangian approach. In order to solve the mixed first- and second-kind integral equations, contour integrations in (2.1) and (2.2) are approximated by representing the contour boundaries by piecewise-linear segments and piecewise-linear distributions of β and $[\phi]$ along the segments. The discrete forms of the mixed first- and second-kind integral equations are then solved by evaluating the integrations at suitable collocation points z_k. For the second-kind integral equations, the collocation points are on the nodes of the line segments. For the first-kind equations, the z_k are placed at the midpoints of the segments. In order to obtain two more equations for the complex constant $\tilde{\beta}_\infty(t)$, we also collocate at the upper intersection point and at the midpoint of the segment above the lower intersection point. Details of the numerical implementation in discretizing the integral equations are given in appendix A.

The evolutions of the free surface position and potential are updated by integrating in time the kinematic and dynamic free surface boundary conditions (2.5) and (2.6), where the complex velocities $w(z,t) = \partial\beta(z,t)/\partial z$ are calculated using three-point Lagrange formulae. The velocities at the intersection points are obtained by differentiating the values of β at nodes on the plate next to the intersection points. The explicit fourth-order Runge-Kutta scheme, which is conditionally stable for the linearized free surface boundary conditions, is used to carry out the time integration.

The potential jump at the separation point of the plate is updated according to (2.8), where the velocities $w^{\pm}$ are calculated by differentiating the values of $\beta^{\pm}$ at the midpoints of segments on the submerged plate next to the separation

point using three-point Lagrange formulae. A new shear layer segment is shed out continuously at each time step. The new segment has an updated potential jump at the adjacent to the separation point, and has the previous time step potential jump at the other end which is convected from the separation point. The vortex shear layer, which is a material surface, is convected numerically by a fourth-order Runge-Kutta integrating scheme according to the evolution equation (2.7).

3.2. *Adaptive rediscretization algorithm*

In order to control the growth of short-wavelength instabilities and to optimize the computation efficiency, we use a rediscretizing algorithm based on cubic smoothing spline and mesh-function-controlled node adjustment schemes. After the Lagrangian boundaries (C_f and C_v) are updated, smoothing cubic splines are calculated in the least square sense to fit the nodes of meshes (*e.g.,* de Boor 1978; Lancaster & Šalkauskas 1990). The free surface and the shear layer are then rediscretized based on equidisdistribution of the mesh function (Hyman & Naughton 1985) on each segment. The details of the adaptive rediscretization algorithm are described in appendix B. Through all of the computations, we found such adaptive rediscretization algorithm performs much more robustly and efficiently than applying smoothing formula (Longuet-Higgins & Cokelet 1976) or using equal-segment regridding for mixed-Eulerian-Lagrangian method. As a test and a demonstration, the adaptive rediscretization algorithm is applied to the motions of a plunging free surface and the periodic double-branched spiral roll-up, both with abrupt geometric changes and drastic evolutions. The results are shown by systematically changing the four parameters governing the rediscretization algorithm: smoothing parameter λ, mesh function increment I_κ, maximal and minimal segment sizes h_{max} and h_{min}.

A plunging breaker is generated by imposing a linear, sinusoid free-surface wave with 0.1 steepness and unit periodic wavelength as the initial condition. Figure 1 shows the profiles of the plunging breaker at $t = 1.0, 1.2, 1.4$ and 1.5 for different values of smoothing parameter: $\lambda = 10^6, 10^7, 10^8$ and ∞ with 80 segments per wavelength. Smoothing spline fitting without nodal redistribution is applied to the free surface position and the potential at every fifth time step. The infinite λ corresponds to the situation where no smoothing effect is applied. The free surface profiles, except near the tips of the plunger, are indistinguishable for the range of λ. The profile of the plunger quickly converges to the nonsmoothing one with increasing λ. The absolute error of volume conservation and the total energy loss

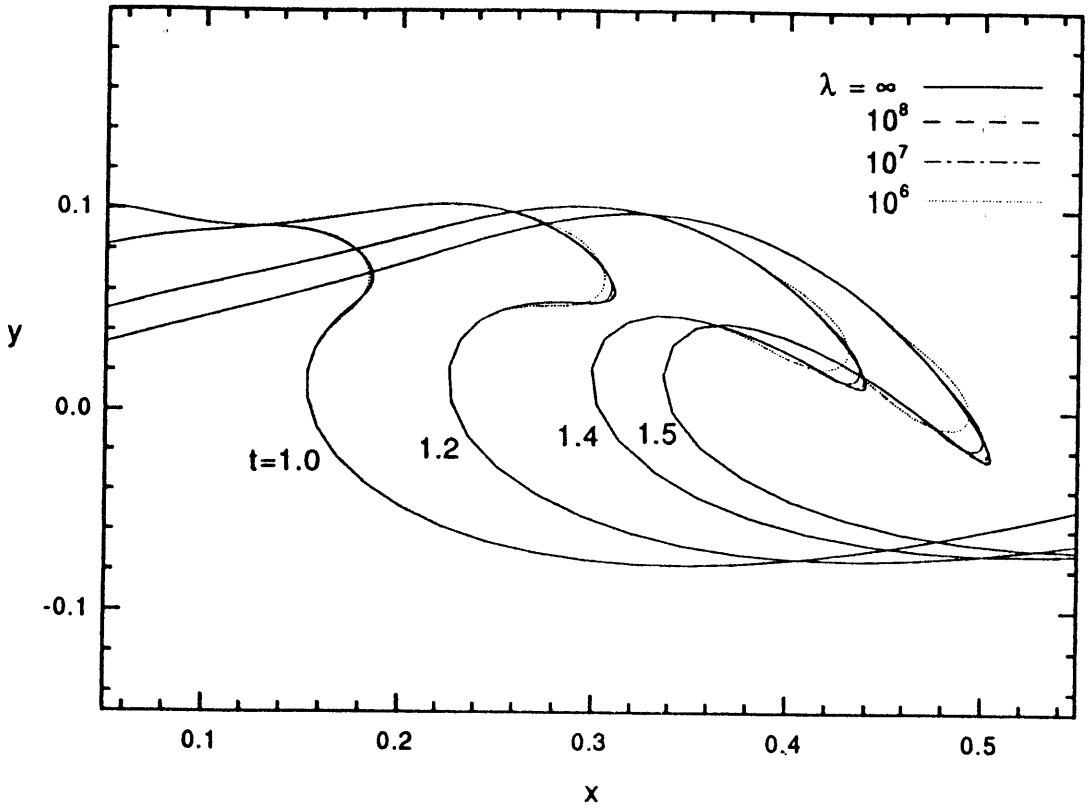

Figure 1. Free surface profiles of plunging breaker at $t = 1.0$, 1.2, 1.4 and 1.5 for different values of smoothing parameter: $\lambda = 10^6$, 10^7, 10^8 and ∞.

(%) at $t = 1.2, 1.4$ and 1.5 for different λ are summarized in Table 1. The volume error is less than 4 digits and the energy loss is less than 1% of the total energy up to $t = 1.5$ right before the reentry of the plunger. The effect of changing the maximal segment size h_{max} and the mesh function increment I_κ are shown in Table 2 for the volume error and energy loss at $t = 1.4$ with $\lambda = 10^{10}$, $I_\kappa = 2\pi/30$, $h_{min} = 0.001$ h_{max} =0.04, 0.035, 0.03, 0.025 and 0.02; and $\lambda = 10^{10}$, $h_{max} = 0.025$, $h_{min} = 0.001$, $I_\kappa = 2\pi/10$, $2\pi/15$, $2\pi/20$, $2\pi/25$ and $2\pi/30$ respectively. Both volume error and energy loss decrease with decreasing h_{max}. The energy loss reduces when I_κ decreases (finer grid), whereas the volume conservation changes from losing to gaining error. The minimal segment size h_{min}, which controls the highest resolution of discretization is found to have only negligible effect on the simulation results.

	Volume error			Energy loss (%)		
λ	$t = 1.2$	1.4	1.5	$t = 1.2$	1.4	1.5
10^6	0.000383	0.000480	0.000510	0.3395	0.6793	0.9415
10^7	0.000343	0.000407	0.000414	0.4101	0.8005	1.1014
10^8	0.000340	0.000401	0.000406	0.4090	0.8045	1.1130
10^{40}	0.000340	0.000401	0.000405	0.4082	0.8047	1.1153
∞	0.000340	0.000401	0.000405	0.4082	0.8047	1.1153

Table 1. Absolute error of volume conservation and total energy loss (%) for the plunging free-surface simulation at $t = 1.2$, 1.4 and 1.5 with varied smoothing parameter λ.

h_{max}	Volume error	Energy loss(%)	I_κ	Volume error	Energy loss(%)
0.040	0.000386	3.0828	$2\pi/10$	-0.000265	3.2012
0.035	0.000276	2.4477	$2\pi/15$	-0.000065	2.3279
0.030	0.000254	1.6191	$2\pi/20$	0.000065	1.7173
0.025	0.000133	1.3357	$2\pi/25$	0.000095	1.5451
0.020	0.000049	0.9918	$2\pi/30$	0.000133	1.3357

Table 2. Absolute error of volume conservation and total energy loss (%) for the plunging free-surface simulation at $t = 1.4$, with varied maximal segment size h_{max} and mesh-function increment I_κ.

The adaptive rediscretization algorithm is also applied to the roll-up of a periodic vortex sheet with constant strength and a small amplitude perturbation as in Krasny (1986). We plot in figure 2 the vortex roll-up at $t = 2.0$ with $h_{max} = 0.1$, $h_{min} = 0.0025$, $I_\kappa = \pi/10$ and $\lambda = 10^{40}$, 10^{10} and 10^6. The inner spiral of the roll-up is amalgamated into a point vortex, as described in the next section, with 2π cut-off winding angle. The results show very little difference in the vortex sheet roll-up between the strong smoothing ($\lambda = 10^6$) and the nonsmoothing case ($\lambda = 10^{40}$). Also plotted in figure 2 are the results using the vortex-blob method (Krasny 1986) with the blob radius $\delta = 0.12$ and 500 vortex blobs. The comparison between the solutions by the present scheme and the vortex blob method is very close for the outer spiral turns demonstrating the accuracy of the present result and also the minor effect of amalgamation on the global motions. Figure 3 shows the roll-up at $t = 2.0$ for different mesh-function increments $I_\kappa = \pi/15$, $\pi/10$ and $\pi/5$. The resolution within the roll-up spiral is improved as expected with increasing I_κ. The effect of varying the maximal segment size h_{max} on vortex sheet roll-up is shown in figure 4. The vortex sheets are very close in the roll-up region with the exception of near the braid for different values of h_{max}. The results also demonstrate the influence of initial discretization on vortex roll-up since initially all segment sizes are approximately equal to h_{max}. Unlike the free-surface case in which the result converges with decreasing h_{max}, here reducing segment size means introducing modes with higher growing rates. Nevertheless, the global features of the roll-ups are the same with the same embedded initial perturbation.

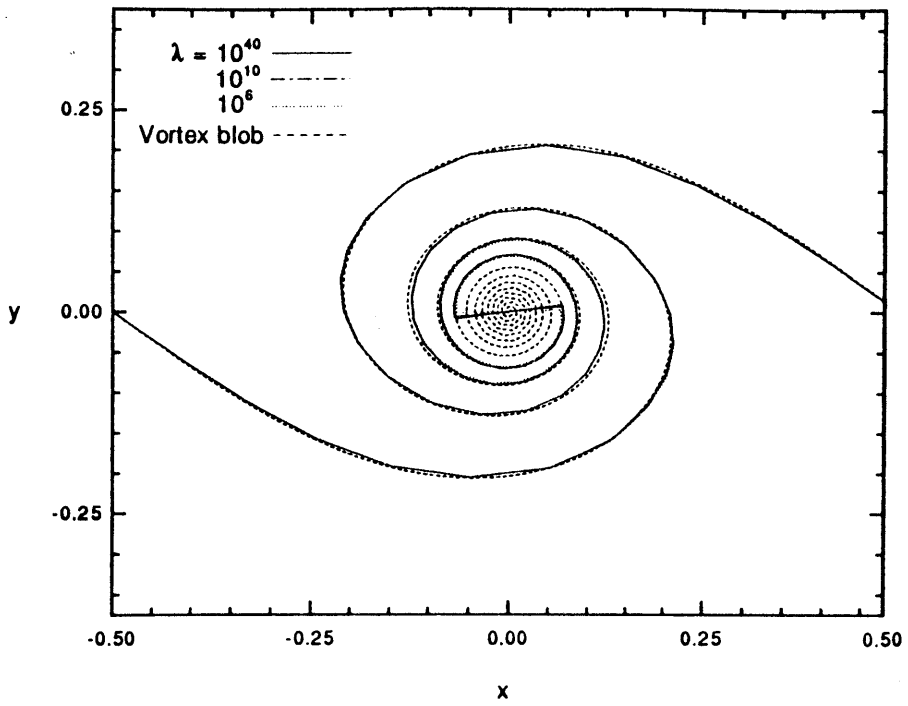

Figure 2. Double-branched spiral roll-up of periodic vortex sheet at $t = 2.0$ for different values of smoothing parameter: $\lambda = 10^6$ 10^{10} and 10^{40}; and by vortex blob method with radius of blob $\delta = 0.12$ and 500 vortex blobs.

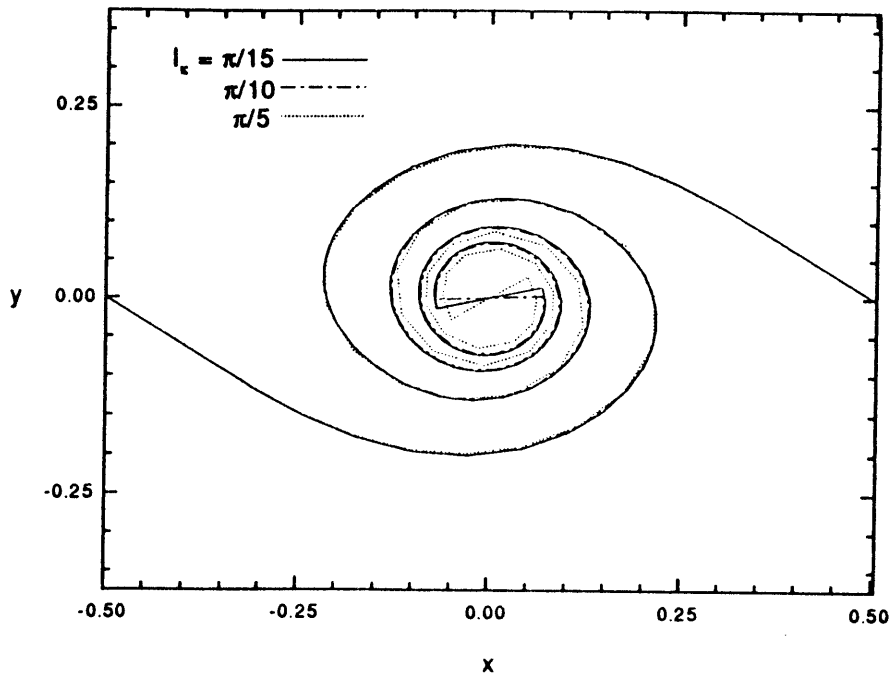

Figure 3. Double-branched spiral roll-up of periodic vortex sheet at $t = 2.0$ for different values of mesh-function increment: $I_\kappa = \pi/15$, $\pi/10$ and $\pi/5$.

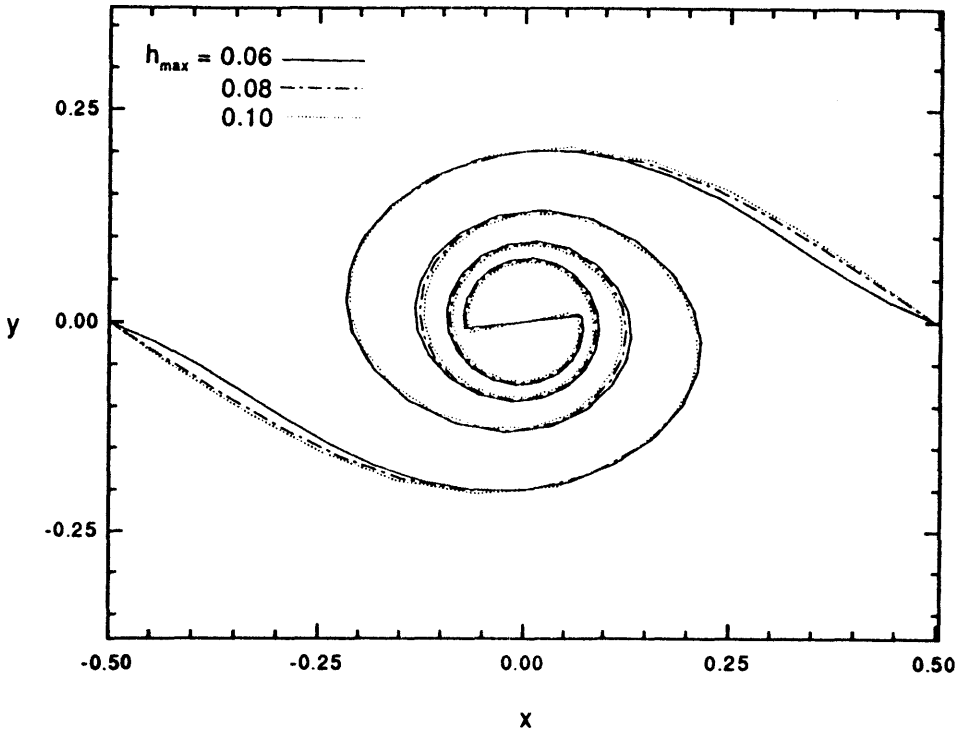

Figure 4. Double-branched spiral roll-up of periodic vortex sheet at $t = 2.0$ with different maximal segment size: $h_{max} = 0.1$, 0.08 and 0.06.

3.3. Amalgamation of single- and double-branched spirals

To eliminate the numerical difficulties in simulating the asymptotically tightened and infinitely wound spiral roll-up, the spiral (single- and double-branched) vortex sheet is approximated by a single core vortex bounded by a finite winding number vortex spiral (*e.g.*, Pullin & Phillips 1981; Hoeijmakers & Vaatstra 1983). For single-branched spiral roll-up the core vortex corresponds to the starting vortex shed at $t = 0$. As the vortex sheet continuously rolls up into a spiral and the winding angle exceeds the prescribed value, the excess portion of the shear layer is amalgamated into the core vortex. For double-branched roll-up, which results from steepening of circulation distribution along the shear layer, amalgamation starts whenever the inner spiral's roll up exceeds the given winding turns. The amalgamation forms a core vortex which approximates the steep circulation distribution by a step function. The strength and position of the amalgamated vortex are determined according to the conservation of circulation and linear moment of vorticity. Figure 5 shows single-branched spirals with different cut-off winding angles $\theta = \pi$, 2π, and 3π, for the roll-up of vortex sheet shed by a steadily moving plate with $\pi/2$ angle of attack. Double-branched spiral roll-up of a periodic vortex sheet with various cut-off winding angles $\theta = \pi$, 2π, and 3π for one branch are shown in figure 6. Application of amalgamation is found to have only negligible effects on the motions outside the outermost turn of both single- and double-branched spirals.

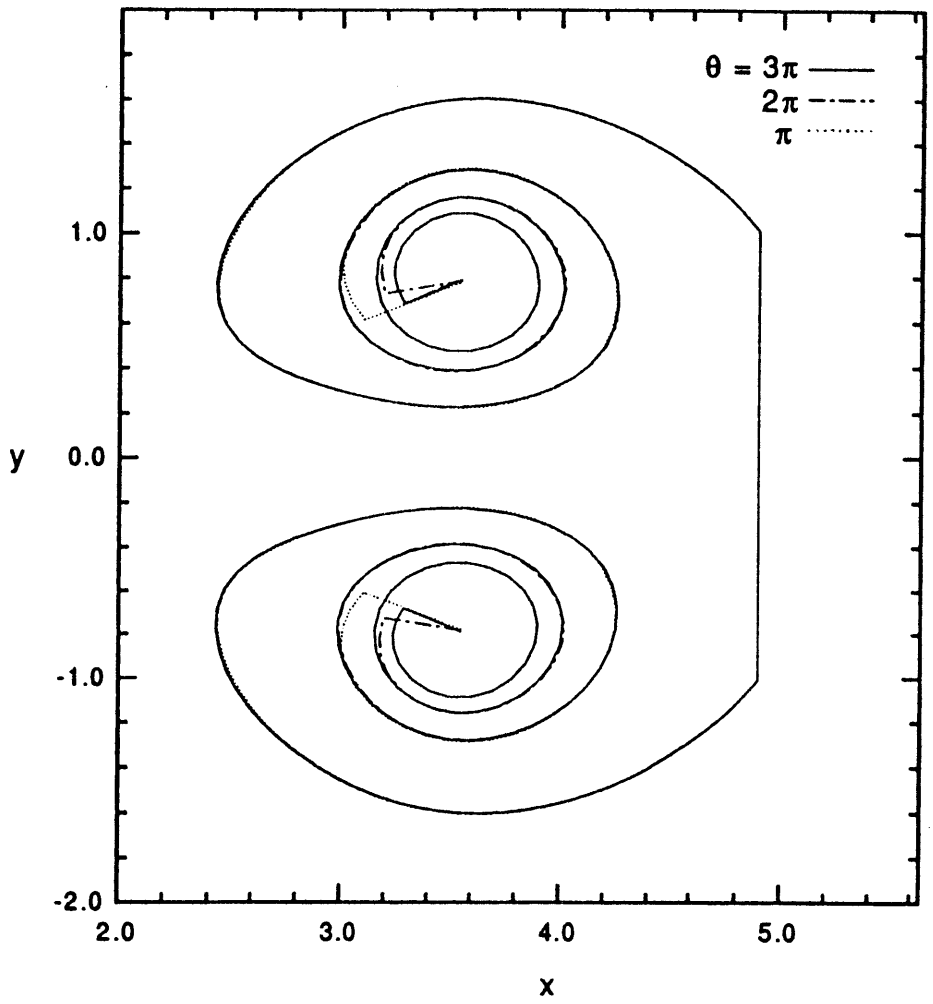

Figure 5. Single-branched spiral roll-up at $t = 5.0$ shed by a steadily moving plate in infinite flow with different cut-off winding angle of amalgamation: $\theta = \pi$, 2π and 3π.

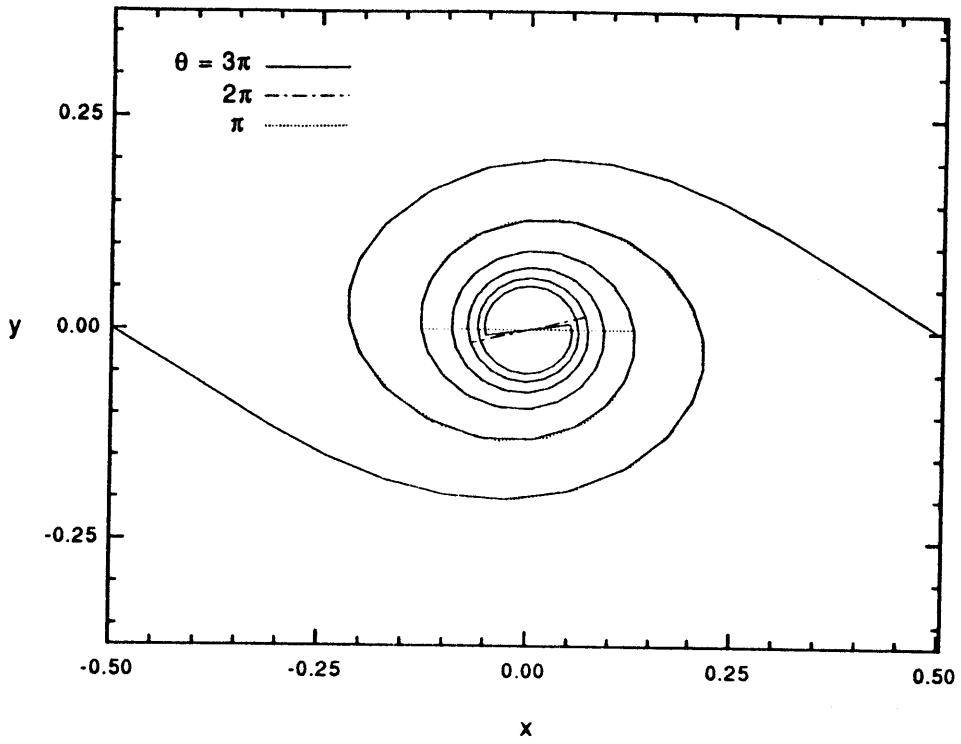

Figure 6. Double-branched spiral roll-up of periodic vortex sheet at $t = 2.0$ with various cut-off winding angle of amalgamation: $\theta = \pi$, 2π and 3π.

3.4. Accuracy of numerical time integration

As shown in Dommermuth *et al.* (1988), the explicit fourth-order Runge-Kutta time integration for linearized free surface boundary conditions is conditionally stable and mildly dissipative. The Courant condition for the stability of the Runge-Kutta method is: $\triangle t^2 \leq 8Fn^2\triangle x/\pi$, where $\triangle t$ is the time step of integration and $\triangle x$ is the segment size on the free surface. For the computations of our final simulation, the typical minimal free-surface segment is 0.01 and the time step used is 0.005 which is much less than required by the Courant condition.

The accuracy and convergence of the time-stepping procedure for vortex sheet tracing and shedding at the separation point are checked by systematically reducing the time step of the Runge-Kutta scheme for the calculations of spiral roll-up shed by the plate in infinite flow. The vortex tracing results of the spiral roll-up at $t = 4.0$ with different integrating time steps ($\triangle t = 0.04$, 0.02, 0.01 and 0.008) are shown in figure 7. The results show convergence of our vortex shedding and tracing scheme with reducing time integration step.

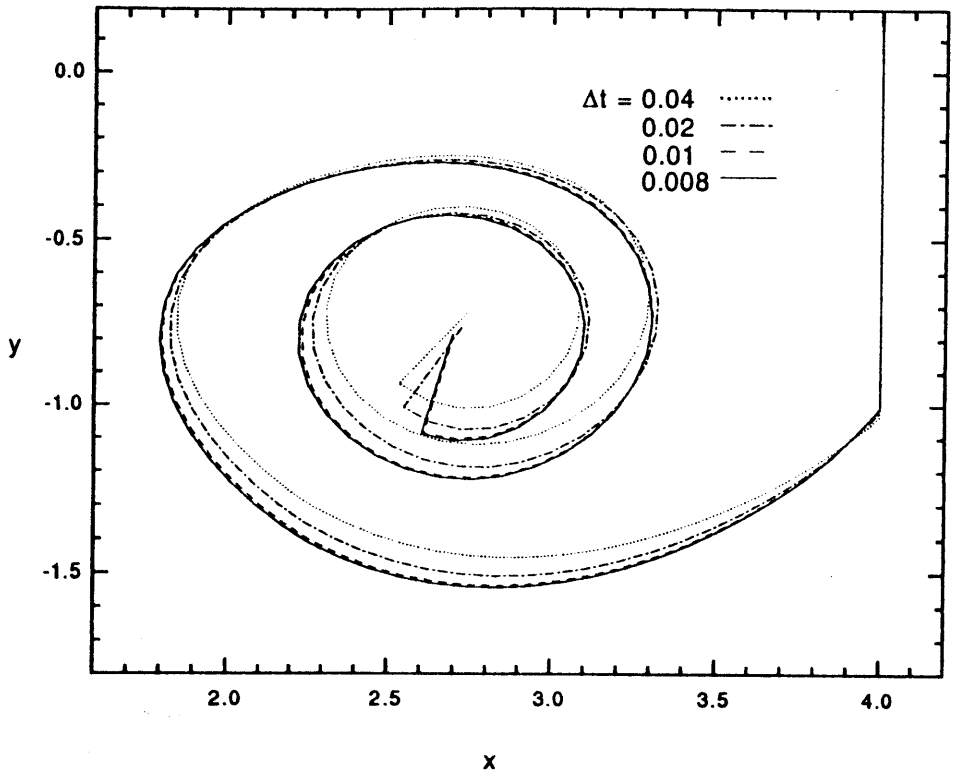

Figure 7. Single-branched spiral roll-up at $t = 4.0$ shed by a plate in infinite flow with different integrating time steps: $\triangle t = 0.04$, 0.02, 0.01 and 0.008.

3.5. Effects of grid spacing on the plate

The discretization of the plate segment affects both the motions of the intersection points and vortex shedding at the separation point. Careful studies were carried out by Lin (1984) regarding the grid spacing near the intersection point. It was concluded from the numerical experiments that the sizes of the segments at the intersection point corner should be comparable, and a denser grid spacing near the intersection results in very high thin jet shoot-up but little effect on the global free-surface motion.

The grid spacing near the separation point, however, affects not only the vortex shedding but also the later motions since the vortex sheet is convected from the separation point. Effects with respect to grid spacing near the separation point are tested by using both cosine and uniform spacing with different segment sizes as shown in figure 8 for a shed single-branched spiral at $t = 4.0$. The uniform spacing is arranged such that finer segments (h_{sep}=1/40 and 1/60) are distributed within a quarter length of the half plate from the separation point, and the rest of the plate is discretized with uniform segments size h=1/28. Two cosine spacing grids with total segment number N_{seg}=40, and 48 are also shown in figure 8. The segment size next to the separation point is approximately equal 0.002 for the finer cosine spacing which is much smaller than the 0.025 segment size uniform spacing. The results show virtually indistinguishable profiles for cosine spacing shedding. Whereas the uniform spacing shedding converges quickly with finer gridding to cosine spacing results. For the surface-piercing plate, whose submergence (plate length) changes with time, we therefore use uniform spacing along the plate with fixed and finer discretization near the separation point and uniformly rediscretize the rest of plate at each time step.

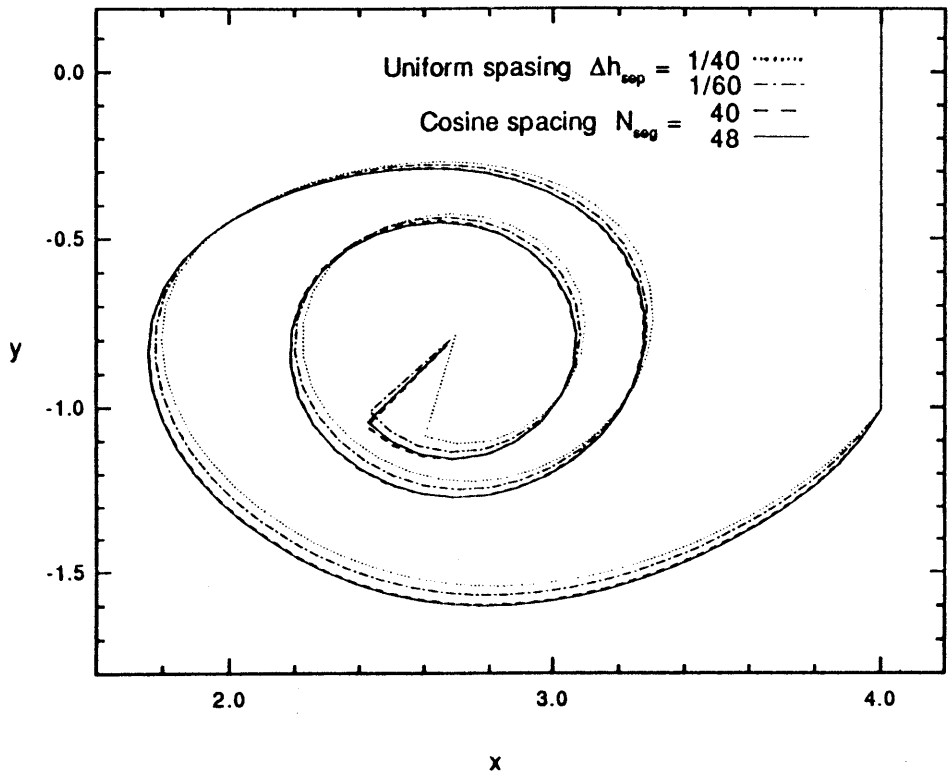

Figure 8. Single-branched spiral roll-up at $t = 4.0$ shed by a steadily moving plate in infinite flow with various uniform and cosine spacing segments on the plate.

4. Computational results

4.1 Critical Froude number for surface/vortex interactions

We perform a complete study of the free surface and shed vortex sheet interaction problem by systematically varying the Froude number F_n over the entire range of interest. From our numerical simulations, three qualitatively different classes of interactions can be identified, depending on F_n, as subcritical ($F_n <\sim 0.7$), transcritical ($F_n \sim 0.7 - 1.0$), and supercritical ($F_n >\sim 1.0$). The characteristic features for the three classes of interaction dynamics within the near wake of the plate are:

- *Subcritical interaction.* Free surface breaks before significant interaction with the starting single-branched spiral vortex happens.
- *Transcritical interaction.* Backwards propagating free-surface setdown pushes backwards the single-branched spiral and stretches the vortex sheet. The stretched vortex sheet rolls up into series of double-branched spirals without significant interaction with the free surface.
- *Supercritical interaction.* In contrast to the transcritical case, the double-branched spirals form near the free surface and cause large free-surface deformation.

Two global conditions which may affect the interaction features are: the length between up- and downstream periodic boundaries, and the initial motion of the plate. In §*4.3* the effect of periodic boundaries is studied by changing the length of computational domain. The possible effect of the impulsive start of plate motion is studied in §*4.4* by using a smooth startup motion as initial condition. It is concluded that these two boundary and initial conditions do not change the characteristic features of the interaction dynamics.

For all of the computational results shown in the following, we choose the time step of the Runge-Kutta time integration $\Delta t = 0.005$ and the length between pe-

riodic boundaries $\ell = 10$. The discretization on the plate is uniform spacing with fixed segment size $\Delta h_{sep} = 1/60$ on the portion within one tenth of the initial submergence (=1) from the separation point, and with segment size Δh approximately equal to 0.04 for the rest of the plate which is uniformly rediscretized at every time step. Adaptive rediscretization is applied to the free surface every five time steps with the parameters chosen as $\lambda = 10^8$, $I_\kappa = \pi/10$, $h_{max} = 0.06$, $h_{min} = 0.01$, and is applied to the vortex sheet every time step with $\lambda = 10^8$, $I_\kappa = \pi/11$, $h_{max} = 0.06$, $h_{min} = 0.008$. In all of our computations, the total energy and the fluid volume are monitored to ensure the accuracy of the computations. For all the results shown below, the total energy (compared to work done) is conserved to within 4%, and the fluid volume to at least 3 decimal places.

4.1.1. Subcritical Froude number

Figures 9 and 10 show representative evolutions of subcritical Froude number motions ($F_n <\sim 0.7$) at $F_n = 0.5$ and 0.6. At the early stage, a vortex sheet is shed from the separation point which quickly rolls up into a single-branched spiral. Due to the impulsive motion of the plate, the free surface on the forward side of the plate shoots up rapidly in the form of a thin jet. Difficulties associated with simulating a very thin film on the forward face are avoided by cutting that portion of the film whose thickness is less than a small fraction (we use 2%) of the local segment length, and a new intersection point is specified. In contrast, the intersection point on the lee side is drawn down and meets the plate at a finite contact angle.

As time proceeds, the single-branched spiral grows in size and the vortex sheet continuously rolls into the spiral center. A free surface disturbance propagates away from the forward face of the plate eventually forming a plunging breaker. On the lee side of the plate, a smaller backward propagating wave front is formed near the plate which ultimately also breaks. Consistent with and similar to the infinite fluid ($F_n = 0, e.g.,$ figure 5) case, the single-branched spiral remains attached to the plate. The center of roll-up, however, becomes shallower as it grows, resulting in a small deformation of the free surface. The free-surface and vortex sheet evolutions for this range of Froude numbers are thus characterized by negligible to weak interactions between the two.

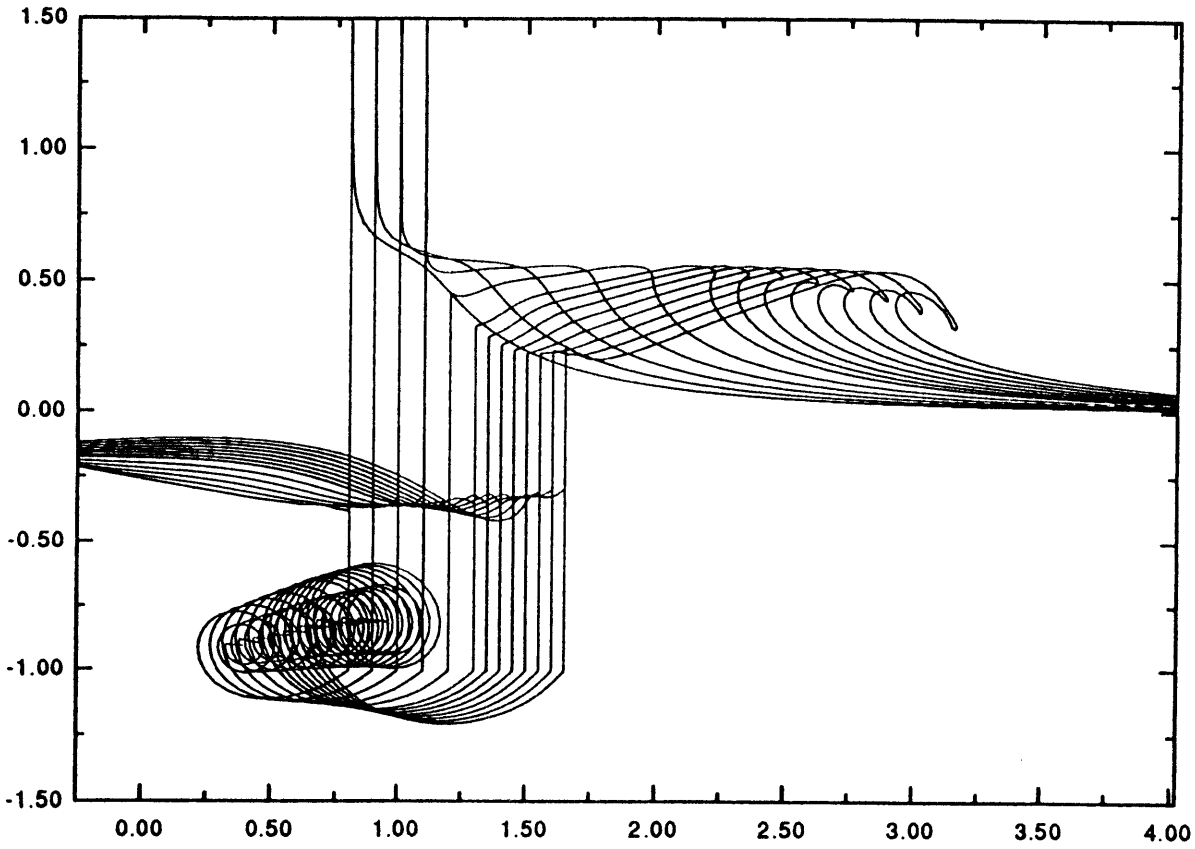

Figure 9. Evolution of the free surface and vortex sheet for subcritical Froude number $F_n = 0.5$.

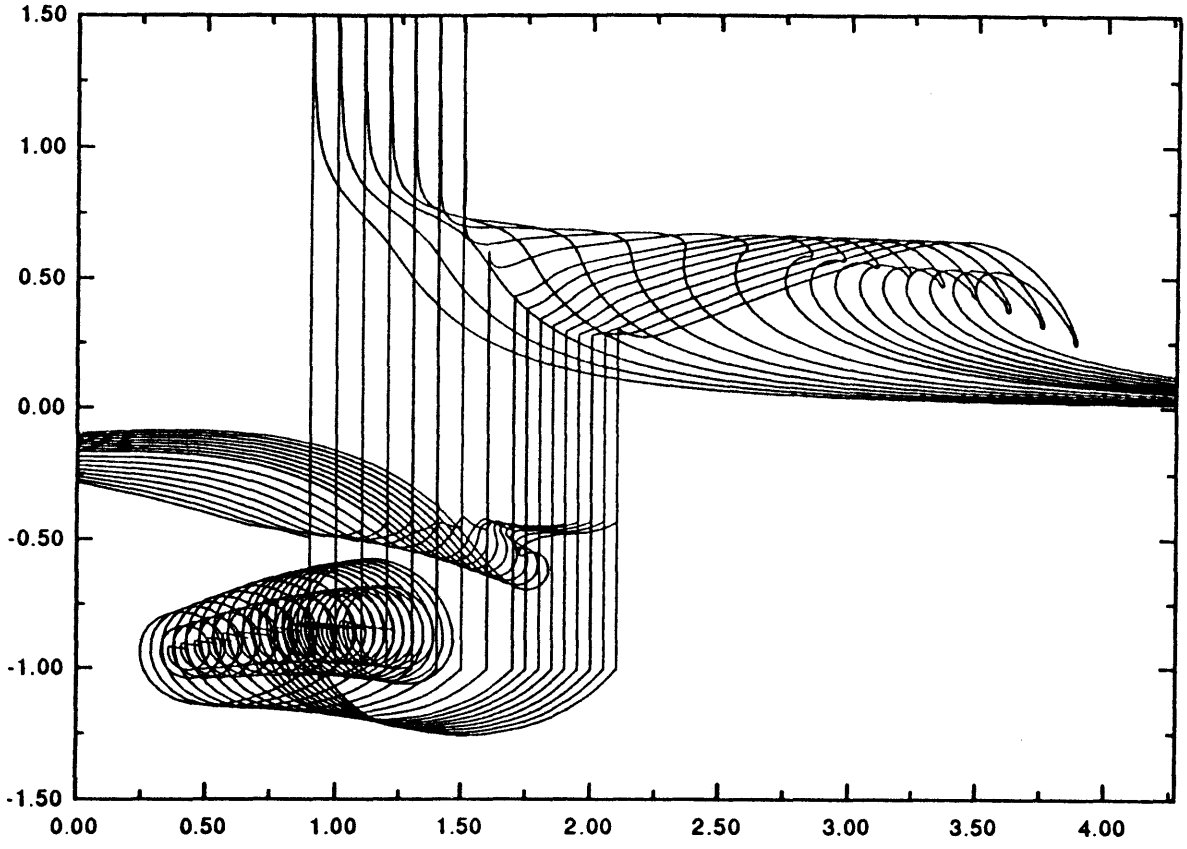

Figure 10. Evolution of the free surface and vortex sheet for subcritical Froude number $F_n = 0.6$.

4.1.2. Transcritical Froude number

The early stages of the free surface and vortex sheet evolutions are similar for the three classes. While for transcritical and supercritical Froude number ($F_n >\sim 0.7$), different but significant interactions are observed after the single-branched spiral fully develops. Figures 11, 13 and 15 show the evolution of the free surface and vortex sheet for $F_n = 0.7$, 0.8 and 1.0 respectively, illustrating the transcritical interaction mechanisms. Details of the vortex sheet motions in the wake of the plate at various time instances are also shown in figures 12, 14 and 16. The depression of the free surface on the lee side of the plate pushes the single-branched vortex spiral downstream causing the vortex sheet to stretch between the single-branched roll-up and the separation point. At this stage, the rate of vortex shedding at the separation point decreases to a small value (figure 23) and finite-amplitude Kelvin-Helmholtz instabilities develop on the stretched portion of the vortex sheet. As time proceeds, these instabilities grow and roll up into double-branched spirals as shown in figure 12 at $t > 2.45$ for $F_n = 0.7$, figure 14 at $t > 1.9$ for $F_n = 0.8$, and figure 16 at $t > 1.8$ for $F_n = 1.0$.

The incidence of Kelvin-Helmholtz instabilities is demonstrated for the $F_n = 0.9$ case in figure 17 which plots the velocity fields in the wake of the plate at $t = 0.9$, 1.7, 2.1 and 2.2. At the initial stage, $t = 0.9$, the wake flow is mainly influenced by the rolled-up starting vortex which has developed to a considerable size. As the large free-surface depression associated with the plate starting motion propagates backward, it prevents the vortex spiral from rising and pushes it further downstream creating a stretched flat vortex sheet between the separation point and the rolled-up spiral ($t = 1.7$). Due to flows in opposite directions on the upper and lower sides of the stretched vortex sheet, a strong shear strain develops which amplifies the initial growth of instabilities on the stretched vortex sheet. These instabilities then quickly roll up into double-branched spirals starting from the portion of shear layer near the single-branched spiral (t= 2.1 and 2.2).

The main difference between the transcritical and supercritical cases is in the strength of the interactions between the free surface waves and the Kelvin-Helmholtz instabilities on the vortex sheet. For transcritical Froude numbers, the double-branched spirals form well below the free surface. The interactions between the free-surface and Kelvin-Helmholtz waves are consequently weak and allow the instabilities on the stretched vortex sheet to roll up continuously, forming a series of double-branched spirals. For substantially higher Froude numbers in transcritical range, as *e.g*, $F_n = 1.0$, $t = 2.15$ in figure 16, the double-branched spirals begin interacting with each other and may eventually merge into a single vortex spiral.

The free-surface depression behind the plate continues to develop, the backward facing surface steepens and eventually plunges backward. The intersection point on the lee side of the plate moves downward with time, reaching a constant depth asymptotically (see figure 20).

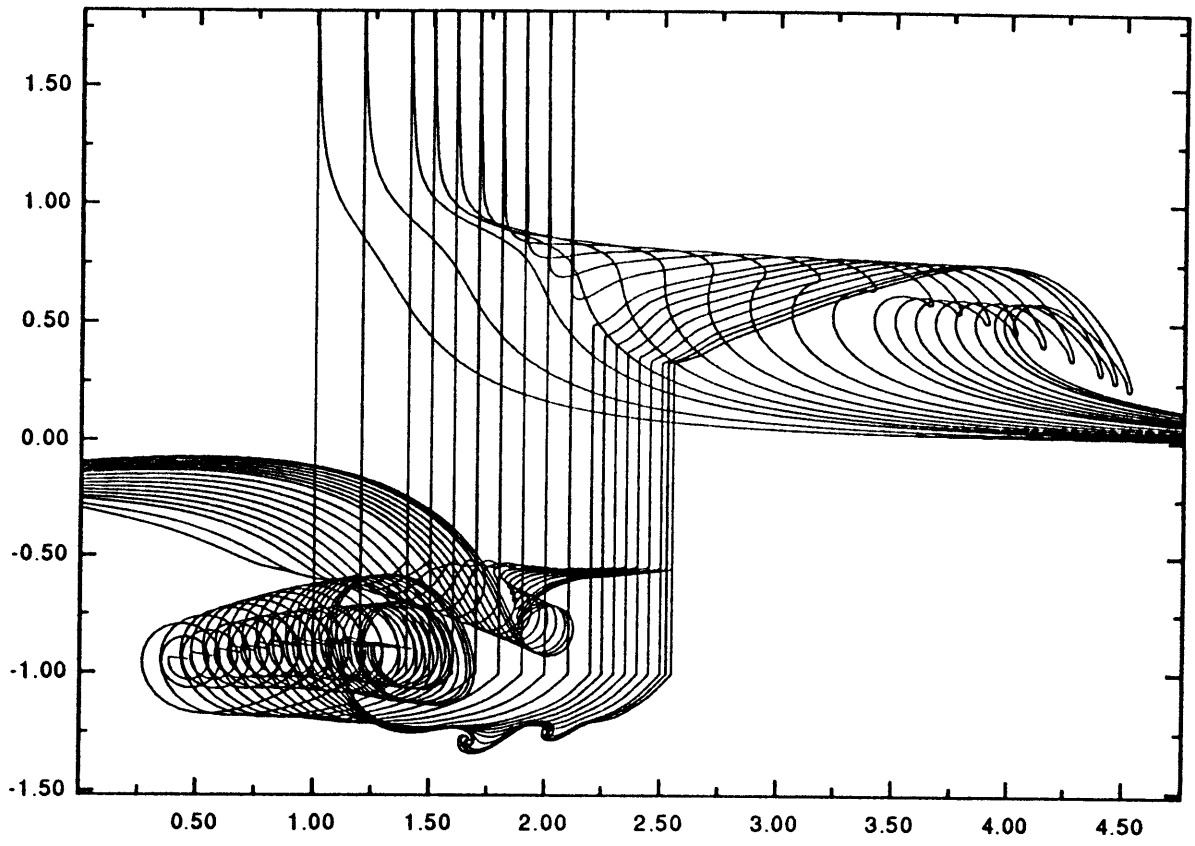

Figure 11. Evolution of the free surface and vortex sheet for transcritical Froude number $F_n = 0.7$.

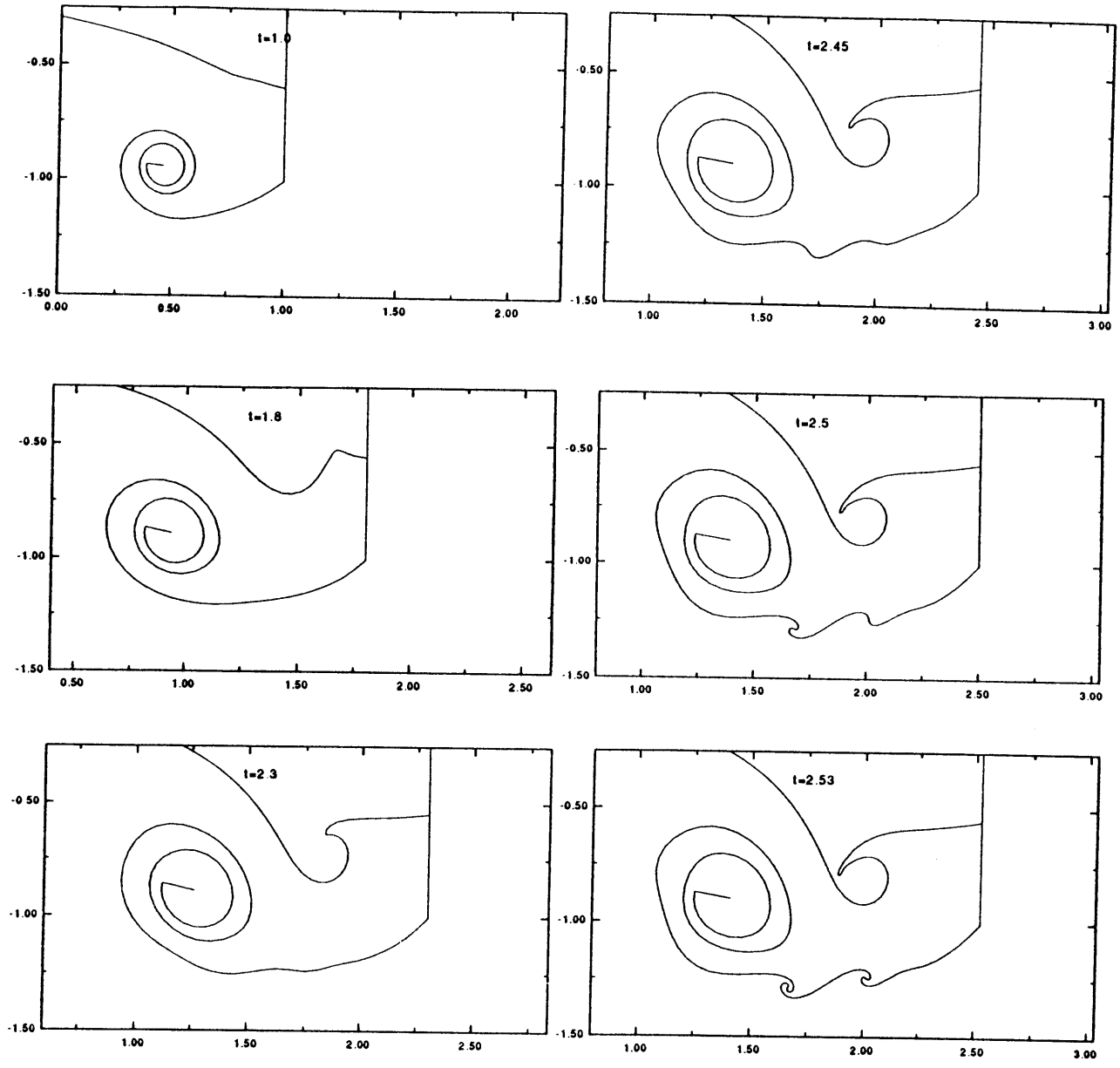

Figure 12. Evolution of the free surface and vortex sheet in the wake of plate for $F_n = 0.7$ at $t = 1.0$, 1.8, 2.3, 2.45, 2.5 and 2.53.

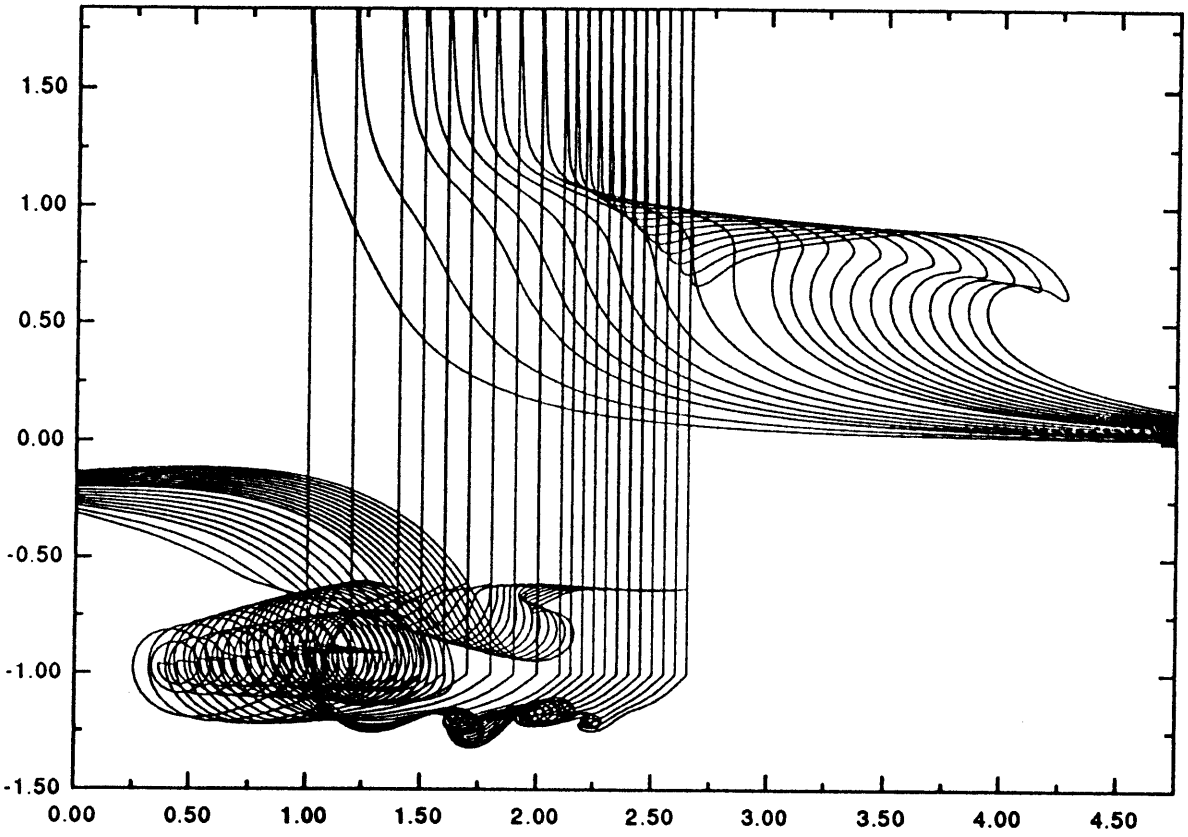

Figure 13. Evolution of the free surface and vortex sheet for transcritical Froude number $F_n = 0.8$.

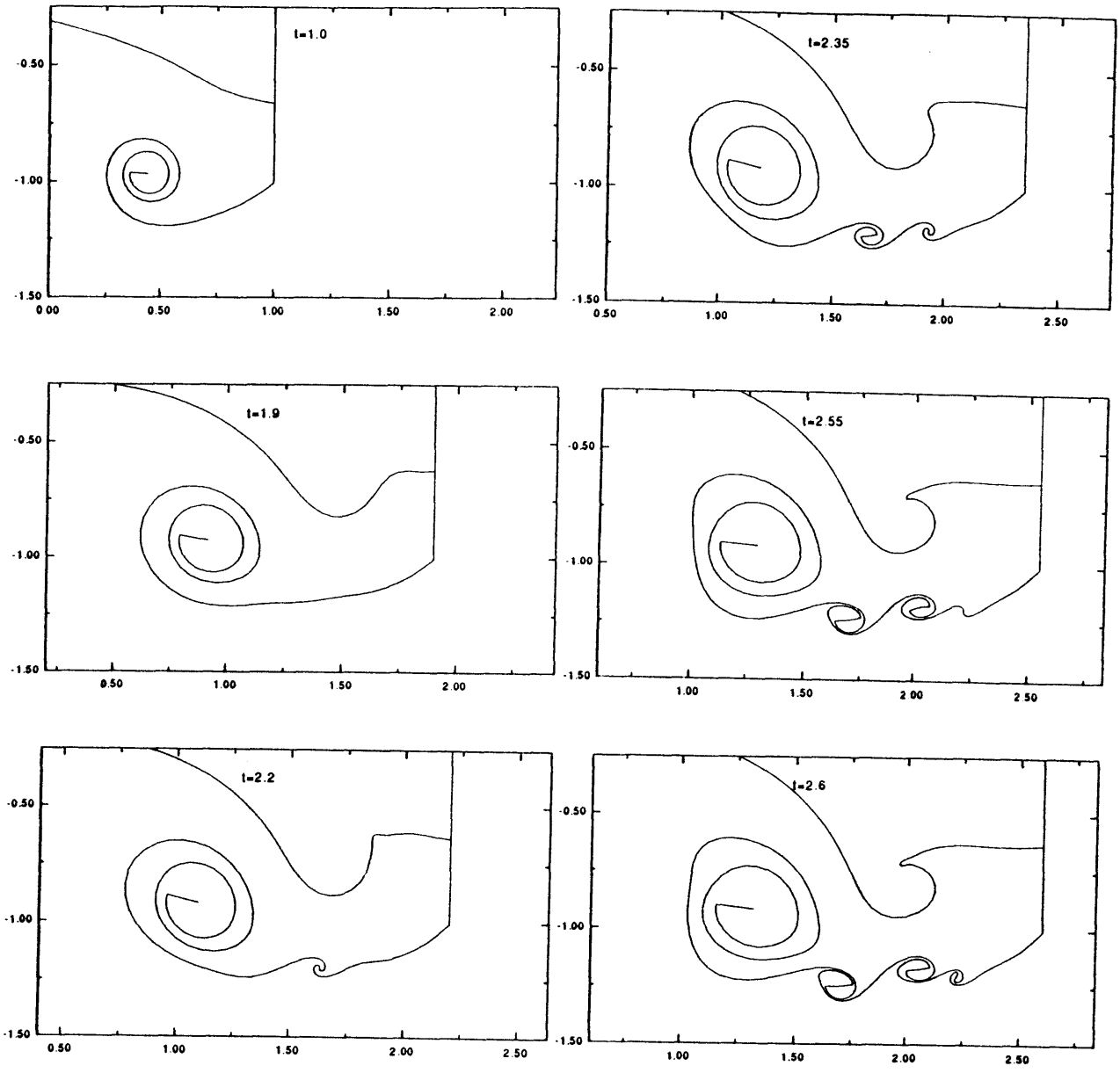

Figure 14. Evolution of the free surface and vortex sheet in the wake of plate for $F_n = 0.8$ at $t = 1.0$, 1.9, 2.2, 2.35, 2.55 and 2.6.

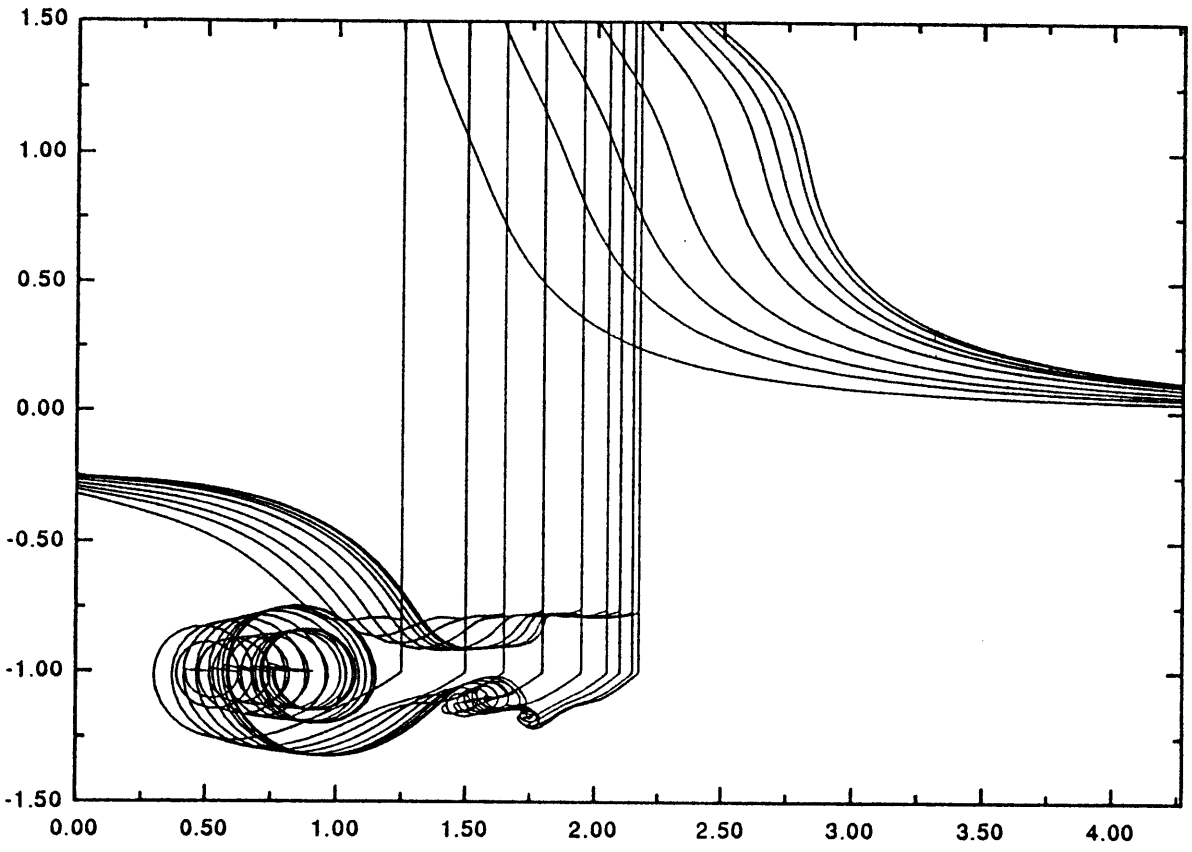

Figure 15. Evolution of the free surface and vortex sheet for transcritical Froude number $F_n = 1.0$.

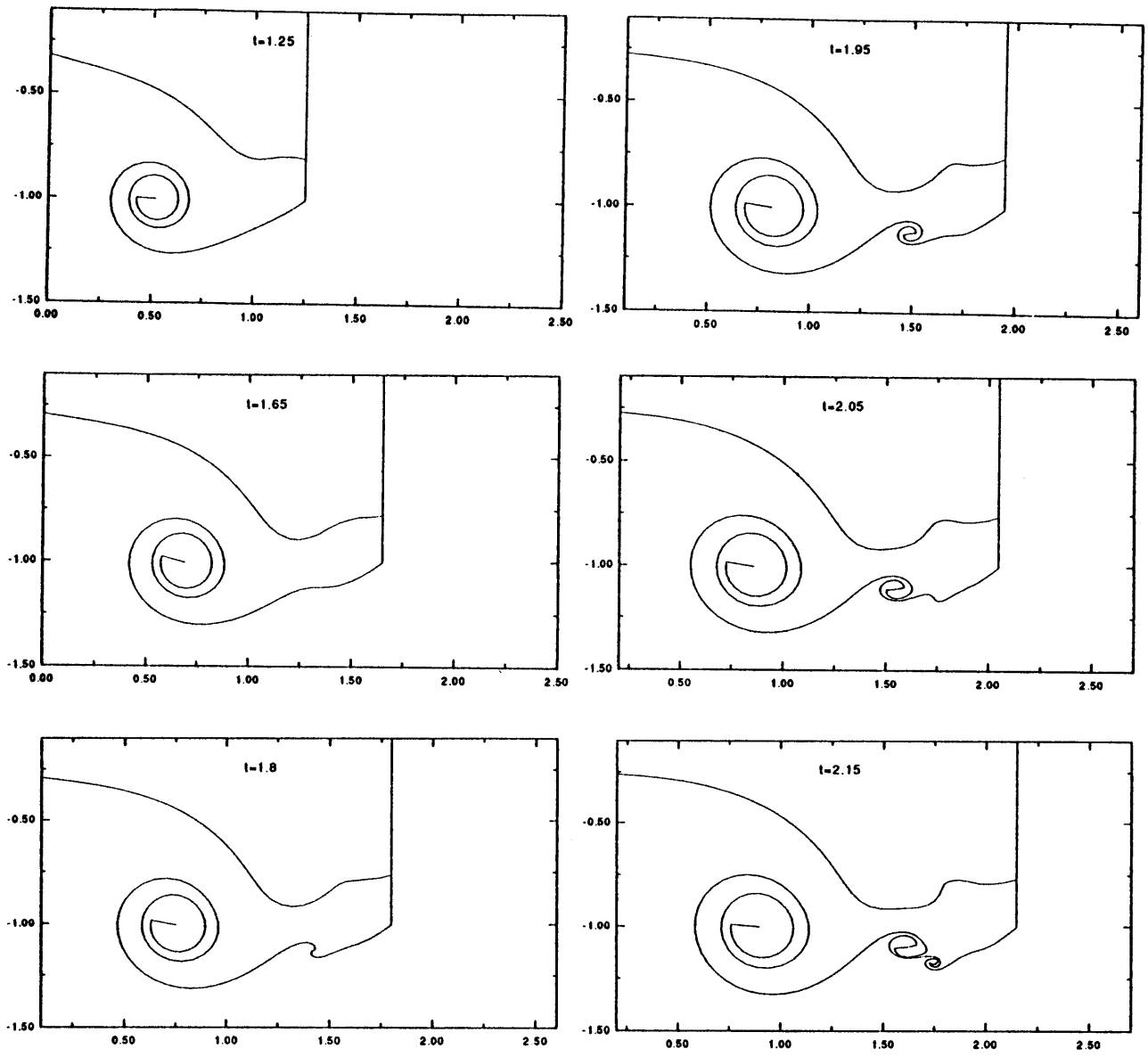

Figure 16. Evolution of the free surface and vortex sheet in the wake of plate for $F_n = 1.0$ at $t = 1.25$, 1.65, 1.8, 1.95, 2.05 and 2.15

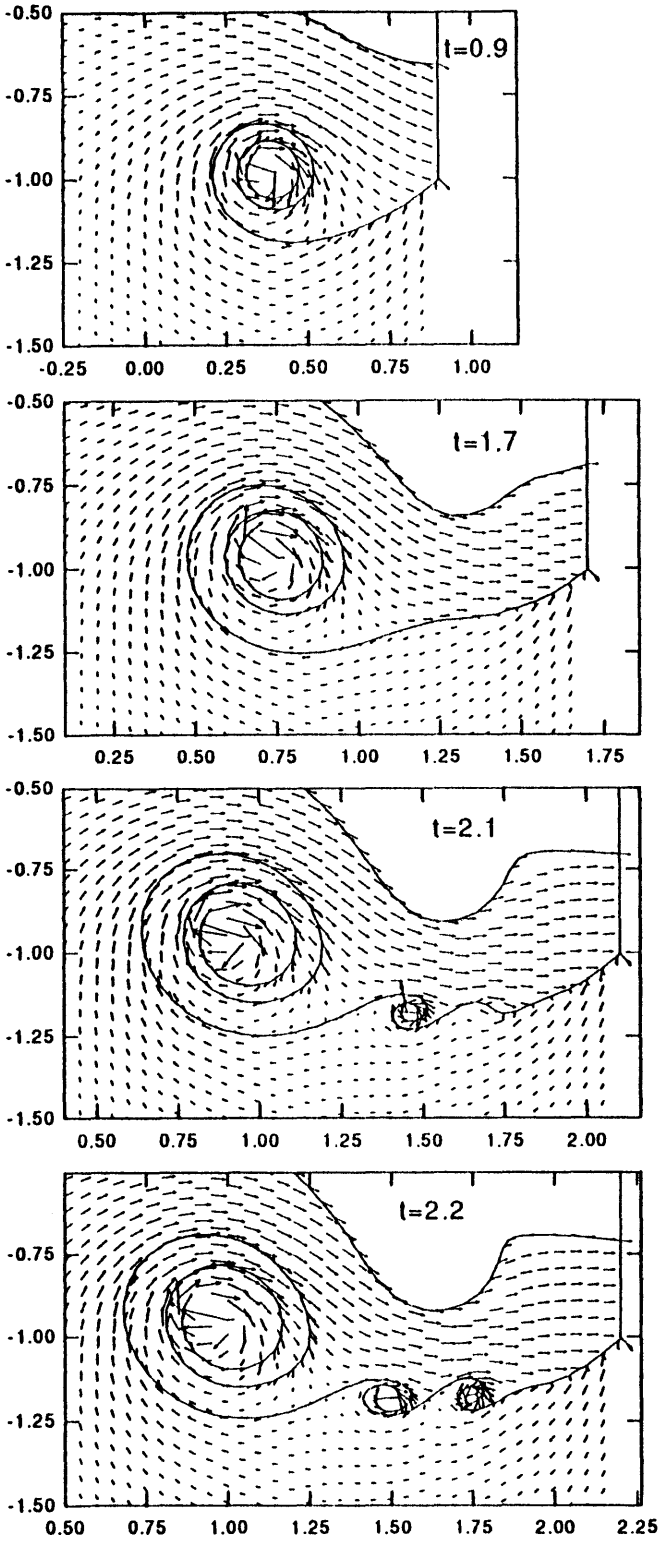

Figure 17. Velocity field in the wake of plate for $F_n = 0.9$ at $t = 0.9$, 1.7, 2.1 and 2.2.

4.1.3. Supercritical Froude number

The features of the free surface/vortex interactions at later stage for the supercritical Froude number are quite different from those of the transcritical case, as shown in figures 15 and 16 for $F_n = 1.2$ and 1.5 respectively. As in the transcritical Froude number cases, the initial and quick free-surface set-down in the wake of the plate pushes the single-branched spiral downward and forms a stretched, unstable vortex sheet. As the Kelvin-Helmholtz instability grows, a single double-branched spiral forms on the perturbed, stretched vortex sheet beneath the sloping side of the depressed free surface. Unlike the transcritical cases, such a solitary double-branched spiral in the supercritical Froude number class grows in size and approaches and eventually becomes entrained into the free surface. The free-surface deformation is strongly affected by the rising double-branched spiral, developing a sharp depression between the single- and double-branched spirals.

In these cases, the movement of the plate almost follows the propagation of the free surface disturbance on the front side of the plate. The free surface jet is pushed forward and keeps rising in the range of computation. The lower intersection point on the lee side of the plate moves downward continuously (figure 20) and the free surface eventually sluices from the lower tip of the plate.

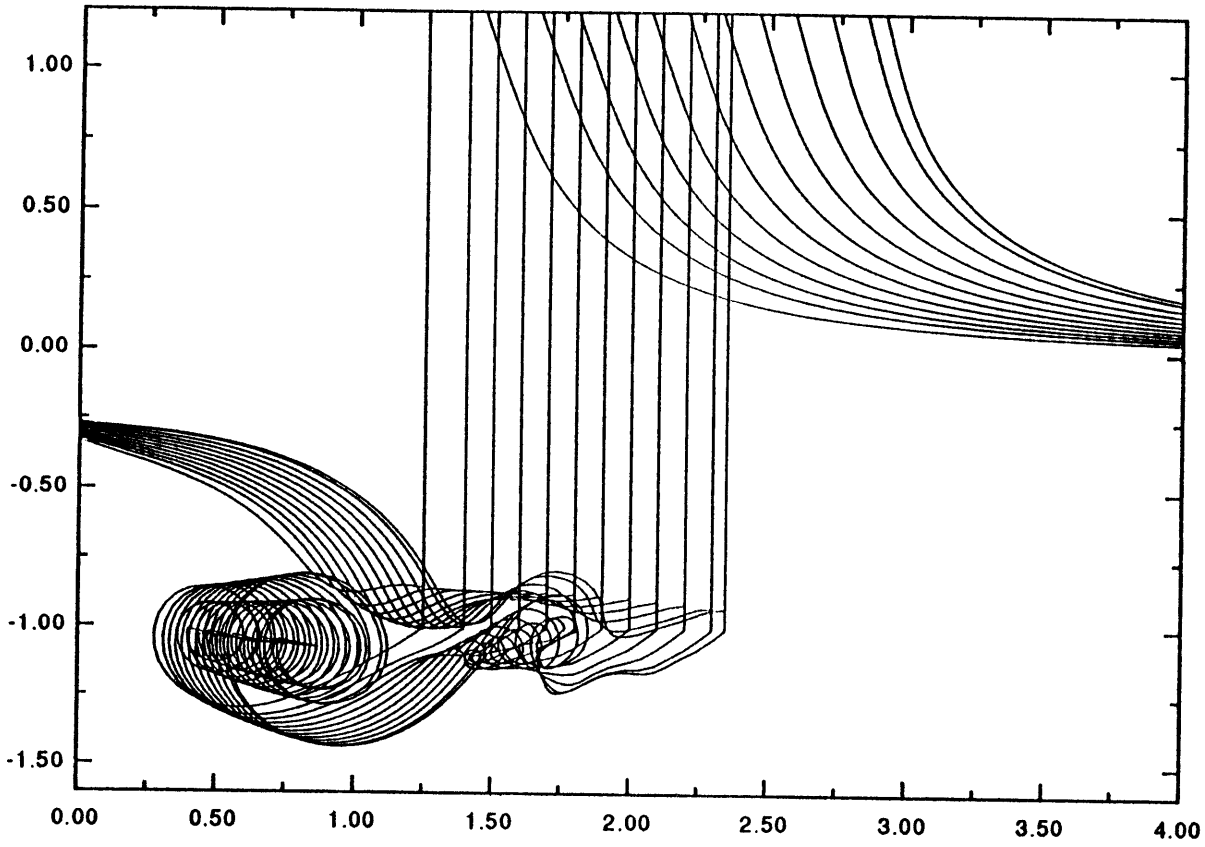

Figure 18. Evolution of the free surface and vortex sheet for supercritical Froude number $F_n = 1.2$.

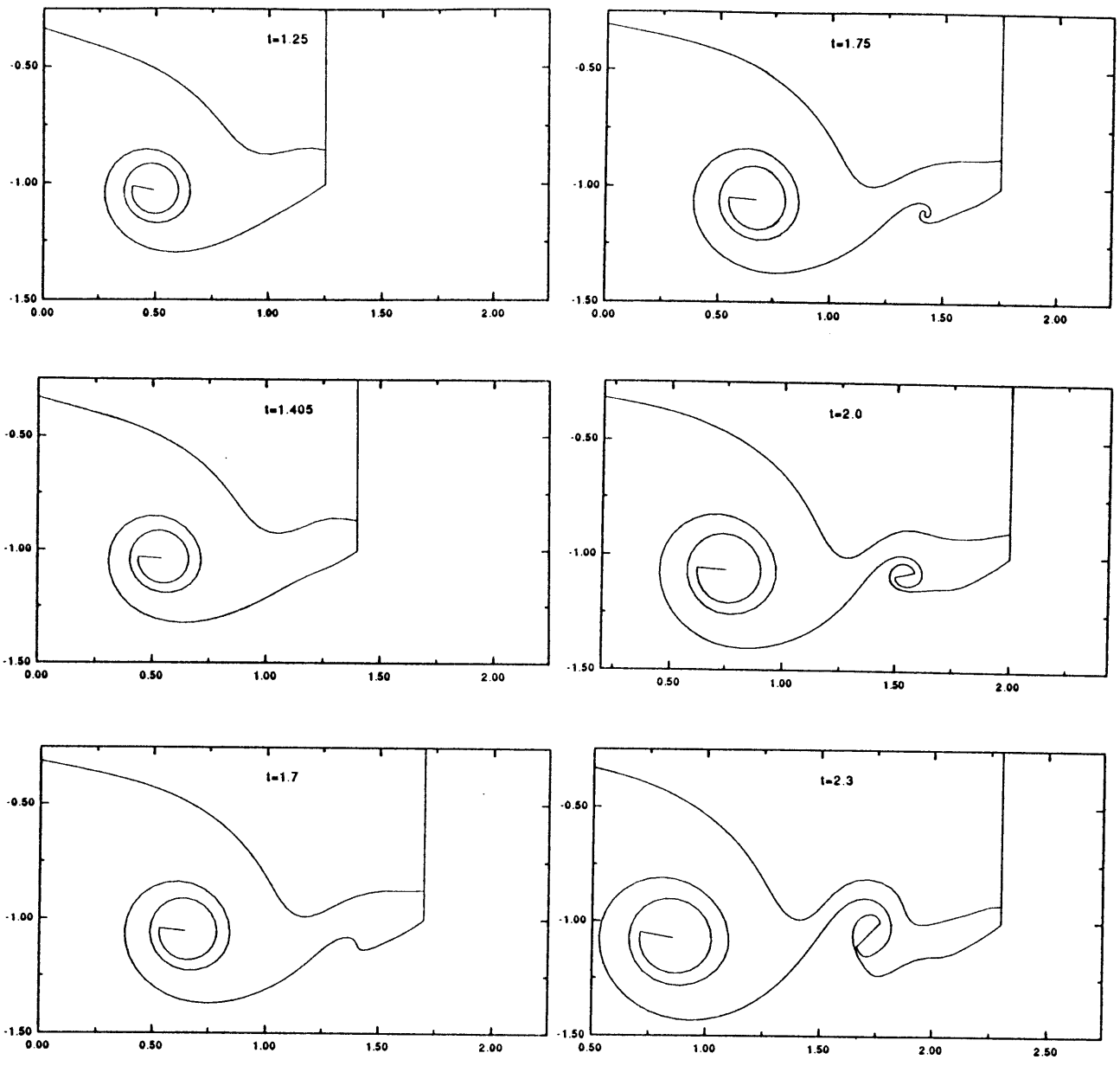

Figure 19. Evolution of the free surface and vortex sheet in the wake of plate for $F_n = 1.2$ at $t = 1.25$, 1.405, 1.7, 1.75, 2.0 and 2.3.

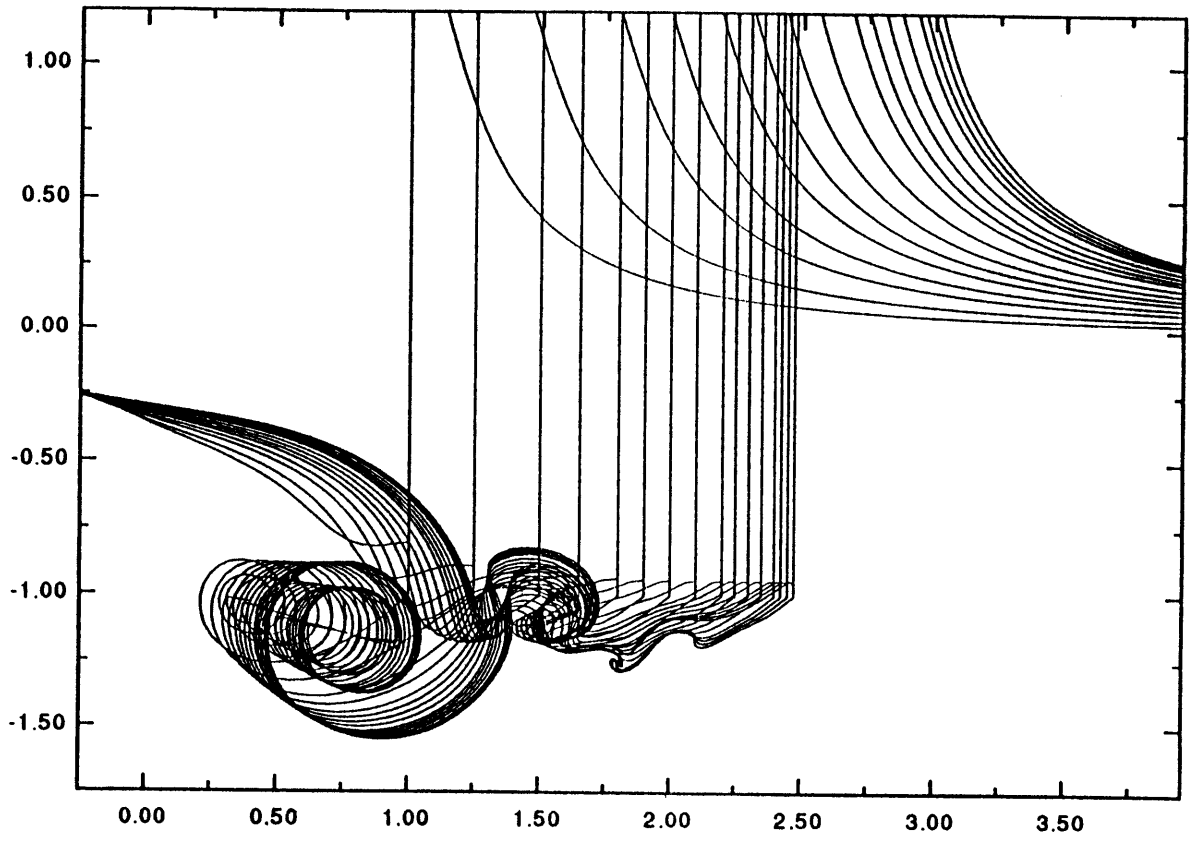

Figure 20. Evolution of the free surface and vortex sheet for supercritical Froude number $F_n = 1.5$.

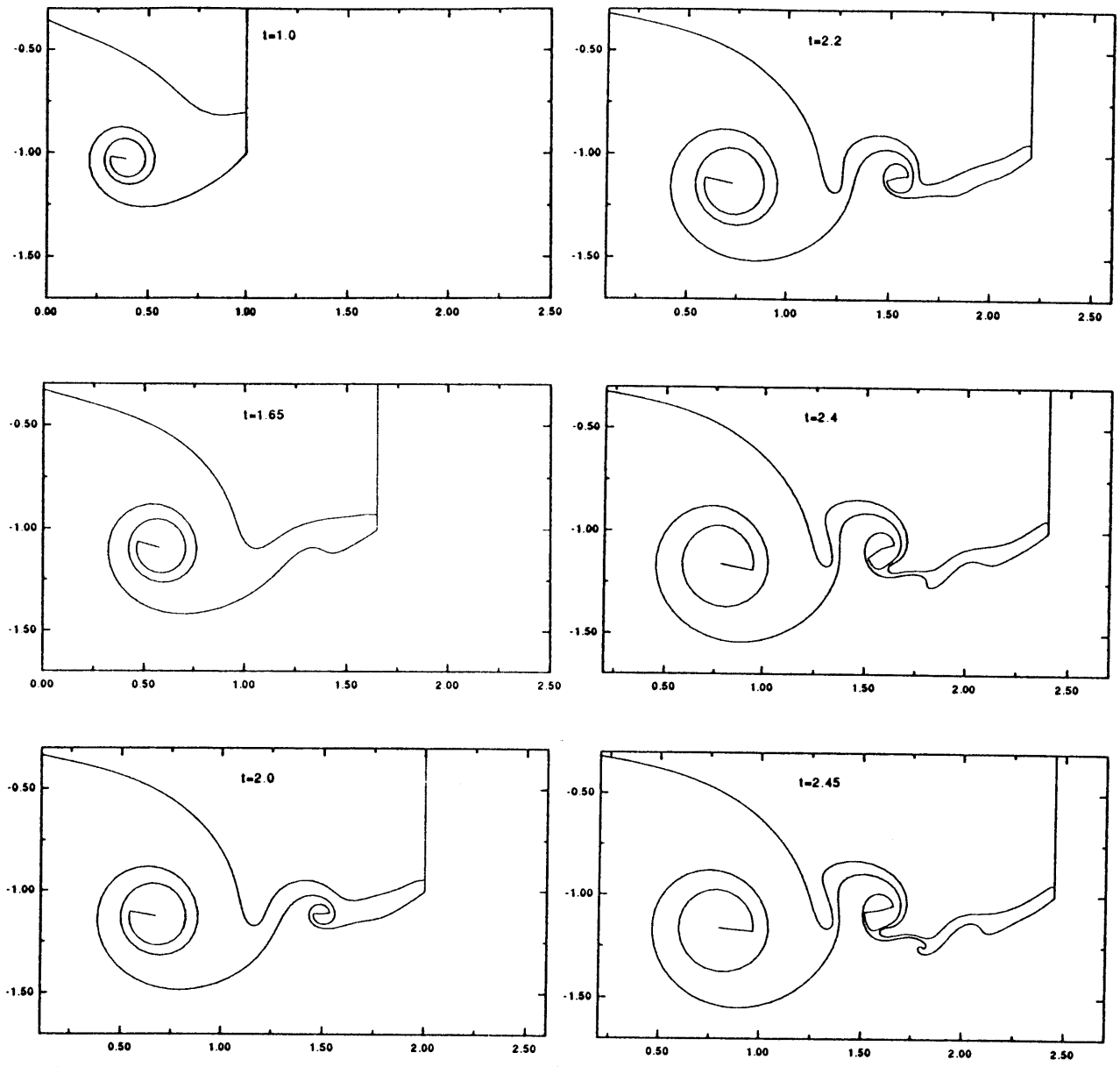

Figure 21. Evolution of the free surface and vortex sheet in the wake of plate for $F_n = 1.5$ at $t = 1.0$, 1.65, 2.0, 2.2, 2.4 and 2.45.

4.2. Time evolution of characteristic properties

It is instructive to compare the time evolution of some physical properties which characterize the Froude number dependence of interaction features. We first show the properties of vortex shedding at the separation point for various Froude numbers. Figures 22 and 23 show time evolution of the circulation $[\phi]_{sep}$ and the rate of vortex shedding $\mathrm{d}[\phi]_{sep}/\mathrm{d}t$ at the separation point. Unlike the vortex shedding in infinite flow which increase monoclinically at later stages, for finite Froude number cases the rates of shedding decrease after a certain time.

To demonstrate the free surface effects on the motions of single-branched spirals, in figure 24 we plot the paths of spiral centers: $(x_{sc}-t)$ versus y_{sc}. As indicated above, for subcritical Froude number cases the spiral approaches the free surface as it grows. The backward movement of the vortex is due to the growth of roll-up but not the free surface motion. As Froude number increases, the free surface depression in the wake begins washing the spiral downstream which causes stretching of the shear layer between roll-up and separation point. For supercritical Froude numbers ($F_n = 1.1 - 1.5$), the free surface even pushes the single-branched spiral deeper beneath the free surface while stretching the vortex sheet.

The vertical movement of the lower intersection point ($C_f \cap C_p \cap C_s$) with time is shown in figure 25 where the vertical position y_{li} versus time t is plotted. For both the subcritical and transcritical Froude number cases ($F_n \sim< 1.0$), the lower intersection point moves downward first and then oscillates. While for the supercritical Froude number class, the intersection points move downward continuously which eventually causes sluicing.

The energy evolutions of fluid system (E) can be calculated according to (2.10) and are shown in figure 26. Also plotted in the figure is the kinetic energy component due to the vortex sheet (E^v). The total energy increases in time for all Froude numbers since the motion of the plate keeps putting energy into the fluids. Nevertheless, the kinetic energy of the vortex sheet increases faster for the sub-

critical Froude number ($F_n = 0.5, 0.6, 0.7$) than for those in the transcritical and supercritical range.

The history of unsteady horizontal force acting on the plate (F_x), which equals the rate of work input or equivalently the rate of total energy change, is plotted in figure 27. Time evolution of the force component due to the vortex sheet (F_x^v) is also shown in figure 28. Interestingly, for subcritical Froude number, the total force first increases with time and then decreases rapidly. In the time when the total force decreases the component due to the vortex sheet increases rapidly, and contributes to most of the total force. For the transcritical and supercritical cases, the total force variation is more gradual. At later stage, the force due to the vortex sheet decreases to a small amount.

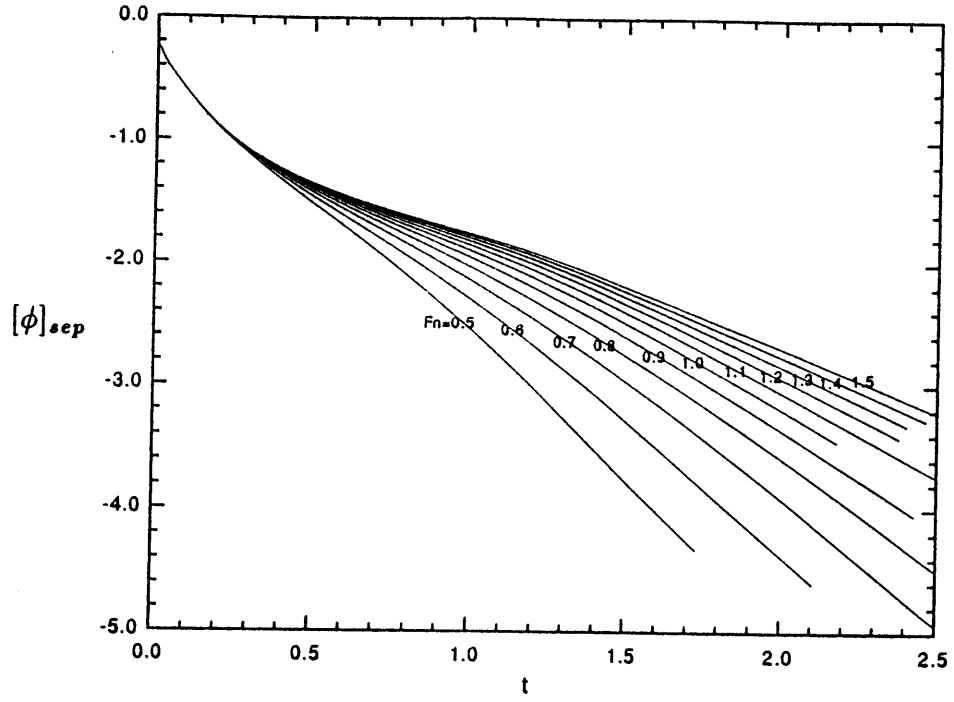

Figure 22. Time evolution of the circulation $[\phi]_{sep}$ at the separation point for various Froude numbers.

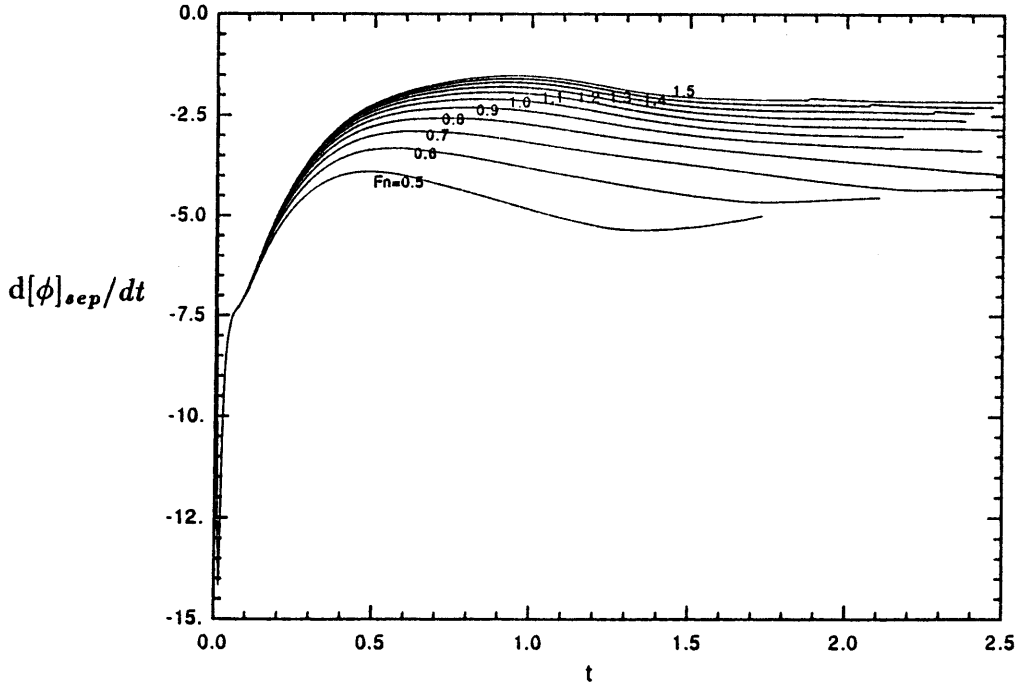

Figure 23. Time evolution of the rate of vortex shedding $d[\phi]_{sep}/dt$ at the separation point for various Froude numbers.

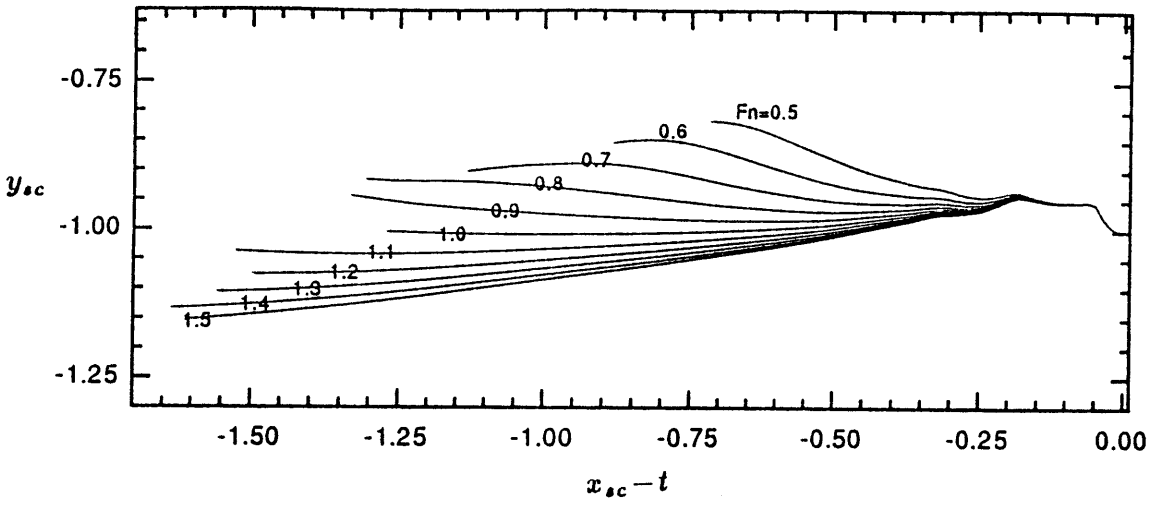

Figure 24. Paths of single-branched spiral center for various Froude numbers.

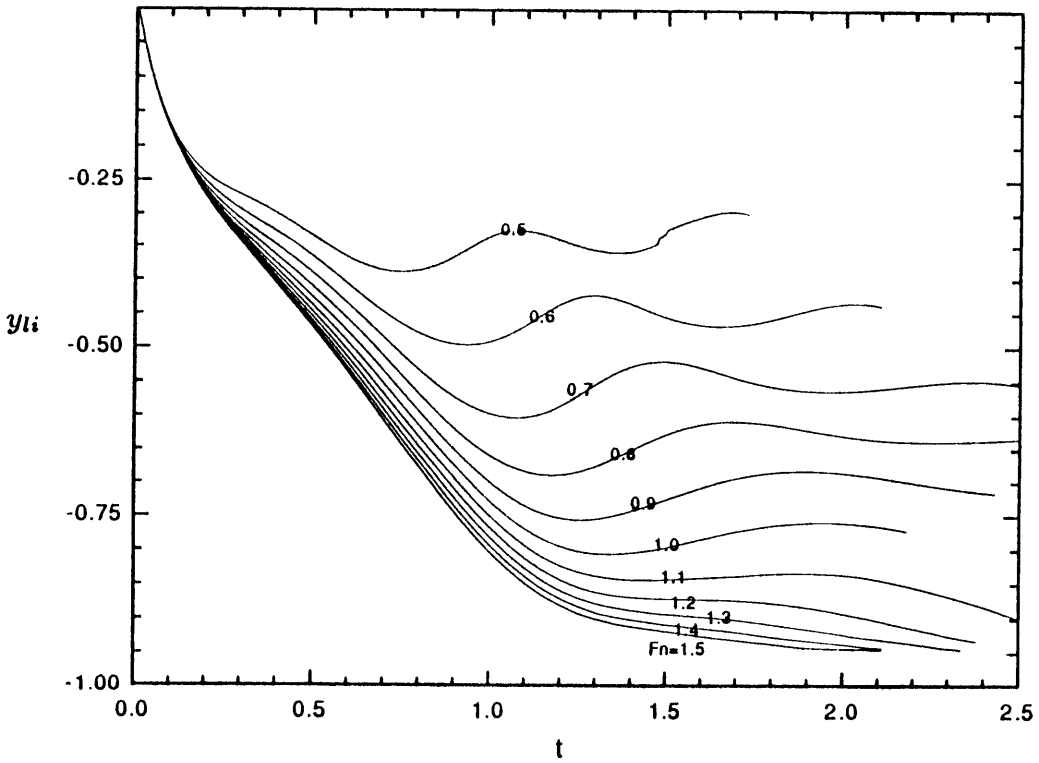

Figure 25. Time evolution of the vertical position of lower intersection point y_{li} for various Froude numbers.

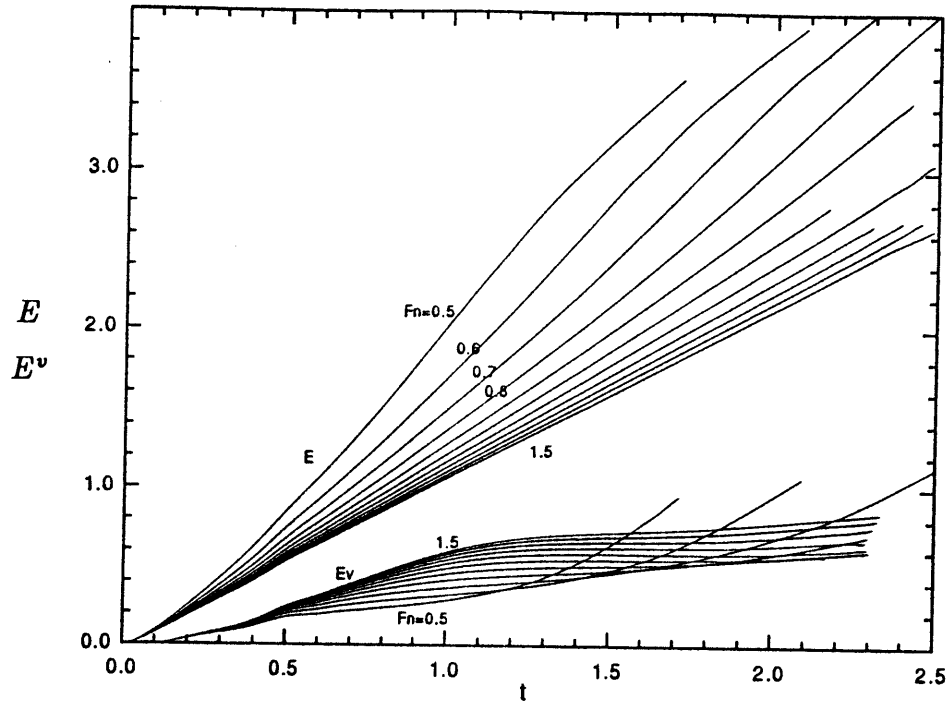

Figure 26. Time evolution of the total energy E and the energy component due to vortex sheet E^v for various Froude numbers.

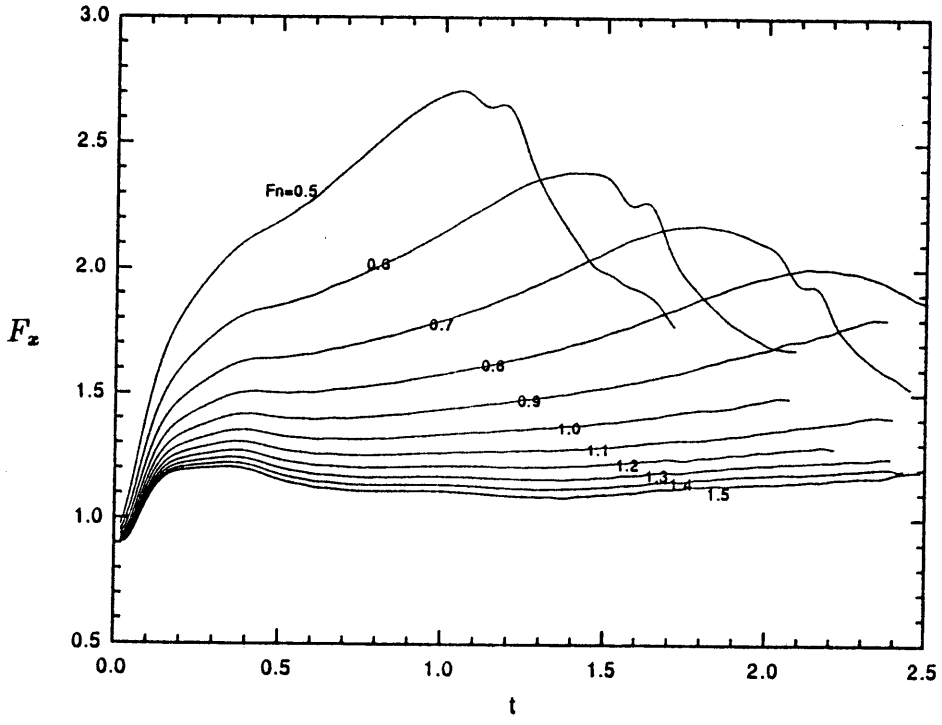

Figure 27. Time evolution of the total horizontal force F_x for various Froude numbers.

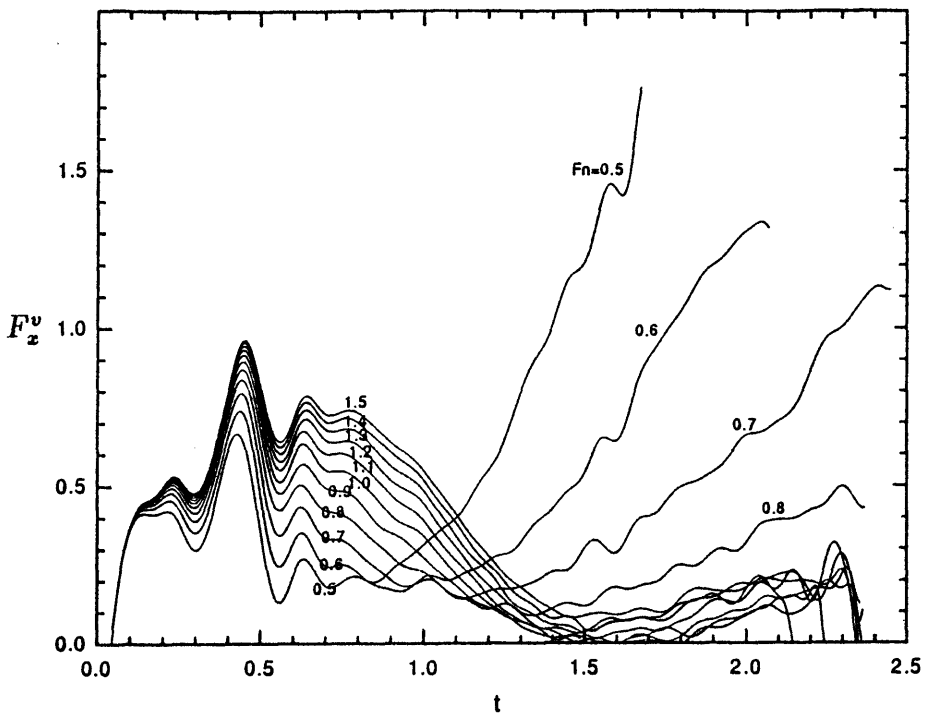

Figure 28. Time evolution of the force component due to vortex sheet F_x^v for various Froude numbers.

4.3. Effect of periodic boundaries

Periodic conditions, imposed on the up- and downstream boundaries, are used to enclose the computational domain. Although such boundaries interfere with the free surface and vortex sheet motions, the interest in the present study is the fluid interactions within the near wake of the plate. We check the effect of such finite boundaries by increasing the length of computational domain. Figure 29 compares two simulation results with different lengths between periodic boundaries ($\ell = 10$ and 20) for $F_n = 0.8$ at $t = 2.15$ and 2.6. The major difference, as expected, is on the forward side of free surface near the boundary. For a narrower domain ($\ell = 10$) the plunging free-surface disturbance certainly reaches the boundary. However, the free surface plungers and the vortex shear layers, which are very sensitive to perturbations, have only minor differences between $\ell = 10$ and 20. Figure 30 shows the comparison of free surface and vortex profiles between $\ell = 10$ and 20 for $F_n = 1.5$. Again, the essential features of the dynamics are not changed by the positions of periodic boundaries up to the final stage of interaction (vortex entrains into free surface). It is therefore concluded that the interaction features between the free surfaces and shear layers are accurately simulated within finite computational domains.

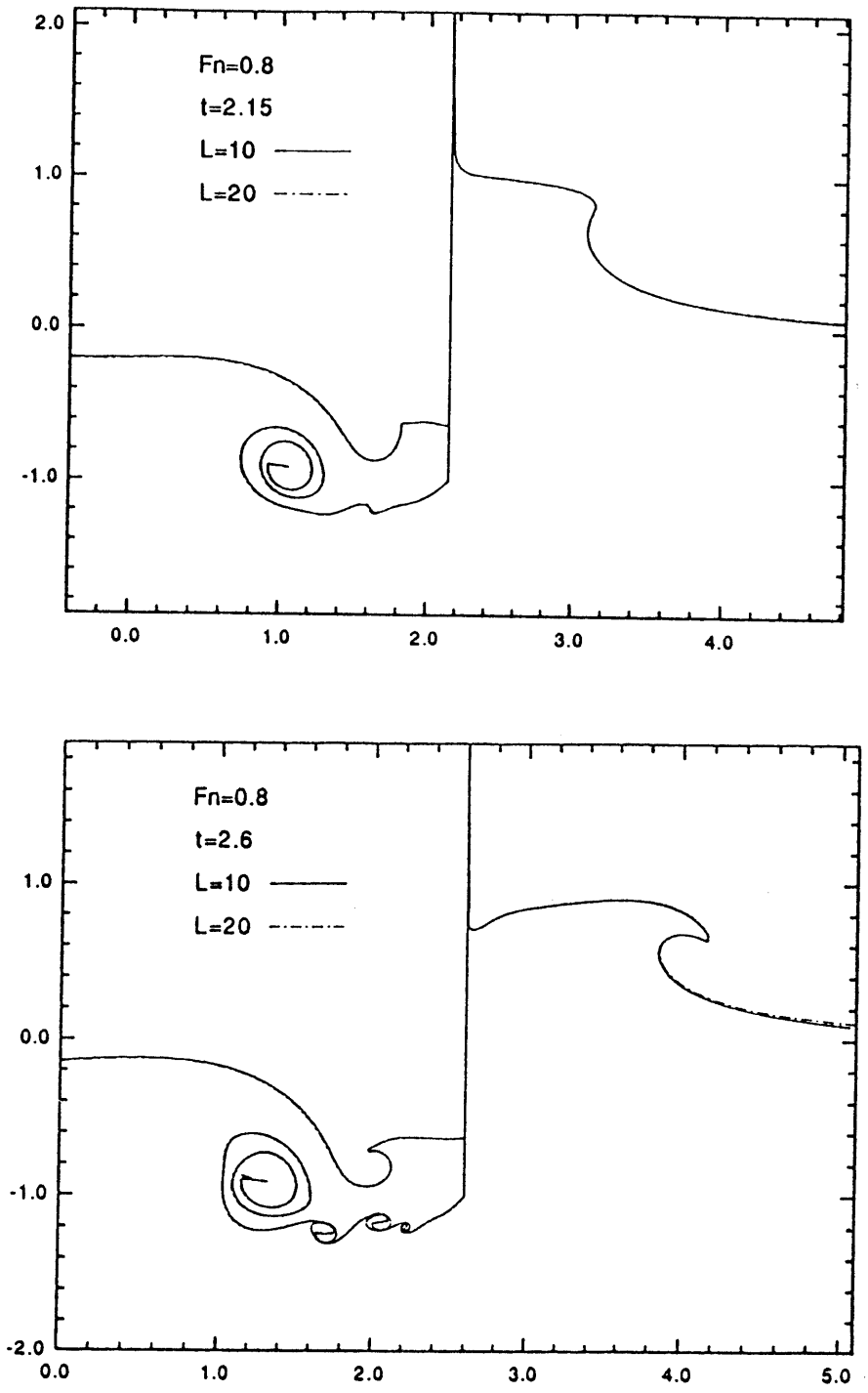

Figure 29. Profiles of free surface and vortex sheet at (a) $t = 2.15$ and (b) $t = 2.6$ for $F_n = 0.8$ and with length between periodic boundaries $\ell = 10$ and 20.

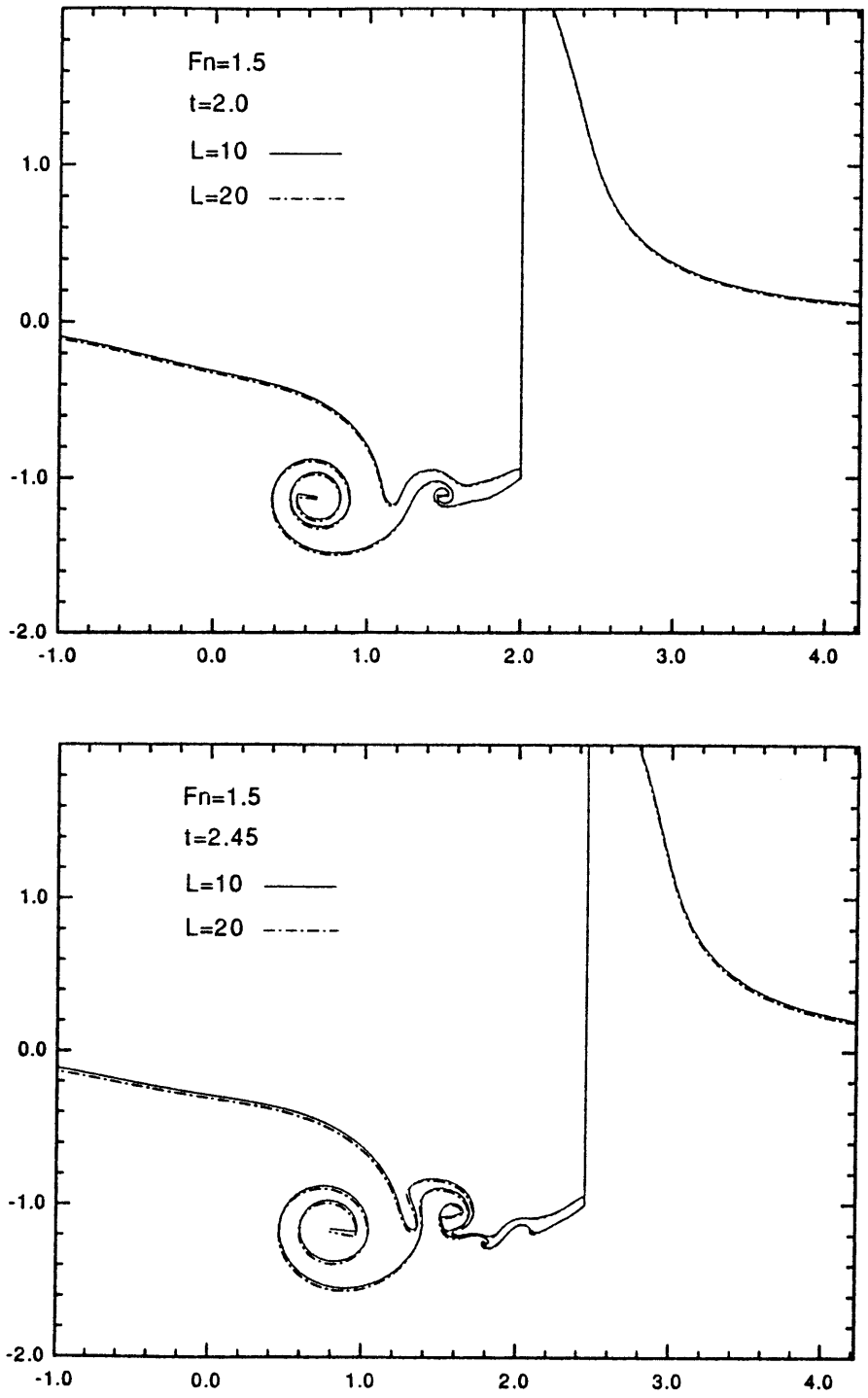

Figure 30. Profiles of free surface and vortex sheet at (a) $t = 2.0$ and (b) $t = 2.45$ for $F_n = 1.5$ and with length between periodic boundaries $\ell = 10$ and 20.

4.4. Effect of impulsive plate motion

As mentioned in §1, to reduce the governing parameters of the interaction dynamics to a single parameter – Froude number, we have used an impulsive acceleration of the plate. The nondimensionalized velocity distribution of such an impulsive motion is described by the Heaviside step function $\mathcal{U}(t)$. It is clearly difficult if not prohibitive to move the plate impulsively in the real experiment. In addition, it is not obvious if the critical role of Froude number and the characteristic features of the interaction dynamics depend on the initial motion of the plate. The effect of impulsive plate motion compared to a smooth startup of the plate is studied by using a velocity distribution $\tanh(t/\delta t)$, where δt is the parameter governing the duration of transition from rest to steady motion. We have used $\delta t = 0.1$ which approximately equals 5% of the typical time period of the entire simulation.

One of the major effects of the transient starting motion compared to the impulsive motion is the delay of formation and growth of the starting single-branched spiral. For the subcritical Froude number range, the single-branched spiral vortex forms well below the free surface and the free surface breaks without any significant surface-vortex interaction. The dynamics features of the subcritical class therefore are not affected by the initial plate motion.

The effect of transient starting motion on the interaction dynamics for the transcritical Froude number class is shown in figure 31 for $F_n = 0.8$. The plate positions of $t = 1.075$, 1.975, 2.275, 2.425, 2.625 and 2.675 in figure 31 are approximately equal to $t = 1.0$, 1.9, 2.2, 2.35, 2.55 and 2.6 respectively in figure 14 for the impulsive plate motion. The delay of formation and growth of the single-branched spiral can be seen by comparing figures 14 and 31. Because of such delay the stretching mechanism of the vortex sheet is postponed and so is the onset of Kelvin-Helmholtz instabilities and the formation of double-branched spirals. As in the impulsive starting motion, the double-branched spirals form well below the free surface and do not interact with the free surface. The transient starting plate

motion therefore only delays the stages of interaction features for the transcritical Froude number range.

Figure 32 shows the evolution of vortex and free surface in the wake of plate for $F_n = 1.5$ (supercritical Froude number) with smooth startup of the plate. The plate positions of $t = 1.075$, 1.725 and 2.075 in figure 32 are approximately equal to those of $t = 1.0$, 1.65 and 2.0 respectively in figure 21 for impulsive plate motion. For the supercritical Froude number case, the delayed formation and growth of the single-branched spiral results in a noticeably different effect on the interaction dynamics from the transcritical class. As in the transcritical class, the delayed single-branched spiral growth postpones the stretching of the vortex sheet and also the propagation of the free-surface depression. Such a delay of set-down propagation accelerates the downward motion of the depressed free surface and consequently the approach of the stretched vortex sheet to the free surface (compare $t = 1.725$ in figure 32 and $t = 1.65$ in figure 21). The onset of Kelvin-Helmholtz instability on the stretched vortex sheet and the roll-up of the double-branched spiral are expedited in contrast to the transcritical interaction (compare $t = 2.075$ in figure 32 and $t = 2.0$ in figure 21). The delay of the backward propagation of the free-surface depression and the entrainment of the double-branched spiral into the free surface speed up the collapse of the free surface as $t = 2.125$ in figure 32 shows.

Although the transient startup of the plate either delays or accelerates the interaction processes depending on the Froude number range, the essential stages of the vortex-free surface interaction are not changed. We therefore conclude that the critical role of Froude number and the characteristic features of the interaction dynamics are independent of the initial plate motion.

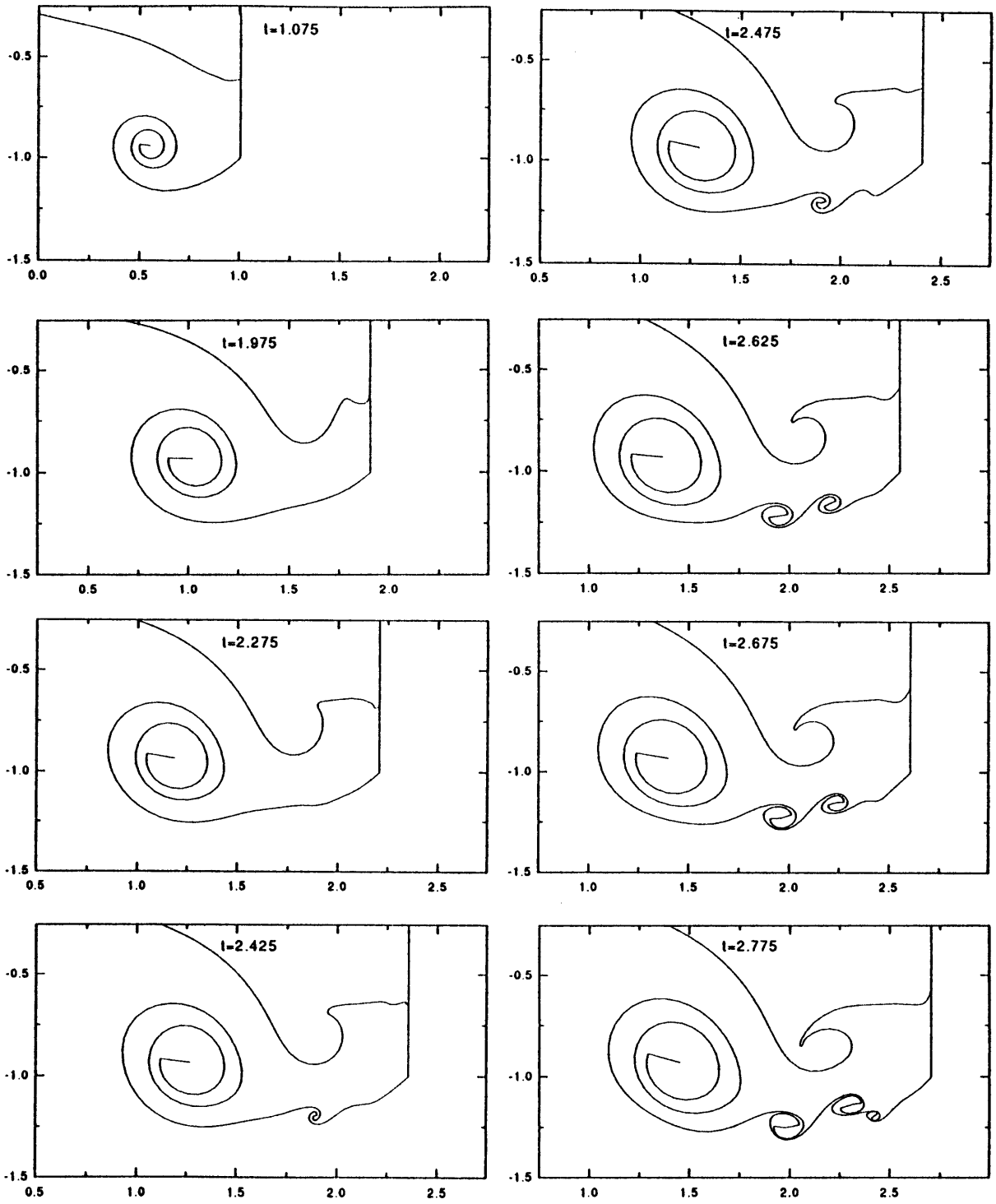

Figure 31. Evolution of the free surface and vortex sheet in the wake of the plate for $F_n = 0.8$ at $t = 1.075$, 1.975, 2.275, 2.425, 2.475, 2.625, 2.675 and 2.775, and with transient starting plate motion.

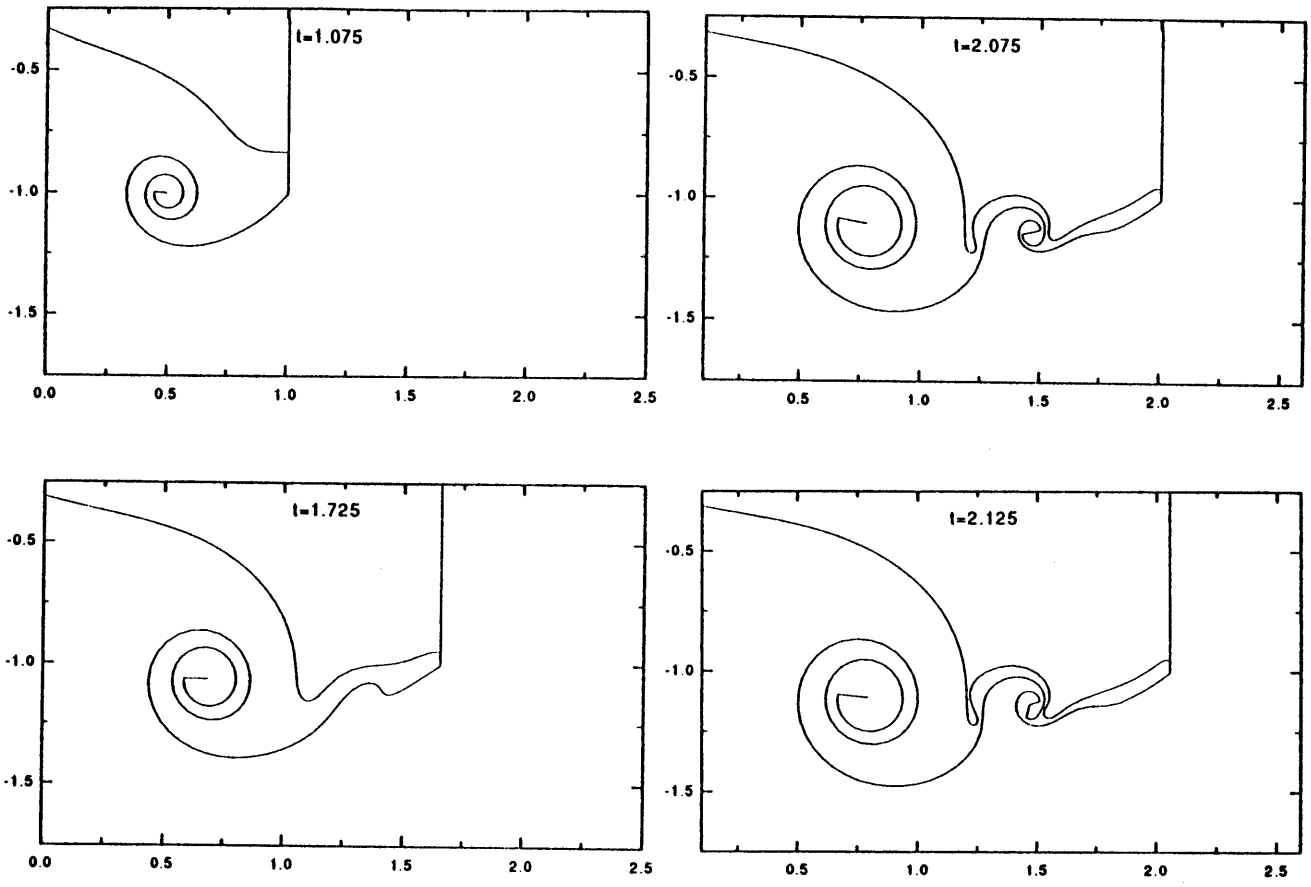

Figure 32. Evolution of the free surface and vortex sheet in the wake of the plate for $F_n = 1.5$ at $t = 1.075$, 1.725, 2.075 and 2.125, and with transient starting plate motion.

5. Conclusion

In this study the complexity of the vortex-free surface interaction in the wake of a moving body is clarified and quantified by considering the motion of a surface-piercing plate. Three classes of interaction dynamics are identified, based on the Froude number, as subcritical, transcritical and supercritical interactions. For subcritical Froude number ($F_n <\sim 0.7$), the free surface breaks on both forward and backward faces before significant interactions with the shed vortex sheet occur. In the higher Froude number range ($F_n >\sim 1.0$), the strong drawn-down deformation of the free surface on the rearward face stretches the trailing vortex sheet and causes finite-amplitude Kelvin-Helmholtz instabilities. For the transcritical Froude number case ($F_n \sim 0.7-1.0$), these instabilities form sufficiently deep below the free surface and allow them to continuously roll up into double-branched spirals. While for the supercritical Froude number range ($F_n >\sim 1.0$), the instabilities entrain the free surface and cause significant free surface deformation. The underlying mechanism and the basic features of vortex-free surface dynamics, such as free surface breaking, vortex entrainment, detachment of starting vortex, stretching of shed vortex sheet, and single- and double-branched spiral roll-ups, are clarified through the numerical simulations.

A robust numerical scheme based on the mixed-Eulerian-Lagrangian approach and incorporating smoothing spline fitting, mesh-function-controlled rediscretization and spiral amalgamation is developed. Detailed accuracy and convergence validation of the numerical scheme has been carried out. Such a numerical scheme can be extended to other vortex-free surface interaction problems such as: damping of floating body due to vortex shedding from the sharp corners, operation of hydrofoil near the free surface and vortical flow over bottom topology.

This study is our first step in an effort to understand the intricate features in the wake of a surface-piercing body. While the flows considered in the present study is two-dimensional and inviscid, considerable insight has been provided into the com-

plex interaction dynamics. Clearly, many questions still remain to be resolved, such as vortex break-down and free surface turbulence. The look into three-dimensional and viscous flows is naturally inevitable.

Appendix A. Numerical evaluation of the discretized integral equations

The integral equations (2.1) and (2.2) are discretized by approximating the contour boundaries by piecewise linear segments, and β and $[\phi]$ by piecewise linear distributions along the segments. Evaluating at suitable collocation points, the discretized integral equations then take the form of a system of linear equations as:

$$\Im \text{ or } \Re\Big[\sum_{z_j\in C_f\cup C_p}\beta_j\Gamma_{jk}+\sum_{z_j\in C_s\cup C_v}[\phi]_j\Gamma_{jk}-2\pi\tilde{\beta}_\infty\Big]=0; \tag{A.1}$$

when $z_k\in C_f$ (imaginary part equations); $z_k\in C_p$ (real part equations), and

$$\Im\Big[\sum_{z_j\in C_f\cup C_p}\beta_j\Gamma_{jk}+\sum_{z_j\in C_s\cup C_v}[\phi]_j\Gamma_{jk}-2\pi\tilde{\beta}_\infty\Big]=-2\pi\psi_k; \tag{A.2}$$

when $z_k\in C_s$. The influence function Γ_{jk} is

$$\Gamma_{jk}=\int_{z_{j-1}}^{z_{j+1}}T_j(z)K(z_j;z_k)\mathrm{d}z, \tag{A.3}$$

and the tent function $T_j(z)$ is defined as

$$T_j(z)=\begin{cases}\frac{z-z_{j-1}}{z_j-z_{j-1}}, & z_{j-1}\le z<z_j\\ \frac{z-z_{j+1}}{z_j-z_{j+1}}, & z_j\le z<z_{j+1}.\end{cases} \tag{A.4}$$

The integration in the influence function $\Gamma_{k,j}$ which cannot be carried out explicitly is evaluated by subtracting a simple pole $1/(z-z_k+\delta_{jk}\ell)$ from the kernel $K(z_j;z_k)$ as:

$$\Gamma_{jk}=\int_{z_{j-1}}^{z_{j+1}}\frac{T_j(z)}{z-z_k+\delta_{jk}\ell}\mathrm{d}z+\int_{z_{j-1}}^{z_{j+1}}T_j(z)\Big[\frac{\pi}{\ell}\cot\frac{\pi}{\ell}(z-z_k)-\frac{1}{z-z_k+\delta_{jk}\ell}\Big]\mathrm{d}z, \tag{A.5}$$

where $\delta_{jk}=1$ when $\Re(z_j-z_k)<-\ell/2$, $\delta_{jk}=-1$ when $\Re(z_j-z_k)>\ell/2$, and $\delta_{jk}=0$ otherwise. The first integral can be evaluated analytically as in Vinje

& Brevig (1981). Representing the kernel of the second integral by a multipole expansion up to second order and evaluating the integration gives,

$$\Gamma_{jk} \cong \frac{z_k - z_{j-1} - \delta_{jk}\ell}{z_j - z_{j-1}} \ln \frac{z_j - z_k + \delta_{jk}\ell}{z_{j-1} - z_k + \delta_{jk}\ell} + \frac{z_k - z_{j+1} - \delta_{jk}\ell}{z_j - z_{j+1}} \ln \frac{z_j - z_k + \delta_{jk}\ell}{z_{j+1} - z_k + \delta_{jk}\ell}$$
$$+ \frac{1}{2}(z_{j+1} - z_{j-1})\left[\frac{\pi}{\ell}\cot\frac{\pi}{\ell}(z_j - z_k) - \frac{1}{z_j - z_k + \delta_{jk}}\right.$$
$$\left. + \frac{1}{3}(2z_j - z_{j-1} - z_{j+1})\left((\frac{\pi}{\ell})^2 \csc^2\frac{\pi}{\ell}(z_j - z_k) - \frac{1}{(z_j - z_k - \delta_{jk}\ell)^2}\right)\right]. \tag{A.6}$$

Appendix B. Adaptive rediscretization algorithm

Given a set of N nodes on the contour boundary

$$f_j = \{(x_j, y_j) \mid 1 \leq j \leq N\}, \tag{B.1}$$

a fitting smoothing spline

$$S = \{x(s), y(s) \mid s_a \leq s \leq s_b\}, \tag{B.2}$$

is solved by minimizing the functional

$$K_\lambda(S) = \int_{s_a}^{s_b} [S^{(2)}(s)]^2 ds + \lambda \sum_{j=1}^{N} [S(s_j) - f_j]^2, \tag{B.3}$$

with natural boundary conditions at $s = s_a$ and s_b (see de Boor (1978) or Lancaster & Šalkauskas (1990) for details). The weighting parameter λ measures the compromise between the smoothness or fitting (decreasing λ) and accuracy or interpolating (increasing λ) of the spline functions.

After the smoothing spline is calculated, the contour is rediscretized based on equidistribution of the "mesh function" $\kappa(s)$ (Hyman & Naughton 1985) along the contour such that the new node discretization has the a priori prescribed value of

$$I_\kappa = \int_j^{j+1} \kappa(s) \frac{ds}{dj} dj, \tag{B.4}$$

on the j-th segment between nodes j and $j+1$, where s is the arc length of the boundary. In the present work we choose the curvature of the contour as the mesh function κ. To guarantee a minimal a priori accuracy and to prevent the size of segments from decreasing too rapidly, a constraint is imposed in rediscretizing for the size of the j-th segment h_j:

$$h_{min} \leq h_j \leq h_{max}, \tag{B.5}$$

where h_{max} and h_{min} are upper and lower limits of the segment sizes. The choice of h_{min} also guarantees the suppression of instabilities with wavelengths shorter than

$2h_{min}$. In summary, the controlling parameters for adjusting the rediscretization are the weighting parameter for smoothing cubic spline fitting λ, the integration of the mesh function on each segment I_κ, and the maximal and minimal limits of segment size h_{max} and h_{min}.

References

Birkhoff, G. & Fisher, J. 1959. Do vortex sheets roll up? *Rend. Circ. Mat. Palermo.* **8**, 77–90.

Chorin, A. & Bernard, P.S. 1973. Discretization of a vortex sheet, with an example of roll-up. *J. Comput.. Phys.*, **12**, 423.

de Boor, C. 1978. *A Practical Guide to Splines*, Springer-Verlag.

Dimas, A.A. 1991. Nonlinear interaction of shear with a free surface. Ph.D. thesis, MIT, Department of Ocean Engineering.

Dommermuth, D.G., Yue, D.K.P., Lin, W.M., Rapp, R.J., Chan, E.S. & Melville, W.K. 1988. Deep-water plunging breakers: a comparison between potential theory and experiments. *J. Fluid Mech.* **189**, 423–429.

Faltinsen, O.M. & Pettersen, B. 1982. Vortex shedding around two-dimensional bodies at high Reynolds number. In *Proc. 14th Symp. Naval Hydrodynamics., Ann Arbor, MI*, PP.1171–1213.

Fink, P.T. & Soh, W.K. 1978. A new approach to roll-up calculations of vortex sheets. *Proc. Roy. Soc. Lond.* A**362**, 195–209.

Graham, J.H.R. 1983. The lift on an aerofoil in starting flow. *J. Fluid Mech.* **133**, 413–425.

Hoeijmakers, H.W.M. & Vaatstra, W. 1983. A higher order panel method applied to vortex sheet roll-up. *AIAA J.* **21**, 516–523.

Hyman, J.M. & Naughton, M.J. 1985. Static rezone methods for tensor-product grids. *Lectures in Applied Mathematics* **22**, pp.321–343. AMS, Providence.

Krasny, R. 1986. Desingularization of periodic vortex sheet roll-up. *J. Comput. Phys.* **65**, 292–313.

Lamb, H. 1932. *Hydrodynamics*, Cambridge Univer. Press.

Lancaster,P. & Šalkauskas, K. 1990. *Curve and Surface Fitting*, Academic Press.

Lin, W.M. 1984. Nonlinear motion of the free surface near a moving body. Ph.D. thesis, MIT, Department of Ocean Engineering.

Longuet-Higgins M.S. & Cokelet, E.D. 1976. The deformation of steep surface waves on water. I. A numerical method of computation. *Proc. Roy. Soc. Lond.* **A350**, 1–26.

Moore, D.W. 1979. The spontaneous appearance of a singularity in the shape of an evolving vortex sheet. *Proc. R. Soc. Lond.* **A365**, 105–119.

Moore, D.W. 1981. On the point vortex method. *SIAM J. Sci. Stat. Comput.* **2**, 65–84.

Newman, J.N. 1977. *Marine Hydrodynamics*, MIT press.

Pullin, D.I. & Phillips, W.R.C. 1981. On a generalization of Kaden's problem. *J. Fluid Mech.* **104**, 45–53.

Rosenhead, L. 1931. Formation of vortices from a surface of discontinuity. *Proc. Roy. Soc. Lond.* **A135**, 170–192.

Sarpkaya, T. 1989. Computational methods with vortices – The 1988 Freeman scholar lecture. *J. Fluids Engrg.* **111**. 5–52.

Vinje, T. & Brevig, P. 1981. Nonlinear two-dimensional ship motions. *The Ship Research Institute of Norway, Rep.* R-112.81.

Yu, D. & Tryggvason, G. 1990. The free-surface signature of unsteady, two dimensional vortex flows. *J. Fluid Mech.* **218**, 547–572.